YOKOHAMA NATIONAL UNIVERSITY

Doctoral Thesis

Interference effects of wind-over-top flow on twin square cylinders

Author:

DOAN Sy Long

Academic supervisors:

Prof.Dr. YAMADA Hitoshi

Prof.Dr. KATSUCHI Hiroshi

A thesis submitted in fulfilment of the requirements
for the degree of Doctor of Philosophy in Engineering
in the
Department of Urban Innovation

July 29th , 2019

Abstract

There are few standard designs of wind-resistance for high-rise buildings structure in urban area. Interference effects become a highly concerns among research fields these days to completely understand the behaviour of buildings due to the mutual effects. This research will contribute a part of knowledge about wind-over-top (WOT) flow over square cylinders in smooth flow condition. There are two main objectives in this dissertation: 1) Investigate the characteristics of the WOT flow; 2) Simulate these characteristics in Computational Fluid Dynamic (CFD) using OpenFOAM.

Characteristics of the WOT flow over square cylinders are investigated through a series of wind tunnel tests including static and dynamics tests. The principal model is designed as the pressure taps model located on the self-designed elastic system. Wind tunnel tests are conducted with various wind speed and angle of attack to get the pressure value on the pressure taps around four faces and the top displacement of the principal model. This principal model locates at the origin of the Cartesian coordinate system which is set-up on the wind tunnel floor. Two different height of wooden rigid interference models are set-up in different position in Cartesian coordinate system to evaluate the interference effects. The same height interference test contributes the effect of the WOT flow and side flow to principal model. On the other hand, the double height interference test only contributes the side effects to the principal model. The characteristics of the WOT flow is assessed through the comparison of same height interference test and double height interference test.

The experimental results show that large area near the top of the downstream building is affected from the WOT flow. This WOT flow could affect to 21% area of the front face. This effect could reach up to 61.31% compared to the mean positive pressure of the front face. Moreover, the WOT flow show it beneficial effect to the vibration of the principal model. In closed distances of two square cylinder, the vortex-induced vibration of the principal model vibrates with small amplitude with the presence of the WOT flow. In further distance, the principal model vibrates at higher reduced velocity with the presence of the WOT flow. PIV test shows that the WOT flow contains two main parts: 1) Shear layer generated from the rooftop of upstream building; 2) Unsteady vortex located under the shear layer and tip at the edge top of upstream building.

CFD is conducted by using open-source program, OpenFOAM. There are two methods which are applied in simulation: 1) The most common method among pratical computational wind engineers, Unsteady Reynolds Averaged Navier-Stokes (URANS); 2) The more precise simulation and more computational effort Large Eddy Simulation (LES). In URANS tests, the polyhedral mesh type shows its advantages when reducing number of mesh cells and keeping the accuracy of simulation. The k-Ω SST turbulence model well reproduces the velocity field among other turbulence models of URANS to give the correct trend on the face pressures of the downstream model. In this part, the condition to form the WOT is proposed. The WOT flow is only formed between two building with the distance of two buildings $3 \leq x/B \leq 6$ (B is the width of building). URANS model could not reproduce well for the unsteady vortex of the WOT flow

under the shear layer. On the other hand, LES methods with Smagorinsky sub-script scale model can reproduce the unsteady vortex of the WOT flow.

Acknowledgement

Three years in Japan almost pass with the tough work for the doctoral dissertation. It is the time to thank all those who helped me go through this period and make my stay at Yokohama City become more pleasant.

This doctoral dissertation would not be completed without fruitful advices, comments and guidance from my supervisors, Prof. Yamada Hitoshi and Prof. Katsuchi Hiroshi. Their interests have encouraged me to put myself in the research area. I do appreciate all the things supervisors has done for me before and so far.

I would also like to thank the committee member, Prof. Fujino Yozo, Assoc. Prof. Dionysius M Siringoringo, Assoc. Prof. Tamura Hiroshi for serving as the member of the thesis committee. I deeply express my sincere gratitude to their invaluable discussion on every detail on the dissertation contents according to their expertise.

Special gratitude to Assist. Prof Kim Haeyoung for their enormous helps and in-depth discussion on the CFD simulation. Also, I do not forget to say thank to Sakai san who always supports me with all kinds of document during the research time.

Very special thanks go to Prof. Hoang Nam (HCMUT-Vietnam) and Prof. Taweep Chaisomphob (SIIT-Thailand) to give me initial steps and encourage me to research at YNU.

I would like to express my gratitude to the Ministry of Education, Culture, Sports, Science and Technology, Japan for the Monbukagakusho (MEXT) program. Thank you for every food, accommodation and facilities.

I do not forget to give a warm thank to Dr. Nguyen Pham Quang Vu, who always give me a hand since the first day I was in Japan.

I am very appreciative to all colleagues at YNU for supports and friendship. The warmness indirectly pushed me to walk forward. I would like to thank to everyone for their talk, smile and laugh.

Finally, I wished to thank my parents who constantly encouraged me every time, take care me every seconds of my life. Also, I send my warm thank to my wife, who often gives me a beautiful smile and warmly take care of family. And thank you my son, Pooh, to be here with daddy.

There is many one I have not mentioned, I never forget even some little help, and thank you is not enough for you all.

Nomenclature

$\overline{c_p}$ = Mean of pressure coefficient

c = Damping coefficient (Ns/m)

C_D = Drag coefficient

C_f = Skin friction coefficient Schlichting

C_L = Lift coefficient

C_M = Momentum coefficient

C_μ = Turbulence model constant (0.09)

Co = Courant number

f = = Structure frequency (Hz)

F_D = Drag force (N)

$F'_{D(t)}$ = Fluctuating drag force (N)

F_l = Lift force (N)

G = Gust factor

I_u = Turbulence intensity in along wind direction (%)

I_v = Turbulence intensity in across-wind direction (%)

I_w = Turbulence intensity in height direction (%)

k = Kinetic energy

L_m = Centre of aeroelastic model to pivot point (m)

L_e = Distance from pivot point to the centre of mass of steel stick (m)

l_d = Distance from pivot point to the centre of damping card (m)

M = Model mass (kg)

nuTilda = Turbulence kinetic viscosity (m^2/s)

OM = overturning moment (Nm)

Re = Reynold number

RMS = Root mean square (m)

$S_{u(n)}$ = The spectrum of the longitudinal turbulence

S_c = Scruton number

$\bar{u}$ = Mean longitudinal wind velocity (m/s)

U = Mean wind velocity (m/s)

Ug = galloping critical reduce flow speed (m/s)

Ur = Karman-vortex resonance reduced flow speed (m/s)

v'(t) = The lateral or crosswind component of turbulence

x = distance in along wind direction (m)

$x_{(t)}$ = Total response of the structure (m)

$\bar{x}$ = Mean of response of the structure (m)

$x'_{(t)}$ = Fluctuation of response of the structure (m)

y = Distance in across wind direction (m)

z = Distance in model's height direction (m)

ρ = Air density (kg/m^3)

ζ_0 = Damping ratio

ε = Dissipation rate

ω = Specific dissipation rate

μ = Molecular dynamic viscosity (kg/m/s)

μ_t = Turbulence viscosity

$\frac{\mu}{\mu_t}$ = Eddy viscosity ratio

ζ = Damping ratio

ν = (Nu) Kinematic viscosity (Momentum diffusivity) (m^2/s)

τ_w = Shear wall stress

Content

List of Figures

List of tables

Chapter 1

Introduction

There have been few detailed standards about wind-resistant design for high rise buildings due to mutual interference effects. Wind tunnel test is still an important method to design wind resistance in urban areas. This topic has become a concern for many researchers (Bailey and Kwok 1985, Zdravkovich 1985, Taniike 1991, Taniike 1992, Xie and Gu 2004, Kim, Tamura et al. 2009, Yu and Xie 2015) for decades. Other researches were concerned about a conical vortex on the rooftop (Marwood and Wood 1997, Banks, Meroney et al. 2000, Banks and Meroney 2001, Banks and Meroney 2001, Wu, Sarkar et al. 2001, Kawai 2002). The conical vortex produces a stationary negative pressure on the roof but does not move downward. The shear layer generated from the flat roof accompanies with the moving downward vortex on the side face, called Karman vortex, and forms the complex three-dimension type on the leeward path. This three-dimension (3-D) vortex is called an arch-type vortex (Kawai 2002). A research on interference in details in this study will distinguish between effects from flows on the side and effects from the flow on the roof of a building called wind-over-top (WOT) flow.

These studies, however, mostly focus on the interference factors of static or dynamic of overall wind load. The WOT flow is a non-stationary complicated path and plays a different role from Karman vortex generated on the side. According to Taniike (1992), the principal building receives more angular momentum which is generated from the shed vortices of an upstream building. Kawai, Okuda et al. (2009) showed that the unsteady rooftop wind generates the arch-type vortex which stretches in a stream-wise direction near the tip of the vortex. A presence of an upstream building accelerates the flow and magnifies the pressure on the flat roof of a downstream building (Pindado, Meseguer et al. 2011). However, the effects of WOT flow from the upstream building to side faces of the downstream building remain unclear.

Chapter 2

Background and Literature Review

2.1 Interference effects in high-rise building

2.1.1 Isolated building test

In the isolated test, the combination of the WOT flow and Karman vortex turns into the arch-type vortex which was initially mentioned in Kawai, Okuda et al. (2009). This 3-D structure of wake is formed just behind the square cylinder and always keeps its form during the formation and shedding of Karman vortex. Although the tip of arch-type vortex stays still during the cycle of Karman vortex, this type of vortex can stretch in the stream-wise direction (Kawai, Okuda et al. 2012). In interference tests, the principal building at downstream receives more angular momentum which is generated from the shed vortices of an upstream building (Taniike 1992). In addition, the presence of an upstream building accelerates the flow and magnifies the pressure on the flat roof of a downstream building (Pindado, Meseguer et al. 2011). However, the effects of only the WOT flow from the upstream building to the downstream building in interference tests remain unclear.

The flow structure over the bluff body as square cylinder in uniform stream is represented in Figure 2-1. The wind faces of bluff body build up with the positive pressures. While the rear faces between two shear layers fall to negative pressure. The vortex generated after body will form to Karman vortex. This vortex makes to side change continuously in pressure leading to the vibration of the bluff body.

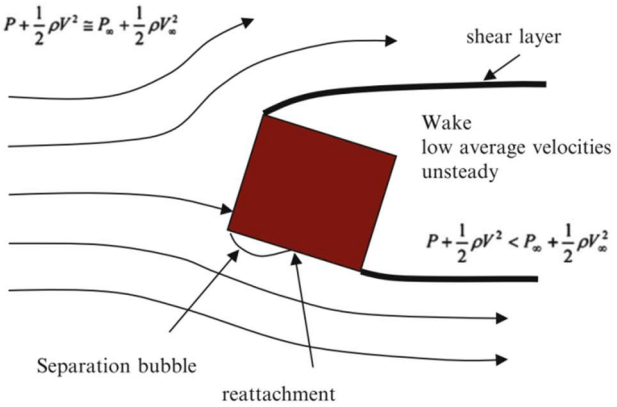

Figure 2-1: Square body in smooth flow (Tamura and Kareem 2013)

2.1.2 Interference building test

Kim, Tamura et al. (2015) indicated that the local pressure calculated by root-mean-square (RMS) near the top of a building increases up to 84% compared to the isolated building. The

interference tests with various position show that the mean increase of mutual effects is only 13% to 40% on the principal building (Xie and Gu 2004, Hui, Tamura et al. 2012, Yan and Li 2016). The reason for high local pressure on the side faces near the top is explained by the three-dimensional approaching flow velocity and shear layer from the roof top of interference building. Therefore, the WOT flow from vicinity building plays an important contribution in the designs of claddings on the side faces near the top of the principal building.

Current research area shows that the interference researches with two buildings under 400m were considered by most of researches using the cartesian coordinator system or polar coordinator system. A research conducted the interference test over 400m of prototype building can be found in LI and LI (2015). A group of multiple interference buildings were presented by Xie and Gu (2004) for three buildings and Lam, H. Leung et al. (2008), Lam, Zhao et al. (2011) for a row of buildings. In addition, effect of breadth ratio, Br = 0.4 – 1.4, always create the shielding effect to the downstream model. The shielding are is expanded with the increasing breadth of the interference building (Yu and Xie 2015).

An upstream building in interference tests, in general, reduces the mean response of the principal building by shielding effects. Due to various positions of the upstream building, some parts on cladding pressure or even the dynamic properties of the principal building turn into overestimated values (Yahyai, Kumar et al. 1992). The peak oscillatory amplitude is likely to increase by three times in an interference test compared to isolated cases for both square and circular cylinders (Gowda and Kumar 2006). The interference regime at a distance of $x/B < 6$ (B: width of the downstream model) is able to produce most of vortex shedding types (Zdravkovich 1985). The sensitive height of the upstream building in interference tests is 0.5-1.5H_0 (H_0: Height of the downstream building) (Xie and Gu 2004, Kim, Tamura et al. 2015). Therefore, the upstream building in double height to the height of the principal building will remove all effects from flows on the roof of the upstream building.

The results of the spacing and position of interference building did not show clearly in literature. The closed space was identified less than 6B with B is the width of building, and large space was over 6B (Stathopoulos and Baniotopoulos 2007). The interference effect is clearly when locate within 2-13B (Cheng and Lin 2005). In tandem arrangement, spacing less than 3B could cause the negative pressure and likely to magnify the dynamic forces (Cheng and Lin 2005, Han, Gu et al. 2012).

English (1993) proposed the equation for the mean of interference factor (IF) for rectangular shape with two buildings. And, it was approved by many researchers (Xie and Gu 2004, Kim, Tamura et al. 2009). However, this equation has no correlation to the inflow condition. Therefore, to apply this equation, the inflow condition must follow the condition of wind tunnel by English (1993). An example of the correlation to the inflow boundary condition in Taniike (1991). He researched on the IF of along-wind and across-wind direction. The results show that the IF decreases exponentially with the increase of turbulence intensity and were reduced to 1 when the turbulence intensity increased up to 17-18%.

$$IF = -0.05 + 0.65X + 0.29X^2 - 0.24X^3 \quad \textbf{(2.1)}$$

2.2 Dynamic phenomenon

The studies about the excitation mechanisms include the vortex shedding, turbulence buffeting, and those related to the aeroelastic effects such as amplitude dependent crosswind and torsional lock-in excitations, galloping, and the reparation, reattachment mechanism for torsion (Tamura and Kareem 2013). The displacement from these vibrations is not sensitive to the stiffness and mass of the building. Recent research has been focusing on passive and active vibration controls.

To investigate the dynamic properties of a square cylinder, several methods have been applied by multiple-degree-of-freedom (MDOF) model or single-degree-of-freedom (SDOF) model with supporting systems at the base of models. A comparison of SDOF and MDOF model was conducted by Yoshie, Kawai et al. (1997) in a series of wind tunnel tests. The results showed that there is no significant difference between SDOF and MDOF in across-wind of square cylinders. Moreover, the effect of the motion-dependent force is more significant on the across-wind direction (Thanh, Yamada et al. 2005). Therefore, the research on the across-wind direction of a building is in demand.

The excitation in along-wind direction is explained through the drag force and fluctuating drag in equation below. The total longitudinal wind velocity is divided to mean and fluctuating part. The response of the along-wind could be estimate through the method in Figure 2-2.

$$F_D(t) = C_D \frac{1}{2}\rho A u^2(t) = C_D \frac{1}{2}\rho A\left(\bar{u} + u'(t)\right)^2 \tag{2.2}$$

$$C_D \frac{1}{2}\rho A\bar{u}^2 + C_D \rho A \bar{u} u'(t) = \bar{F}_D + F'_D(t)$$

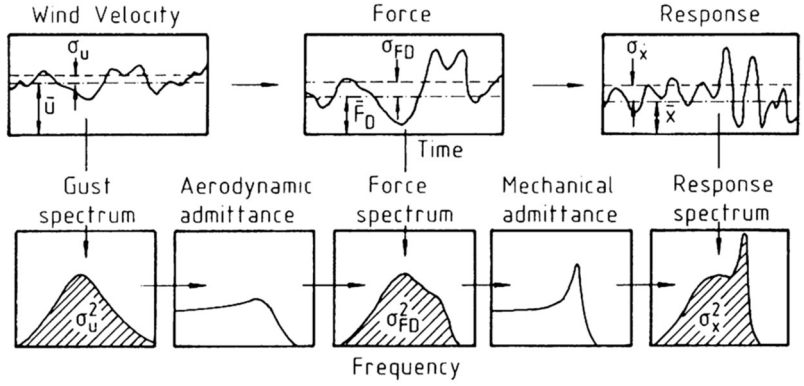

Figure 2-2: Along wind excitation and response process (after Davenport 1967)

Excitation due to incident turbulence as fluctuating cross wind force is calculated in (2.3). This is more significant for the structures with a long afterbody.

$$F'_L = C_L \rho \bar{u} b v'(t) + \left(C_D + \frac{\partial C_L}{\partial \alpha}\right)\rho \bar{u} b v'(t) \tag{2.3}$$

The various research has studied on the wake-induced crosswind forces (Figure 2-3). The turbulence intensity impacts to the strength of the vortex shedding. To be more details, the high turbulence flow could reduce the strength of vortex shedding and widen the crosswind force spectrum. The low height to breadth ratio generate the vortex shedding in less organization, which broadening of the crosswind force spectrum. Moreover, structures with a short afterbody produce the narrow bandwidth of the force spectrum corresponding to high Strouhal number $St = \frac{f_0 b}{u}$.

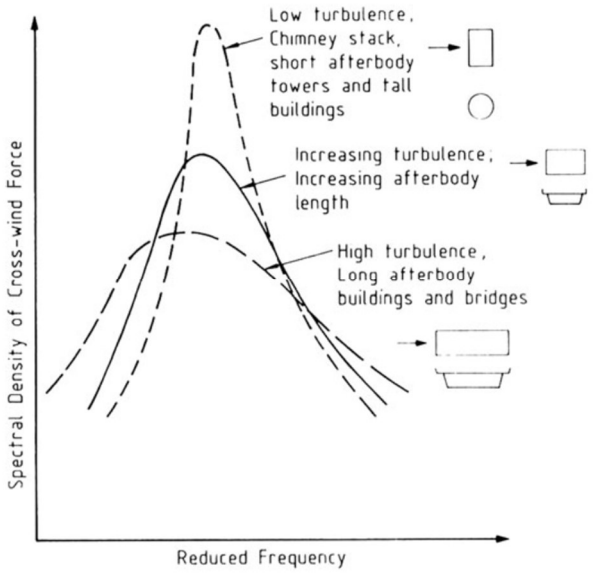

Figure 2-3: Frequency distribution of wake-induced forces for various structures and free stream turbulence (Melbourne 1975)

Regarding to the instability vibration, some phenomenon has been researched to avoid in the structures such as wake galloping (for 1 DOF structure), flow switching, lock-in excitation, flutter (two or more DOF).

Wake galloping makes engineers more carefully consider of the vibration of upstream structure. We try to avoid the downstream structure oscillate due to the velocity field behind the upstream model. Wake galloping especially happens in the sharp-edged bluff body. If there is a phrase shift between the position and the force of rear member as

$$Y = y_0 \sin(\omega_1 t) \qquad \textbf{(2.4)}$$
$$F = F_0 \sin(\omega_1 t - \phi)$$

By this time, the actual flow pattern around the downstream member is appropriate to the static value of the force at an earlier time. The wake galloping happens when the rear member is constrained to move in only one direction.

Flow switching could possibility happens in the cylinders when there is the switch between the laminar separation with wide wake and high drag, and turbulent separation with narrow wakes and low drag.

Lock-in excitation happens when the natural frequency of structure is coincided with the frequency of vortex shedding. For tall buildings in turbulent boundary layer flow, the critical amplitude during lock-in excitation was 0.6% of the diameter for circular cylinder and 2.5% for prismatic structure (Kwok and Melbourne 1981)

Flutter is another dynamic instability of an elastic structure that was responsible for the failure on the Tacoma narrows Bridge. To find the total solution for flutter, all the Aerodynamic coefficients H_i^* and A_i^* which are known as flutter derivatives in (2.5) need to assume clearly. Unlink the galloping case, the flutter derivatives can be obtained from the static test. For the limitation of this study, the flutter is not put into the consideration of research

$$\ddot{z} + 2\zeta_z \omega_z \dot{z} + {\omega_z}^2 z = \frac{F_z(t)}{m} + H_1^* \dot{z} + H_2^* \dot{\theta} + H_3^* \dot{\theta} \tag{2.5}$$

$$\ddot{\theta} + 2\zeta_z \omega_z \dot{\theta} + {\omega_z}^2 \theta = \frac{F_\theta(t)}{m} + A_1^* \dot{z} + A_2^* \dot{\theta} + A_3^* \dot{\theta}$$

Other fluctuation forces could be considered in the dynamic design for structure would be torsional vibration and ovalling vibrations induced by vortex shedding. Torsional vibration is induced by turbulence buffeting and mostly occurs onto a long afterbody with reattaching flow or from the vortex shedding from neighbouring tall buildings. Also, this phenomenon could be found in the asymmetrical or complex building shapes, which generating the mean and dynamic torques. With open-ended thin-walled structures like chimneys, storage bins and silos, the vortex shedding can generate the fluctuating drag forces which cause along-wind vibrations and fluctuating pressure leading to ovalling vibration.

2.2.1 Isolated building

Fluid dynamic firstly start with low Reynold number as in the water environment. A list of research and comparison of force coefficients and Strouhal number for flow past a stationary square cylinder in low Reynold number (100-200) is listed in Zhao (2015). In high Reynold number, Bearman (Bearman and Morel 1983) mentioned about the relationship between effective Reynold number and free stream turbulence. He explained about two conditions in flow to get effect from the Reynold number to the turbulence intensity: The flow is in the transient flow and in the same direction with free stream. If two of these conditions are not met, there is no correlation between effective Reynold number and free stream turbulence. For example, the increasing of Reynold number leads to the reduction of boundary layer skin fiction. While, the free stream turbulence increases the boundary layer skin fiction.

Turbulence around the bluff bodies has been researched by many researchers. Bearman (Bearman and Morel 1983) proved that the drag force acting on rectangular section in turbulence flow is lower than the case with smooth flow.

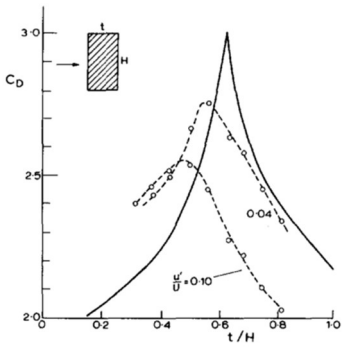

Drag of 2D rectangular bars in smooth and turbulent streams.
——— smooth (Bearman and Trueman (1972), – – – – turbulent, Courchesne and Laneville (1978).

Figure 2-4: Drag coefficient in different flow of rectangular cylinder (Bearman and Morel 1983)

There are 2 types of vorticity in square cylinder (Kawai 2002): 1) Non-moving type: formed on a flat roof in an oblique angle. 2) Moving type: vortex shedding. Kawai et.al. (Kawai and Nishimura 1996) also indicated the large suction along the leading edge near the corner is caused by the conical vortex on the roof. This type of vortex is form as stationary which is not induce the fluctuating suction on the roof and do not move downward. However, the pressure caused by this vortex on the roof is very large particularly in the turbulent flow. In addition, Matsumoto (Matsumoto, Yagi et al. 2008) presented 2 main kinds of vortex in rectangular cylinder: 1) Karman vortex: Strouhal number St, lock-in vibration, occur at Vres = 1/St. 2) Motion-induced vortex: due to shear layer instability, reduced velocity = 1.67B/D. The torsional flutter instability is mainly dominant by the motion-induced vortex excitation. Noted that the motion-induced vortex can be generated only at the low reduced velocity range (6 to 12). The flow pattern will dramatically change from low to high reduced velocity around the cylinder during the torsional motion. There are two condition to generate conical vortex. Firstly, the approaching gust attacks the roof from 25°. Secondly, the gust blows straightly in a relatively long time at least when the fluid particle travels a distance 4-5 times the roof size. However, these may not be the sufficient conditions.

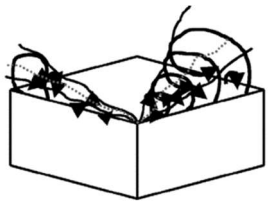

Figure 2-5: Strong conical vortex to induce high peak suction (Kawai 2002)

The relationship between Reynold number, angle of attack and Strouhal number was mentioned in Norberg (1993). At the angle of attack is 0°, the Strouhal number of a square cylinder is around 0.13 for Re from 10^4-10^5. This number is various with the ratio of the breath to depth of the model. It is found that there is no much change of Strouhal number in the different angle of attack at the same Reynold number about 1×10^3-5×10^3.

Scruton number S_{sc} is presented for the mass-damping parameter. Scruton number for rectangular cylinder is calculated as

$$S_{sc} = \frac{4\pi M \zeta_0}{\rho B D H} \tag{2.6}$$

Where M: Model mass (kg); ζ_0: Damping ratio; B, D, H: width, length, height of building; ρ: Air density. To be more detail, two more definitions are given here. Karman-vortex resonance reduced flow speed is Ur = 1/St and Ug (galloping critical reduce flow speed) = $U_g = \frac{2S_{sc}}{A_1}\frac{B}{D}$, $A_1 = -\frac{dCF_y}{d\alpha}_{(0)}$, therefore $\frac{U_g}{U_r} = \frac{2S_{sc}St}{A_1}\frac{B}{D}$. The high values of the Scruton number by this definition is estimated 50-60. In this ranges, the excitation due to the vortex-induced vibration and galloping is completely decoupled. This is very important for design, most the structures are currently considered as the lower value of Scruton number. Therefore, the vibration can be occurred where they are not predicted by any standards or specification. In fact, the galloping critical flow velocity is predicted with Scruton number no lower than about 60 (Mannini, Marra et al. 2017).

The comparison of SDOF and MDOF model is conducted by Yoshie et.al. (Yoshie, Kawai et al. 1997) . In the rectangular cylinder, the differences of across wind responses between MDOF and SDOF model is small when the wind direction is normal to the short side. Torsional flutter properly occurs in the MDOF model with the side ratios of 1/2 and 1/3. In the other hand, the across-wind responses of the SDOF models are larger than those of the MDOF models when the wind direction is normal to the long side of the model. Also, the divergent vibration tends to appear at lower velocity in the SDOF model. This is explained that the vortex shedding from the SDOF model is more regular than that from the MDOF model.

The vortex-induced vibration (VIV) is summarized in the Table 2-1. The VIV is likely happened at the reduced velocity from 5-8 in square cylinder. Types of VIV was also clarified by Williamson and Govardhan (2008) in Figure 2-6.

Table 2-1: Lists of research on the vortex-induced vibration.

Author	Test	Model size	Vortex-induce vibration
Zhao (2015)	Simulation (LES)	Rectangular cylinders aspect ratio 0.3; 0.5; 0.7; 1;1.25	Reduced velocity 5-6
Bearman (1984)		Circular cylinder	Reduced velocity 6-7
Amandolèse and Hémon (2010)	Wind tunnel	Square cylinder	Reduced velocity 7-8
Williamson and Govardhan (2008)		Circular cylinder	Reduced velocity 3 ranges: initial branch: 2S mode, upper branch and lower branch: 2P mode
Brika and Laneville (1993)	Wind tunnel	Circular cylinder (cable)	2S mode: initial branch 2P mode: lower branch

Ongoren and Rockwell (1988)		Control vibration Square, triangular, circular cylinder	2P and P+S mode
Gowda and Kumar (2006)	Wind tunnel	Circular cylinder Square cylinder	Reduced velocity region 7.3 - 14
Matsumoto, Yagi et al. (2008)	Wind tunnel	Rectangular B/D = 4	Low reduced velocity 6-12
Amandolèse and Hémon (2010)	Wind tunnel	Square, high mass ratio, low damping	Reduced velocity = 5-20 VIV at Reduced velocity = 9

Note: S: Single vortex; P: Vortex pair

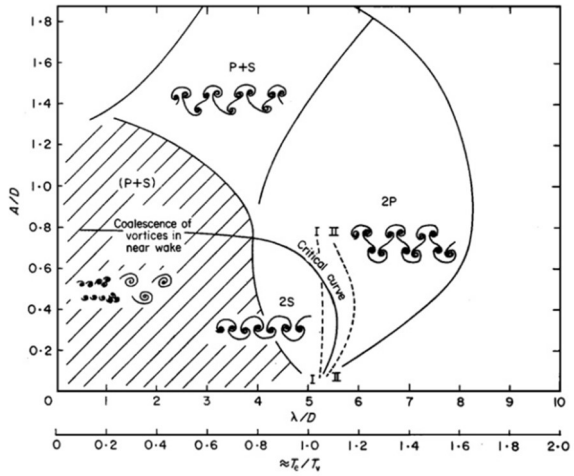

Figure 2-6: Types of vorticities (Williamson and Govardhan 2008)

The most dangerous dynamic failure may be the galloping. Parkinson and Sullivan (1979) gave the definition about the stable area and critical velocity through the Figure 2-7. In this test, the prototype height is H = 400m, St = 0.12. Line $V_{ly} = 0$ ($V_l = 0.33h^{3/2}$ m/s) expresses the velocity at the top of building which galloping begins. Line $V_{ly} = h$ ($V_l = 0.7\ h^{3/2}$m/s) expresses the velocity at top of the building which the amplitude of galloping is equal to the width of building. Finally, the line $V_{ly} = res$ ($V_l = 0.23\ h^{3/2}$m/s) which is observed for the transversion of oscillations in resonance with the vortex shedding.

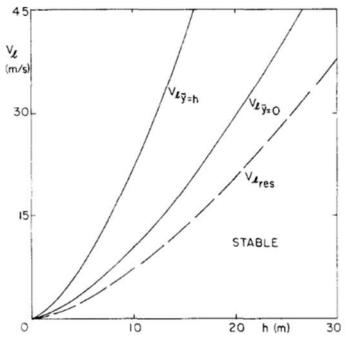

Figure 2-7: Critical wind speed for 400m tower with different width (Parkinson and Sullivan 1979)

A square section prism will gallop with amplitude increasing linearly with velocity as predicted by the quasi steady theory, at flow velocities greater than 2 or 3 times Ures. For lower velocities, if U0 is close to U_{res}, the prism will gallop with amplitudes following the same linear trend, whether or not $U_{res}<U_0$. It seems likely, then, that the quasi-steady theory can be used to predict the galloping of towers under all conditions.

Parkinson also considers the combination of the galloping effects and vortex-induced vibration (Parkinson and Wawzonek 1981). There are strong mutual effects of the two phenomena. Assuming U_{l0} is critical wind speed to generate galloping. And, U_{lr} is critical wind speed to generate Karman vortex. Then, the rectangular section and modern construction can have their critical velocity ratio $U_{l0}/U_{lr}<2$. Model will then be subjected to have strong lateral vibrations in the wind speed range $U_{lr}<U_l<U_{l0}$

Olivari (Olivari 1983) showed that only the small aspect ratio models present vortex-induced vibrations, while all the others seem likely to undergo galloping with high aspect ratio.

Corless and Parkinson (Corless and Parkinson 1988) explained about the galloping and vortex induced vibration relationship. Galloping is a low-frequency (i.e.: reduced frequency $\omega h/V<<1$), high amplitude oscillation. Vortex-induced vibration can occur for any aerodynamically bluff cylinder with an appreciable afterbody $U_r = 1/(2\pi f)$. Also, galloping occurs typically for all wind speeds above a critical wind speed U_r and significantly depends on the system damping, the mass, and the aerodynamic shape of the structure. While VIV occurs only in a specific range. Finally, the amplitudes occurring in galloping oscillations are very much larger and VIV. For example, the amplitude of the ice-covered transmission line was observed to be as much as 100 times the diameter of the line.

Simiu and Miyata (2006) also provided the conceptual diagram of vertical response and flow reattachment for rectangular cylinders in smooth and turbulence flows. The critical velocity between VIV and galloping is also calculated at $V_{cr} = 1/St$. The VIV area obtains the constant reattachment region and increase of distributed negative pressure peak. While the galloping area is observed without reattachment region and the distributed negative pressure becomes nearly uniform.

Kawai, Okuda et al. (2012) tested the flow behind the square prism 50x50x135mm. The pattern of stream line at $z/H = 1.04$ is complicated. The dividing stream line for flow over the top meets the dividing stream line from the floor. Therefore, the flow over the top does not attach on the floor. When $x/B = 0.6$, the vortex near the top still exists.

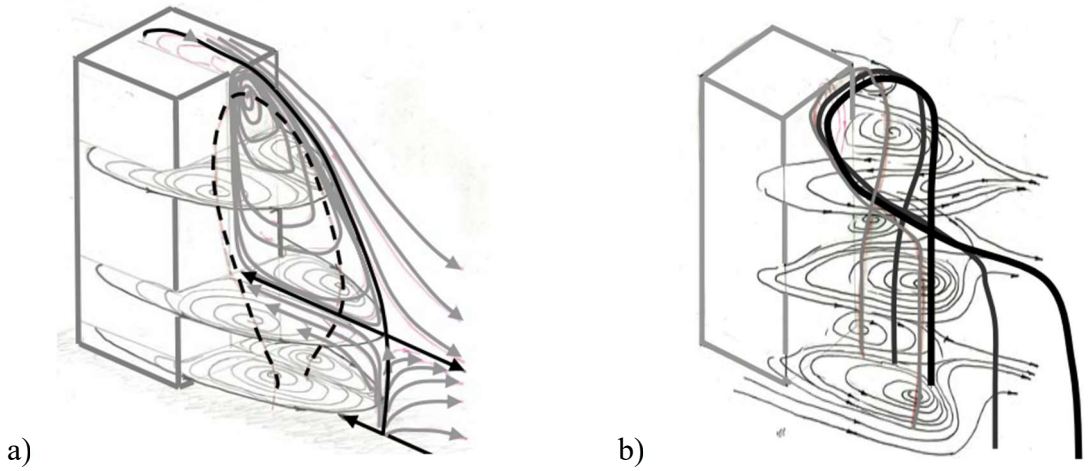

a) b)

Figure 2-8: the flow pattern after the prism cylinder a) Wake of mean flow; b) Wake of unsteady flow during Karman vortex formation behind 3D prism (Kawai, Okuda et al. 2012)

2.2.2 Interference building

When the vortex shedding frequency of the upstream structure coincides with the natural frequency of the downstream structure, large amplitude vibrations may develop. Wake galloping and wake flutter can also occur when a structure is submerged in the wake of another structure. Considered factors would be: Building 's size and shape, dynamic properties of the buildings, wind velocity and direction, type of approach terrain, location and form of the neighbouring buildings.

Regarding to interference regime, Zdravkovich (Zdravkovich 1985) proposed the distance of for stationary cylinders. x/B = 1-4: one vortex street is formed in the interference test. x/B >3 two vortices are formed. Considering to the type of fluid elastic responses, three types for two cylinders are categorized: 1) Instability rapidly builds up to extremely large amplitude in stream wise direction; 2) The amplitude is slowly built up in stream wise direction; 3) Instability gradually builds up to large amplitude in transverse direction. Sakamoto, Hainu et al. (1987) proposed another regime to classify based on vorticity. The square prism on the load cells system were set-up in the inflow boundary velocity 20m/s, turbulence intensity 0.19%. This research aimed to investigate mostly on fluctuating lift and the vortex shedding frequency: Region I: where vortices are shed from the downstream prism alone (x/B<3); Region II: where the vortices shed from the downstream prism synchronize with the ones from the upstream prism (3<x/B<27); Region III: Where the vortices are shed individually from each prism (x/B>27). For the research of interference in the Cartesian coordinator system , the distance x/B would be larger than 3 to observe the flow.

Resonant buffeting occurs when the vortex shedding frequency of the upstream interfering building coincides with the natural frequency of the principal building. The critical reduced wind velocity at which resonant buffeting occurs depends on the vortex shedding characteristics. Very large increases in both along-wind and crosswind responses have been observed in wind tunnel studies using an upstream building of different shape and smaller windward dimension to that of the principal building.

Yahyai, Kumar et al. (1992) through wind tunnel test (model 100×120×600mm, f_0=12.34Hz (100mm) 13.89 (120mm), ξ=2.5%) proved that the mean response of the principal building generally reduced due the shielding effect from the presence of an interference building, while the dynamic response usually increases. A downstream interfering building generally has very little effect on the principal building except for a small critical region. When the gap between two buildings was small enough, the channel effect may develop and impact on the principal building. In this case, the principal building goes under the elongated elliptical motions if the principal building induced the resonant type.

Taniike (1991) showed that the increase in turbulence in incident flows would reduce the interference excitation caused by a neighbouring building. Also, Blessmann (1985) in the wind tunnel test (2 model 17 stories, 96×96×417mm, f = 47.6 Hz) showed that along-wind interference factor is lower for turbulent shear flow compared to smooth flow (BF 1.45 in turbulent and 1.78 in smooth flow). And the highest RMS value does not necessarily correspond to turbulent flow. The mean surface pressures are not affected by the turbulence scale. An increase in turbulence intensity makes fluctuating surface pressure continuously increase. Reattachment length continuously shorten from the distance x/B = 5 in smooth flow to x/B = 2 in turbulence intensity of 15%. Also, through the wind tunnel experiment of Kareem (Kareem 1987), turbulence has been approved to play an important role in interference mechanism.

There is no evidence for the relationship between the wake turbulence and incident turbulence except when the scale of the incident turbulence is large enough to amplify vortex shedding. The free-shear layers which bounded by the separated wake region is strongly affected by the turbulence intensity (Bearman and Morel 1983). Moreover, Ramsey (1990) 's experiments on the effects of the wake of an upstream cylinder proved that the large eddy structures in the approach flow could amplify the vortices shed from the cylinder to a greater extent than homogeneous turbulence with the same scale and intensity. Therefore, the approaching turbulence and wake flow are sensitive to the eddy structure.

Table 2-2: Literature on the instability test of the interference building test.

Author	Test	Model size	Instability	Note
(Bailey and Kwok 1985)	Wind tunnel test	Circular, square	VIV at reduced velocity 6, buffeting factor	Along-wind and cross-wind
(Kareem 1987)	Wind tunnel test	Square 8x3x3inches	IF are more pronounced near the reduced velocity of 5	Measure on top
(Gowda and Kumar 2006)	Wind tunnel test	Circular, square	Re = 5400, Reduced velocity = 10	

Regarding to the shape of model test, Kumar and Gowda (2006) show that a square cylinder exhibits multiple amplitudes within a low and a high peak in the entire resonance range of both single and interference cylinder response. While this phenomenon is not observed in circular cylinder. A square cylinder has got a wider lock-in range and a higher (and a flatter) peak amplitude of vibration compared to the circular cylinder.

From the literature in Table 2-2, the instability happens at the reduced velocity from 5-6 in the interference test.

2.3 Computational Fluid Dynamic (CFD)

Most of researches in interference tests were done by the wind tunnel test, few reports (Peng, Zhang et al. 2012, Lam, Wong et al. 2013) mentioned about the numerical tests for more than two buildings.

Regarding the selection of turbulence model in CFD, Unsteady Reynolds Averaged Navier-Stokes (URANS) method is proved for the adequate prediction for the periodic turbulent separated flows (Isaev and Lysenko 2009). The reason to apply unsteady method is to give a non-stationary solution with the biggest motions inside the flow. The URANS equations govern the transport of the wind flow with all the scales of turbulence models. The URANS-based modelling approach significantly reduces the required computational efforts and resources. Tominaga (2015) proved that URANS could reproduce large-scale fluctuations around a high-rise building model. In addition, various of two-equations and three-equations turbulence models are added to Navier-Stock equation in the simulation of unsteady flow to simulate the flow around high-rise buildings (Ramponi and Blocken 2012). This method could improve the fluctuating results of the recirculation flow behind the building. However, the fluctuation produced by URANS and wind tunnel test still need to be validated for the actual phenomenon.

The most difficult mission for researches is to find the general solution to turbulence so that the wind flow can be simulated closely. Tests from Mochida, Tominaga et al. (2002) proved that the modified k-ε models could improve the accuracy of the separation flow on the roof better than the standard k-ε model. However, all these models tend to overpredict the recirculation flow behind the building. The k-ε v^2-f (Lien and Kalitzin 2001, Davidson 2003) and k-Ω (Wilcox 1998) is reported to produce too much turbulent kinetic energy (Heschl, Sanz et al. 2010) while the k-ε SST model can achieve well for the stagnation point.

2.3.1 Finite Volume Method

Finite Volume Method (FVM) solves the series of conservation equation as followings

The generation form of convection-diffusion-source equation

$$\frac{\partial}{\partial t}(\rho\phi) + div(\rho u\phi) = div(\Gamma grad\phi) + S_\phi \tag{2.7}$$

Replace ϕ by u_x, u_y, u_z and source we have following equation

Mass conservation:
$$\frac{\partial \rho}{\partial t} + \nabla\bullet(\rho u) = 0 \tag{2.8}$$

X momentum equation:
$$\frac{\partial}{\partial t}(\rho u_x) + \nabla\bullet(\rho u u_x) = -\frac{\partial p}{\partial x} + \nabla\bullet(\mu\nabla u) + S_{M_x} \tag{2.9}$$

Y momentum equation:
$$\frac{\partial}{\partial t}(\rho u_y) + \nabla\bullet(\rho u u_y) = -\frac{\partial p}{\partial y} + \nabla\bullet(\mu\nabla y) + S_{M_y} \tag{2.10}$$

Z momentum equation:
$$\frac{\partial}{\partial t}(\rho u_z) + \nabla\bullet(\rho u u_z) = -\frac{\partial p}{\partial z} + \nabla\bullet(\mu\nabla y) + S_{M_z} \tag{2.11}$$

Turbulence equation: URANS – standard k-ε

Kinetic energy

$$\frac{\partial}{\partial t}(\rho k)+\nabla\bullet(\rho kU)=\nabla\bullet\left(\frac{\mu_t}{\sigma_k}\nabla k\right)+2\mu_t E_{ij}\bullet E_{ij}-\rho\varepsilon \quad (2.12)$$

Viscous dissipation

$$\frac{\partial}{\partial t}(\rho\varepsilon)+\nabla\bullet(\rho\varepsilon U)=\nabla\bullet\left(\frac{\mu_t}{\sigma_\varepsilon}\nabla\varepsilon\right)+C_{1\varepsilon}\frac{\varepsilon}{k}2\mu_t E_{ij}\bullet E_{ij}-C_{2\varepsilon\rho}\frac{\varepsilon^2}{k} \quad (2.13)$$

2.3.2 Governing equation in CFD

In CFD, the governing equation of Navier-Stock equation is rewritten as:

Conservation of mass:

$$\frac{\partial\rho}{\partial t}+\nabla\bullet(\rho u_j)=0 \;;\quad In\ \ Carterian\ \ j=x,y,z \quad (2.14)$$

Conversation of momentum:

$$\frac{\partial}{\partial t}(\rho u_j)+\nabla\bullet(\rho u u_j)=-\frac{\partial p}{\partial u_j}+\nabla\bullet(\mu\nabla u)+S_{Mj} \quad (2.15)$$

Conservation of energy:

$$\frac{\partial}{\partial t}(\rho i)+\nabla\bullet(\rho i u)=-p\nabla\bullet u+\nabla\bullet(k\nabla T)+\Phi+S_E \quad (2.16)$$

Turbulence model:

$$u_x=U_x+u_x' \;;\quad u_y=U_y+u_y' \;;\quad u_z=U_z+u_z' \quad (2.17)$$

Kinetic energy k:

$$\frac{\partial}{\partial t}(\rho k)+\nabla\bullet(\rho k u)=\nabla\bullet\left(\frac{\mu_t}{\sigma_k}\nabla k\right)+2\mu_t E_{mn}\bullet E_{nm}-\rho\varepsilon \quad (2.18)$$

Viscosity dissipation ε:

$$\frac{\partial}{\partial t}(\rho\varepsilon)+\nabla\bullet(\rho\varepsilon u)=\nabla\bullet\left(\frac{\mu_t}{\sigma_\varepsilon}\nabla\varepsilon\right)+C_{1\varepsilon}\frac{\varepsilon}{k}2\mu_t E_{mn}\bullet E_{nm}-C_{2\varepsilon}\rho\frac{\varepsilon^2}{k} \quad (2.19)$$

General form:

$$\frac{\partial}{\partial t}(\rho\phi)+\nabla\bullet(\rho\phi u)=\nabla\bullet(\Gamma\nabla T)+S_\phi \quad (2.20)$$

Chapter 3

Methodology

3.1 Wind tunnel test

Wind tunnel experiments were performed in a closed-circuit wind tunnel at Yokohama National University, Japan. The tunnel testing section has a width of 1.8 m and a height of 1.8 m. Figure 3-1 indicates the general configuration of the experimental test in the wind tunnel. According to the research of Bearman and Morel (1983), the forces acting on the rectangular section in free stream turbulence flow was lower than a smooth flow. The flow of the atmospheric boundary layer was designed to simulate as a smooth flow. Figure 3-2 indicates the normalized wind velocity and turbulence intensity which were measured by a hot-wire anemometer. The vertical direction was normalized with the height of model H_0 = 600 mm. Also, the wind speed was normalized with the reference wind velocity U_0 = 3 m/s at the model height. The turbulence intensity at model height was less than 0.1 % which was considered as a smooth flow condition.

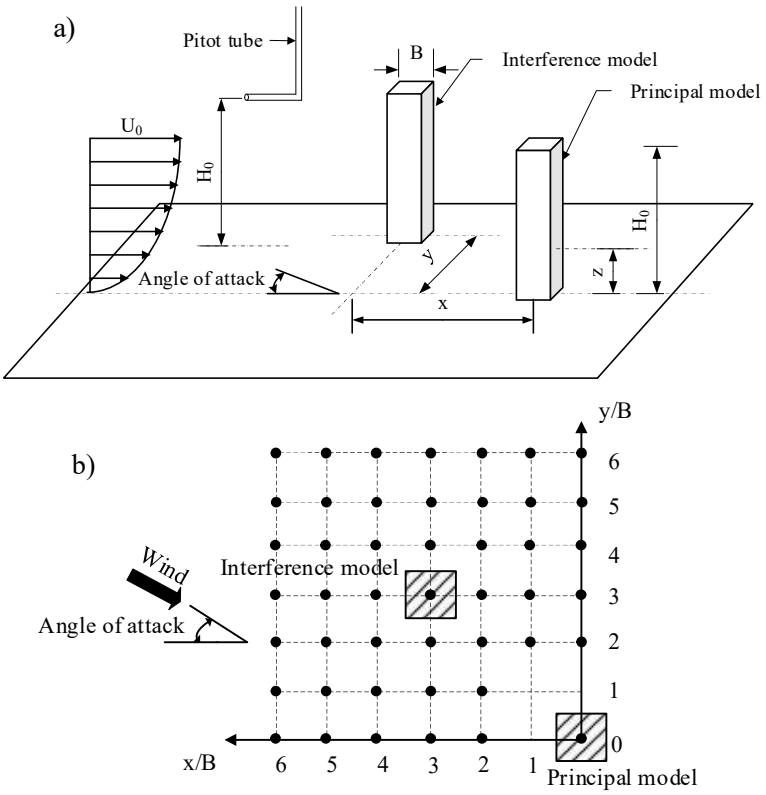

Figure 3-1: Experiment configuration: a) Schematic of the experimental program; b) Positions of interference models

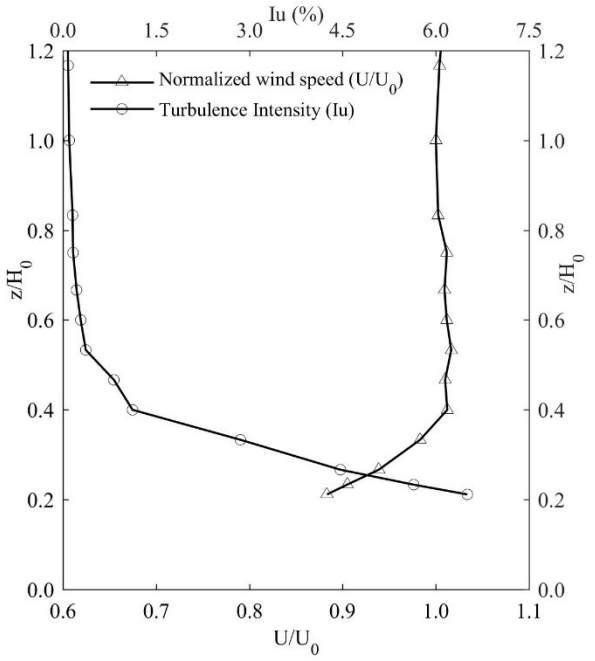

Figure 3-2: Normalized wind velocity and turbulence intensity profiles

In the static test, the velocity in the wind tunnel was calculated from the velocity in a prototype building which was estimated at 40 m/s. The velocity in the experiment at the top model height was calculated at 3 m/s by the similarity law. The Reynold number, defined by the width of the model and reference velocity, was 2.01×10^4. Ten different angles of attack were tested in different cases including 0°, 10°, 20°, 30°, 40°, 50°, 60°, 70°, 80° and 90°. An angle of 0° was represented for wind flow in the x-axis of the Cartesian coordinate. And, an angle of 90° was represented for wind flow in the y-axis of the Cartesian coordinate.

Table 3-1: Previous references of reduced velocity at instability vibration

Reference	Testing	Model size	Reduced velocity at vortex induce vibration lock-in regime
Bailey and Kwok (1985)	Wind tunnel test: Turbulence flow, open terrain	Interference square cylinder, height:width:depth = 9:1:1	6
Kareem (1987)	Wind tunnel test: Smooth and turbulence flow	Interference square cylinder, height:width:depth = 6:1:1	5-8
Gowda and Kumar (2006)	Wind tunnel test	Interference circular, square, height:width:depth = 11.6:1:1	10-12
Amandolèse and Hémon (2010)	Wind tunnel, smooth flow	Isolated square cylinder section test	8-9
Zhao (2015)	Simulation (LES), smooth flow	Rectangular cylinders with height:width = 0.3- 1.25	5-15 The VIV lock-in regime decreases with the increasing aspect ratio

In the dynamic test, the wind velocity was changed at various wind speeds. Table 3-1 shows the previous studies which were related to this study in terms of the model dimensions and wind inflow condition. A wide range of reduced velocity at VIV lock-in regime is indicated in

different tests and boundary conditions. The variation of dimensionless quantity as x/B, y/B and reduced velocity $\left(U_0/f_0 B\right)$ were used in this study. To generate the lock-in regime, the reduced velocity of the isolated model was from 0 to 20 which was equivalent to 0 to 10 m/s, respectively. And, reduced velocities from 0 to 13 were for interference cases. More than 1190 cases of different velocities and arrangements were recorded in this study.

The reference pressures including the total pressure and the static pressure were measured at the principal model height by a pitot tube. Also, wind velocity was calculated from these data sets. The total pressure of each pressure tap was synchronically measured through the acquisition system of the model MT-MP-32-R1-R ±1250 Pa, MelonTechnos company in Japan, that comprised of 32 channels. Sampling frequency and measurement time were 200 Hz and 20 s (equivalent to 10 minutes for the prototype building), respectively. The mean pressure coefficient of each pressure tap was calculated by $\overline{c_p} = \left(p - p_\infty\right)/q_\infty$, where p is the total pressure at each tap, and p_∞ and q_∞ are the reference static pressure and dynamic pressures respectively at each tap. Moreover, the displacement of the principal model was measured by a laser sensor at the top of the model with the same sampling frequency and measurement time to pressure measurement.

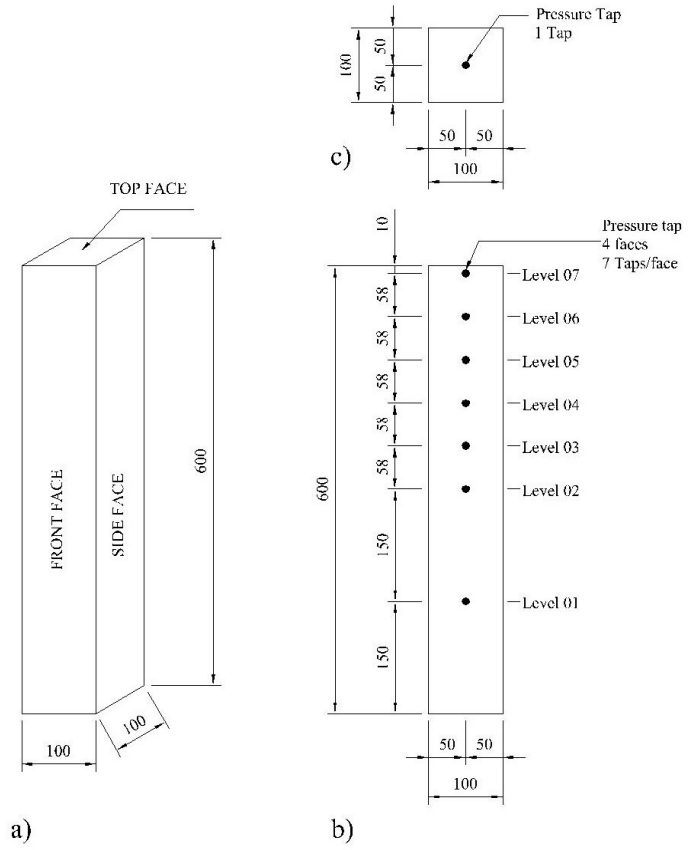

Figure 3-3: Pressure tap models a) Model sizes; b) Locations of pressure taps on side faces; c) Locations of a pressure tap on top face

The design of the prototype building was in dimensions of 40×40×240 m (width × length × height), the prototype building was assumed to have 60 floors with 4 m height at each story.

The square cross-section building models with the dimension of 0.1 m (width) × 0.1m (length) × 0.6 m (height) were used in the wind tunnel test to simulate the prototype building. This model was called the principal model or downstream model. The length scale was 1:400. Pressure taps were attached to the principal building model at all sides and on the top of the model. Twenty-nine pressure taps were installed to investigate the pressure coefficients (Figure 3-3). The principal model was pivoted at the base and restrained with springs in the rigid-aeroelastic-model system. Interference models were wooden rigid models in the same cross-section with the principal model. One model was designed at the same height of the principle model. While another was in double height. For convenience, the series of interference tests with the same height interference model was denoted as group S. On the other hand, group D was noted for interference tests of double height model.

A fundamental natural period of the prototype high-rise building was assumed as 6 s and wind speed at reference height was 40 m/s. Timescale was estimated at 1:30. The expected natural frequency of the model was 5 Hz. After the settlement of models, spring position and spring stiffness, the natural frequency of the principal model was f_0 = 5.00Hz, and damping ratio was finalized at ζ = 1.67%.

The mean interference factor (IF) for each tap at each side was used to measure the interference effect in this study. IF indicated the effect of interference model to principal model. For more details, IF = 1, the mean pressure of principal model in the isolated test was the same with the pressure of principal model in interference test. IF < 1, the appearance of interference model reduced the mean pressure on the principal model. Finally, IF >1, the appearance of interference model increased the mean pressure on the principal model. In addition, the different IF between group S and group D reflected the manner of the WOT flow because group D did not generate the effect of WOT flow. The IF was calculated by

$$\text{IF}=\frac{\text{The mean pressure coefficients for each tap in an interference test}}{\text{The mean pressure coefficients for each tap in the isolated test}}$$

In addition, a PIV system was installed to observe the velocity field in tandem arrangement cases for group S and group D. Images of smoke particles were captured by a high-speed camera at a frame rate of 1000 frames per second. These images were then analyzed by program “Flow Expert” to give instantaneous flows, time-average flows, and power spectral analysis. To get high quality images, a low velocity at the reference height at 2 m/s (U_0) was used in PIV tests.

3.2 Simulation by URANS

Turbulence model is simulated in various models to add more equations of turbulence properties to the general equation. A first-order numerical method is used for time deviation in unsteady part of the equation. The convection-diffusion problems are solved by third-order differencing scheme. Also, PIMPLE algorithm which combines between pressure-implicit split-operator (PISO) method and semi-implicit method for pressure-linked equations

(SIMPLE) is used for computational method and time integral. PIMPLE algorithm gives the implicit method to solve the equation and make irritation itself become stable.

The size of the wind tunnel is simulated in the computational domain. The grid is built based on AIJ Benchmarks for validation of CFD simulation (Tominaga, Mochida et al. 2016). Blockage ratio is fixed at 1.85% and Y+ near the wall is 7

3.3 Simulation by LES

Large Eddy Simulation (LES) is used for more precious solution. The computational effort on each calculation is still a challenge to engineer due to time-costly simulation. LES method is based on the derivation of the incompressible Navier-Stokes equation.

Inflow boundary condition is still a major barrier in LES simulation. The simulation needs to reach the target of turbulence intensity, inflow spectra with the real test. Consistent discrete random inflow generation (CDRFG) recently developed by many researcher (Huang, Li et al. 2010, Aboshosha, Elshaer et al. 2015).

Velocity is generated from

$$u_i\left(x_j,t\right)=\sum_{m=1}^{M}\sum_{n=1}^{N}p_i^{m,n}\cos\left(k_j^{m,n}.x_j^m+2\pi f_{n,m}t\right)+q_i^{m,n}\sin\left(k_j^{m,n}.x_j^m+2\pi f_{n,m}t\right) \quad \textbf{(3.1)}$$

With $x_j^m=\frac{x_j}{L_J^m}, L_j^m=\frac{U_{av}}{\gamma C_j f_m}$

The idea of this method is to calculate from the energy spectrum of fluctuating wind speed in each direction by Von Karman model.

$$S_u\left(f\right)=S_v\left(f\right)=S_w\left(f\right)=\frac{4\left(IU_{avg}\right)^2\left(L/U_{avg}\right)}{\left[1+70.8\left(fL/U_{avg}\right)^2\right]^{5/6}} \quad \textbf{(3.2)}$$

Then the constant number $p_i^{m,n}$ and $q_i^{m,n}$ is calculated as

$$p_i^{m,n}=sign\left(r_i^{m,n}\right)\sqrt{\frac{1}{N}S_{ui}^m\Delta f\frac{\left(r_i^{m,n}\right)^2}{1+\left(r_i^{m,n}\right)^2}} \quad \textbf{(3.3)}$$

$$q_i^{m,n}=sign\left(r_i^{m,n}\right)\sqrt{\frac{1}{N}S_{ui}^m\Delta f\frac{1}{1+\left(r_i^{m,n}\right)^2}}$$

Moreover, vector k is generated as random Gaussian numbers with zero mean and unit standard deviation to satisfy the following criteria:

$$\begin{bmatrix} p_x^{m.n} & p_y^{m.n} & p_z^{m.n} \\ q_x^{m.n} & q_y^{m.n} & q_z^{m.n} \\ k_x^{m.n} & k_y^{m.n} & k_z^{m.n} \end{bmatrix} \begin{Bmatrix} k_x^{m.n} \\ k_y^{m.n} \\ k_z^{m.n} \end{Bmatrix} = \begin{Bmatrix} 0 \\ 0 \\ 1 \end{Bmatrix} \quad \textbf{(3.4)}$$

With M is the number of spectral segments; N is the number of random frequencies within each segment; $f_{n,m}$ is a normally distributed random number with zero mean and f_m standard deviation; $k_i^{m,n}$ is coordinates of a uniformly distributed points on a sphere with a unit radius.

Chapter 4

Wind Tunnel Experiment

4.1 Prototype building

Prototype building is ideally proposed. Structural information is as blow:

- Building height: 240m
- Plan: 40x40m
- Floor height: 4m
- Number of stories: n = 60
- Design code: ASCE 07-05
- System: RC shear wall system + braced mega column, floor is very stiff in lateral displacement.

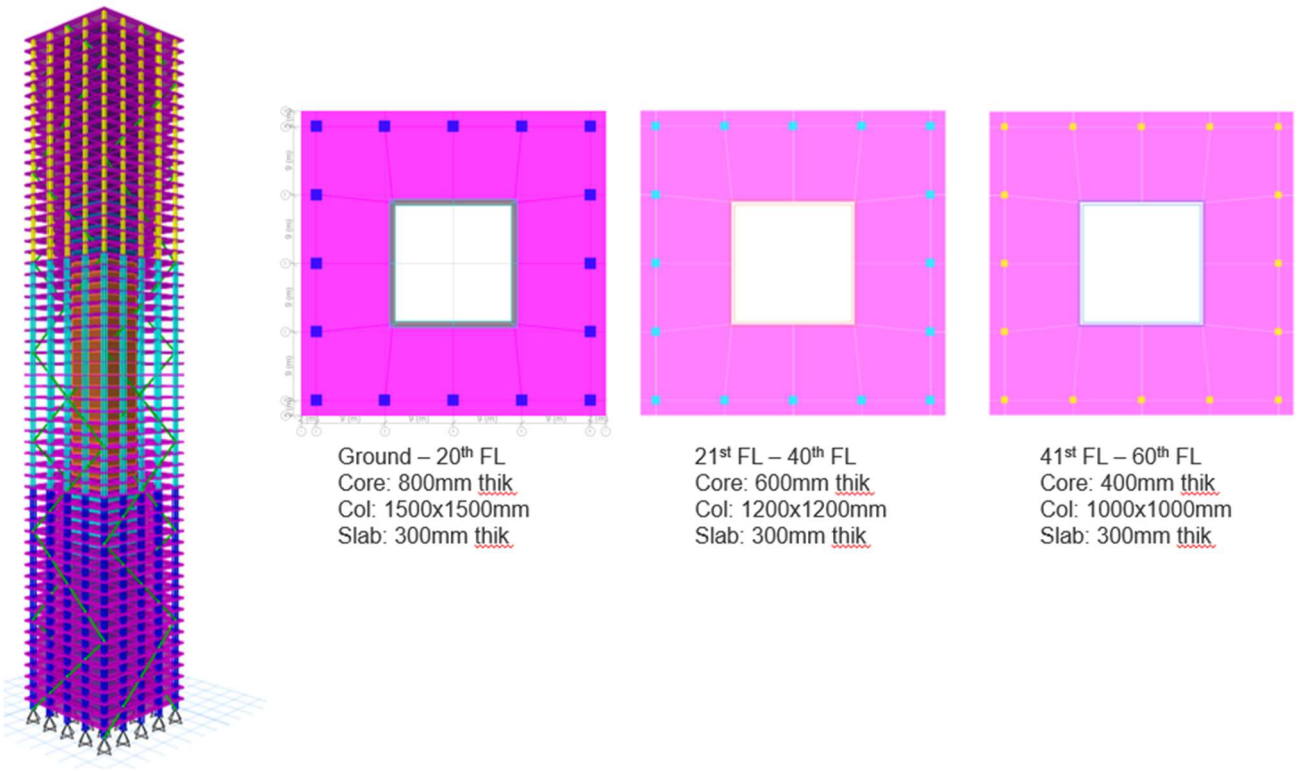

Figure 4-1: Structural system

Basic parameters after design:

- Building mass (DL+0.5SDL+0.15LL): 106,548 tons
- Density: 277kg/m3

4.1.1 Dynamic parameters in FEM model

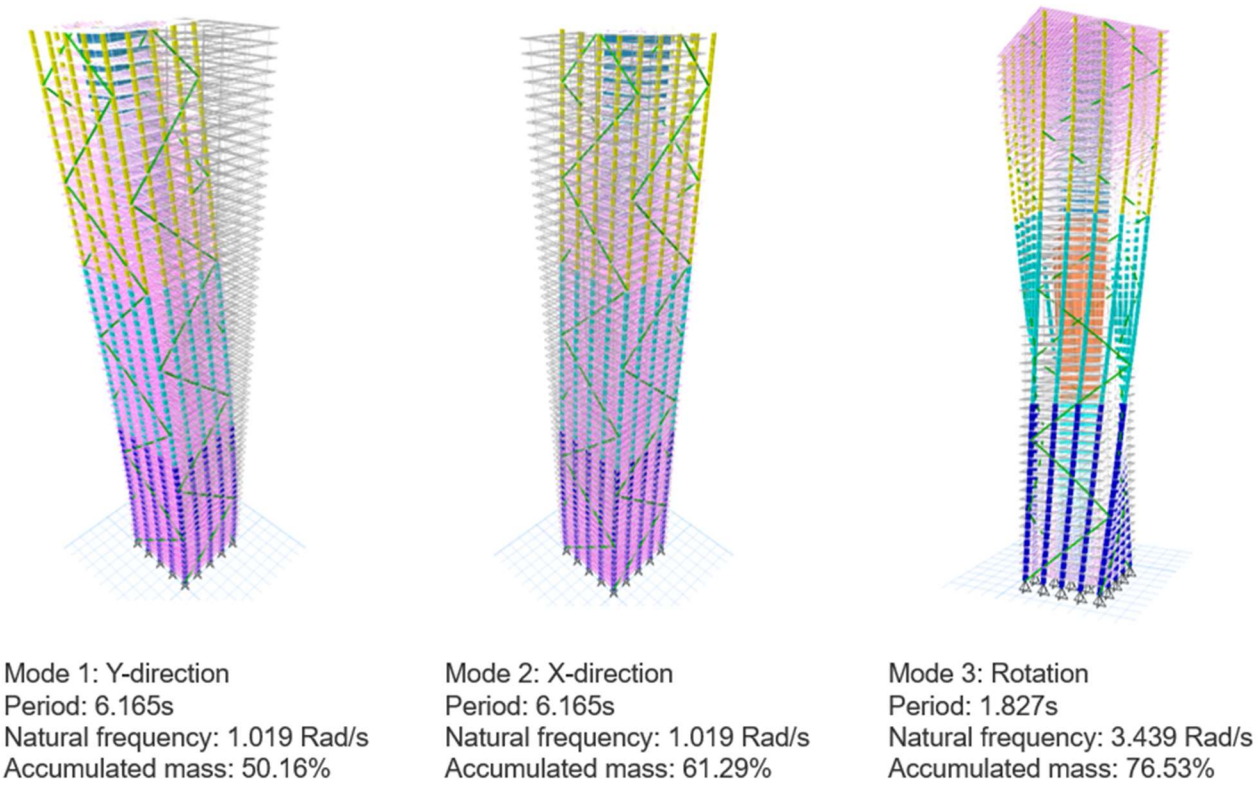

Figure 4-2: First 3 periods of building

Because in design of ETABS, it is hard to control damping. There is also internal damping which is the interaction of materials. MDOF analysis is used to compare the results.

4.1.2 Dynamic parameters in MDOF

By considering the floor is rigid, each floor contains three degree-of-freedom including longitude, transvers and torsion. Figure 4-3 shows the information of MDOF model in three direction of the prototype building.

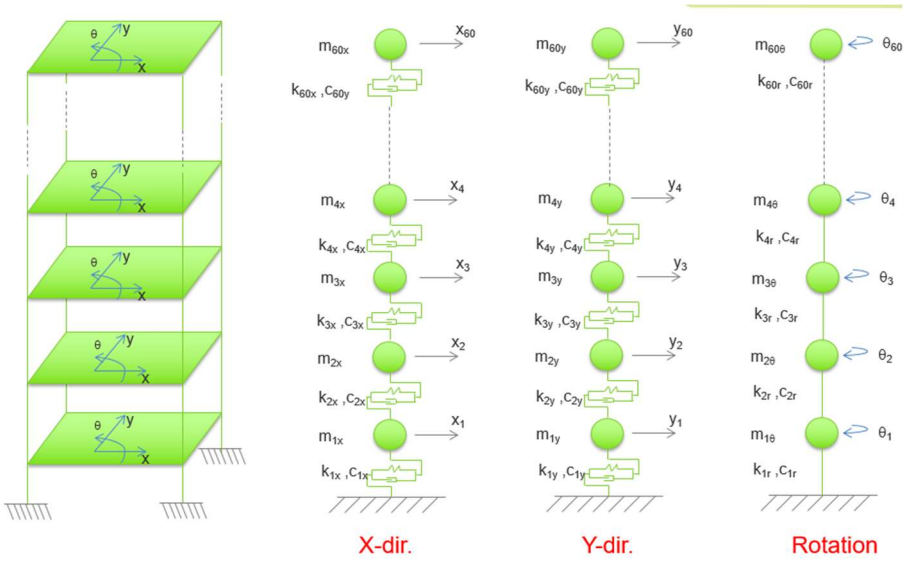

Figure 4-3: MDOF analysis

The equation of motion is written in Figure 4-4. Due to the symmetry structure in both x and y direction, first mode and second mode has same behaviour at period of 6s.

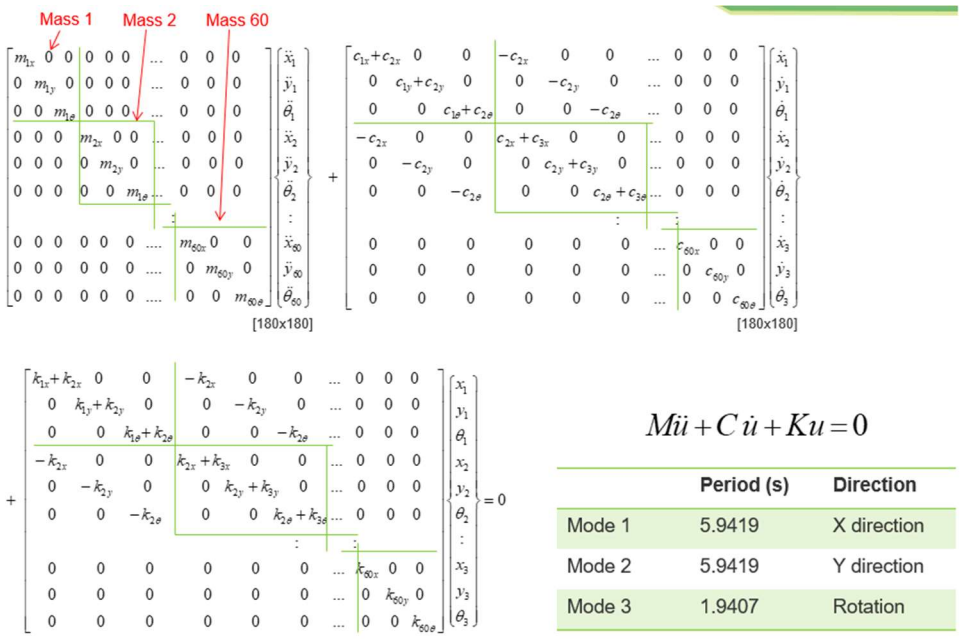

	Period (s)	Direction
Mode 1	5.9419	X direction
Mode 2	5.9419	Y direction
Mode 3	1.9407	Rotation

Figure 4-4: Equation of motion

4.1.3 The estimation of ACSE

In ASCE, equation 12.8-8, the approximation fundamental period of building in which the seismic force – resisting system entirely with concrete moment resisting frames is

Ta = 0.1 N, N is the number of building.

Ta = 0.1 × 60 = 6s

Compare all methods

Table 4-1: The comparison of first period of prototype building.

	FEM model	MDOF	ASCE
	Period (s)	Period (s)	Period (s)
Mode 1	6.165	5.942	6
Mode 2	6.165	5.942	
Mode 3	1.827	1.941	

4.2 Model calculation

A rigid-aerodynamic-model system (Figure 4-5) was designed based on an idea of semi-rigid models firstly presented by Balendra and Nathan (1987). The system was assembled by aluminum materials. The natural frequency of structure possibly varied from 0.78 Hz – 10.58 Hz. The stiffness was able to be modified by the mass of the model, the position of springs and spring stiffness. Oil damping and damping cards were used to control the damping of the model. Different oil damping viscosities and sizes of damping cards gave different damping ratios to structures. The vibration of the model could be measured by laser transducers through the moving of a damping card under the wind tunnel floor or the moving of top of the model upper the wind tunnel floor. With this system, the instability vibration like vortex-induced vibration (VIV) or wake galloping could be measured.

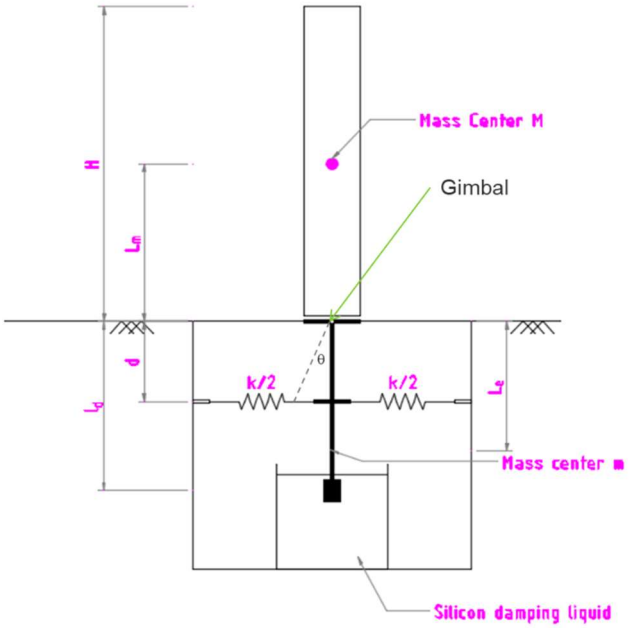

Figure 4-5: Parameters of elastic system

Using similarity law to scale down the prototype building.

- Mass modelling

- Effective bulk density $\left(\frac{\rho_s}{\rho}\right)_m = \left(\frac{\rho_s}{\rho}\right)_p$
- Generalized mass $\frac{M_m}{M_p} = \frac{\rho_m}{\rho_p}\frac{L_m^3}{L_p^3}$
- Mass moment of inertia scaling $\frac{I_{Mm}}{I_{Mp}} = \frac{\rho_m}{\rho_p}\frac{L_m^5}{L_p^5}$

• Damping

- Similarity of dissipative or damping force $\zeta_m = \zeta_p$

• Stiffness scaling

- By maintaining the cauchy number, $\left(\frac{E_{eff}}{\rho V_{wind}^2}\right) = cons\tan t$,

  $E_{eff} = \frac{E\tau}{L};\ \frac{EA}{L^2};\ \frac{EI}{L^4}$
- Flow velocity $\frac{V_m}{V_p} = \left(\frac{E_{effm}}{E_{effp}}\frac{\rho_p}{\rho_m}\right)^{1/2}$
- Reduce frequency $\left(\frac{\omega_0 L}{V_{wind}}\right)_m = \left(\frac{\omega_0 L}{V_{wind}}\right)_p$

• Time scale $\frac{T_m}{T_p} = \frac{L_m}{L_f}\frac{V_f}{V_m}$

The definition of stick aeroelastic model is firstly mentioned in (Zhou and Kareem 2003). Kim and Yoon (2014) used stick aeroelastic model in their wind tunnel study with model 56x56x448mm, natural frequency is 5.6Hz in each size. This research with model 100x100x600mm, targeted natural frequency is 5Hz in both axis.

In MDOF high rise building research, (Yoshie, Kawai et al. 1997) and (Templin and Cooper 1981) suggested that natural frequency of 2 first modes of high rise building model should be less than 10 Hz.

By taking velocity of prototype building in Yokohama area (V= 40 m/s) and time scale to reduce is 1/30

Table 4-2: Similarity law to scale down model

	Prototype	SDOF Model
Size (m)	40x40x240	0.1x0.1x0.6
Volume (m3)	384,000	0.006
Wind speed (m/s)	40	3
Period T (s)	6	0.2
Natural frequency ω (Rad/s)	1.047	31.416
Frequency f (Hz)	0.17	5.00
Density r (kg/m3)	275	275
Mass M (kg)	105,600,000	1.65
Stiffness K (N/m)	115,803,358	1628.48
	118.05 tonf/cm	1.66 kg/cm
Damping ratio ξ	1.00%	1.00%
Damping C (Nm/s)	2.212E+06	1.037
Min reduced velocity	5	5
Min velocity (m/s)	33.33	2.50
Min Reynold number	89,333,333	16,750
Max reduced velocity	15	15
Max velocity	100	7.5
Max Reynold number	268,000,000	50,250

4.2.1 Equation of motion

Using energy method (Lagrange Equation) to find equation of motion

– Potential energy

$$V_m = MgL\left(\cos\theta - 1\right) + mgL_e\left(1 - \cos\theta\right) + \frac{1}{2}kd^2\sin^2\left(\theta\right)$$

– Kinetic energy

$$T = \frac{1}{2}ML_m^2\dot{\theta}^2 + \frac{1}{2}mL_e^2\dot{\theta}^2$$

– Dissipation function

$$F_d = \frac{1}{2}cl_d^2\theta^2$$

– Apply Lagrange equation

L = T - V

$$\frac{\partial}{\partial t}\left(\frac{\partial L}{\partial \dot{\theta}}\right) - \frac{\partial L}{\partial \theta} + \frac{\partial F_d}{\partial \theta} - X_i = 0$$

$$\left(ML_m{}^2 + mL_e{}^2\right)\ddot{\theta} + MgL_m\left(-\sin\theta\right) + mgL_e\left(\sin\theta\right) + kd^2\sin\theta\cos\theta + cl_d^2\dot{\theta} = f\left(t\right)$$

Linearize to equation of motion

$$\sin(\theta)=\theta;\ \cos(\theta)=1$$

$$\left(ML_m^{\,2}+mL_e^{\,2}\right)\ddot{\theta}+cl_d^{\,2}\dot{\theta}+\left(mgL_e-MgL_m+kd^2\right)\theta=F(t)$$

4.2.2 Properties of elastic system

The elastic system is designed for wide range working of frequency and damping ratio. Thus, this system is used for multipurpose study working on the different types of building model.

Table 4-3: Working range of elastic system and estimated data for the tested model

Properties		From		To	Tested model
1. Mass of model (kg)	M	2.00	-	1.00	1.41
2. Center model to pivot (m)	Lm	0.30	-	0.30	0.30
3. Mass of stick (kg)	m	0.84	-	1.01	1.01
4. Dist. pivot to center mass stick (m)	Le	0.06	-	0.16	0.06
5. Dist. to damping (m)	ld	0.47	-	0.49	0.49
6. Damping coefficient (Ns/m)	c	0.05	-	3.71	0.34
7. Spring stiffness (N/m)	k	981.00	-	9,810.00	5886
(kg/cm)		1.00	-	10.00	**6.00**
8. Dist. pivot to spring (m)	d	0.10	-	0.23	**0.15**
9. Total mass (kgm)	Mt	0.18	-	0.12	0.131
10. Total damping (Ns/m*m)	Ct	0.01	-	0.91	0.08
11. Total stiffness (N/m*m)	Kt	4.41	-	515.36	128.86
12. Natural frequency (Rad/s)	ω	**4.91**	-	**66.47**	31.42
13. Period (s)	T	**1.28**	-	**0.09**	0.20
14. Frequency (Hz)	f	**0.78**	-	**10.58**	5.00
15. Damping ratio (%)	ξ	**0.58**		**5.85**	1.00

Note that: Equation of motion $\left(ML_m^{\,2}+mL_e^{\,2}\right)\ddot{\theta}+cl_d^{\,2}\dot{\theta}+\left(mgL_e-MgL_m+kd^2\right)\theta=F(t)$

$$M_t\quad\ddot{\theta}+C_t\ \dot{\theta}+\quad K_t\quad\theta=F(t)$$

4.2.3 Estimation of displacement on top of model

Since there is no wind profile at current time, the static wind load is used to apply on equation of motion. In dynamic test, the reduce velocity in range of 5-15 which means that the velocity in range of 2.5 to 7.5 m/s

- Wind velocity: U = 2.5 m/s to U = 7.5 m/s
- Drag coefficient: $C_d = 1.05$
- Area: A = 0.06 m^2
- Wind load $\frac{1}{2}\rho U^2 C_d A = 0.2412N \quad to \quad 2.1705N$

Apply Newmark beta constant, the estimation of displacement on the top of model is ploted.

The mean of displacement in case of U = 2.5m/s: 7.38 mm

The mean of displacement in case of U = 7.5m/s: 66.42 mm

Amandolese (Amandolèse and Hémon 2010) did the wind tunnel test on flexible square cylinder, the results show that the maximum displacement of building (20x20x150mm) is 0.2%. Gowda (Gowda and Kumar 2006) showed that peak oscillatory amplitudes can be nearly three times that for the isolated cylinder in both square and circular cylinder

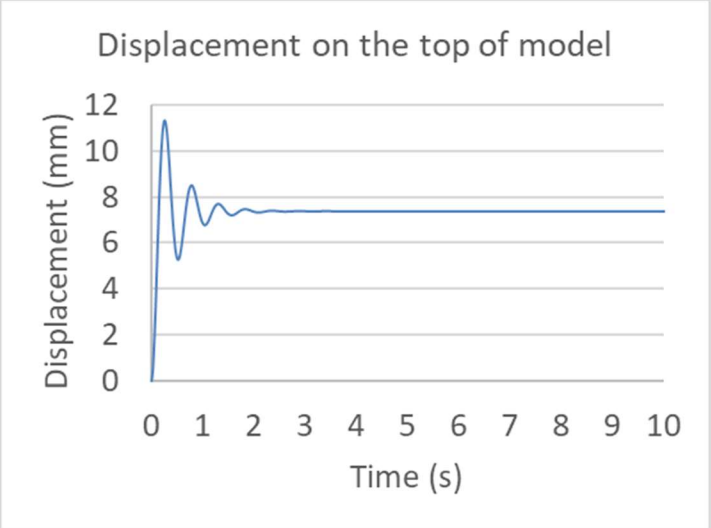

Figure 4-6: Displacement on the top of model at U =2.5 m/s

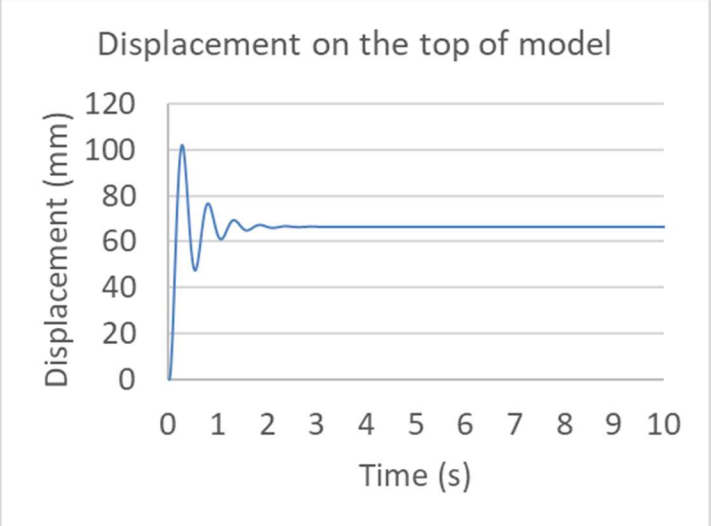

Figure 4-7: Displacement on the top of model at U = 7.5m/s

4.3 Validation with previous studies

To check the reliability of the wind tunnel test, the results of pressure coefficients and displacement of the principal model in the isolated test and interference tests are compared to previous studies. The selected works of literature are in same flow conditions and model section test with this present study: Square cylinder and smooth flow condition.

4.3.1 Validation of pressure coefficients

The local pressure coefficients of each side of the square cylinder in different studies are compared in Table 4-4. Bearman and Obasaju (1982) and Nishimura and Taniike (2000) provided the distribution of pressure coefficients along the cross-section of the square cylinder. The pressure coefficients of each side are recalculated by deducting the value of the first measurement point. This present study shows the satisfactory results to previous studies. The slight differences still can be found in the table because of the differences of blockage percentages and the turbulence intensity in wind tunnel tests.

Table 4-4: Comparison of pressure coefficient of present study with previous studies

References	Front	Side	Rear
Bearman and Obasaju (1982)	1.080	-0.780	-0.680
Nishimura and Taniike (2000)	1.000	-0.730	-0.615
Present study	1.086	-0.741	-0.668

4.3.2 Validation of interference factors

The IFs in tandem arrangements are plotted in Figure 4-8 for comparison. Xie and Gu (2004) conducted the wind tunnel test with smooth flows for square tall buildings. However, the IFs in their research were calculated based on the overturning moment in along-wind direction. The overturning moment in along-wind direction of this present study is then calculated by $OM = \sum U_0 \times \overline{c_p} \times A \times d$ where U_0 is reference velocity at the model height, $\overline{c_p}$ is mean pressure coefficient of each tap in the front and rear face, A is the distribution area of each pressure tap, and d is the distance from pressure tap to the pivot point of SDOF. Then, IFs are calculated and compared to the results of Xie and Gu (2004). The positive values of IFs show the sign of overturning moment in interference tests are in the same with the isolated test. While the negative values of IFs present the overturning moment in interference tests are opposite with the isolated test. In the graph, differences at x/B= 3 and 6 is explained by the limitation of pressure taps on faces, which could not present for all pressure loads on the principal model. However, the trend of IF in both studies still shows the increase and well agreement.

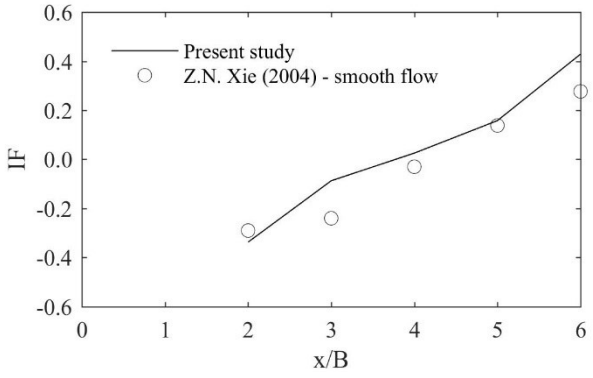

Figure 4-8: Validation of interference factors in tandem arrangements

4.3.3 Validation of displacement in dynamic tests

The aerodynamic system is also validated with the results from interference effect tests of Taniike (1991). Figure 4-9 indicates the RMS displacement of the isolated test and the

interference test of same height models (x/B = 6) in various reduce velocities. In both cases, the reduced velocity which causes the instability vibration can be seen at the same point. The difference in the mass-damping parameter as Scruton number may reflect the different behaviours in vibration. Scruton number in this study is defined as $S_c = 4\pi \frac{m_m}{\rho B^2}\zeta = 8.5$, where m_m is the model mass ratio, B is the width of the model, ρ is the air density, and ζ is the damping ratio. Mannini, Marra et al. (2017) mentioned that the range of excitation due to VIV and galloping fully clarify in high Scruton number. In low Scruton number, it is difficult to distinguish clearly the velocity range which causes galloping or VIV.

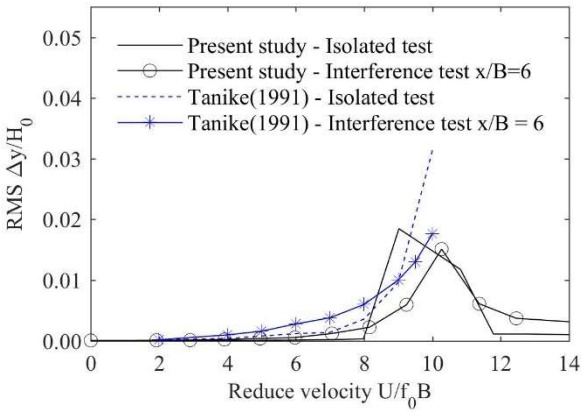

Figure 4-9: Comparison of single and interference case for RMS displacement in different reduced velocity

4.4 Results and discussion

4.4.1 Mean pressure coefficient in tandem arrangements

Figure 4-10 shows the mean pressure coefficient $\overline{c_p}$ of pressure taps along the height of front, rear and side faces of the principal model in tandem arrangements of isolated case, group S and group D cases. The data sets in the front face present the trend of WOT flow clearly. In interference tests, most of the pressure coefficients in the front face of the principal models show negative value compared to positive pressures on the front face of the isolated test. These positive pressures on the front face and negative pressures on the rear face makes the drag coefficient of the whole model turn to a negative value. These results agreed well with the research of fluctuating forces on square prisms of Sakamoto, Hainu et al. (1987). Moreover, the upstream models produces remarkable shielding effect on the downstream model in the along-wind direction (Xie and Gu 2004).

When the interference models locate near the principal model at distance of x/B = 2, no significant difference between group S and group D is found. The WOT flow has no effect to the principal model in these cases. All positions of pressure taps indicate negative pressures. The shear layer which is formed from the separation point at top of the interference model in tests of group S could not reach to the front face of the principal model. From x/B = 3 to 6, the pressure coefficients of the principal model in group S change gradually in each distance. The areas near the top firstly turn to positive pressure at distance x/B = 3. In this case, the shear

layer from WOT flow could move downward and reach the front face of the downstream model. When interference models in group S move further away the principal model, the area of positive pressure on the principal model increased with the increase of the distance. On the other hand, group D without effects of WOT flow does not show this apparent trend. Pressure taps in groups S clearly prove the existence of arch-type vortex behind the flat-roof interference building as discussed by Kawai, Okuda et al. (2009).

At rear and side faces, most of the cases indicate that the negative pressure in group D is lower compared to group S. Meanwhile, the rear face and side faces of the principal model in group S receive more pressure than group D due to the presence of 3-D flow combination of the WOT flow and Karman vortex. It is noted that interference models in group D only produce Karman vortex which moves downward and impacts on the sides of the principal model. This Karman vortex has no action on the rear sides at close distance as x/B = 2. Obviously, pressure coefficients in this closed arrangement indicate the same value with the isolated model case. Shifting interference models to distance x/B = 3 to 6, Karman vortex shows its effects clearly on rear and side faces. At this moment, the differences of pressure coefficients between the isolated test and group D interference test are more apparent. Therefore, Karman vortex represents its effects in the distance larger than x/B = 3 in these interference tests.

Both the front side and rear side face of the principal model get impacts from the arch-type vortex which is only generated from group S test. At the rear side, this vortex helps to reduce pressure force in short distances which are less than 4B. In long distance, the arch-type vortex loses its energy to contribute continuously to the pressure on the rear face. Pressure coefficients show no significant difference at the rear face between group S and group D. On the other hand, the side faces are interesting to observe the mixing of both Karman vortex and the WOT flow. However, the value of pressure coefficients in all cases become slightly complicated to compare. Like the rear face, the effects of arch-type vortex reduce when the interference models located far away from the principal model. In general, the WOT flow shows its existence clearly in distance x/B = 3 to 5 in all sides. These results could contribute to the building code for cladding design in the urban area and estimate the dimension of the arch-type vortex.

From these results, all area of cladding designs should not be designed as positive pressure only as in isolated case or negative pressure only as shielding effect from upstream building. Due to the impact of the WOT, the top area should be designed in positive pressure and bottom area should be designed as negative pressure in the urban area with all same height building. The area near the top which is needed to be strengthened with positive pressure is accounted for 21% $\left(\frac{10+58+58}{600}\right)$ the area of the front face. It is also noted that the WOT flow only contribute the positive pressure to the principal model. This contribution could reach to 62.31% $\left(\frac{\text{mean all pressure tap group S}-\text{mean all pressure tap group D}}{\text{Mean all pressure tap in isolated test}}\right)$ of pressure value compared to the isolated case.

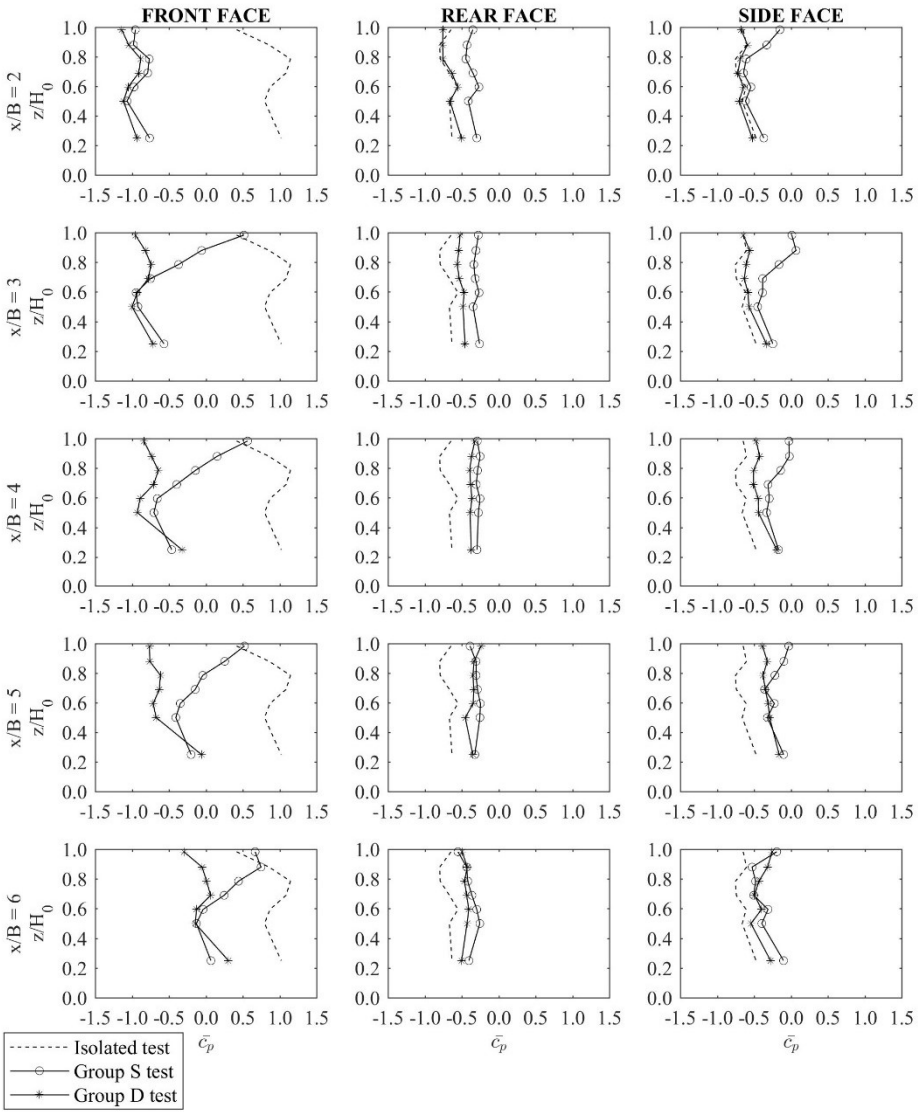

Figure 4-10:Pressure coefficients on the front face of the principal model in tandem arrangements considering different interference models

The mean of pressure coefficients in different angles of attacks in tandem arrangement cases is represented in Figure 4-11. In general, the mean of pressure coefficients of group S and group D indicate a similar trend as the angle varied from 30° to 60°. The distance in across-wind direction between models should be put into the consideration to explain for these results. When the angle of attack becomes wider, the distance between the interference model and the principal model also increases in the normal direction of wind flow. In these cases, there is a chance that the WOT flow could not reach the principal model. Thus, pressure coefficients in all faces hold similar values between group S and group D when the angle of attack is within 30° to 80°. However, Figure 4-11 indicates the gap between group S and group D when the angle of attacks is 0° to 20°. It is noted that the difference between tests of group S and group D is the effect of the WOT flow in contribution to the principal model. Therefore, the WOT flow produces significant effects on cladding pressures of the principal model for angles of attack from 0° to 20° in interference tests. Moreover, the difference of pressure can be found at

90° angle of attack in the vicinity of x/B. The reason for this phenomena could be explained by the channeling effect (Kim, Tamura et al. 2013).

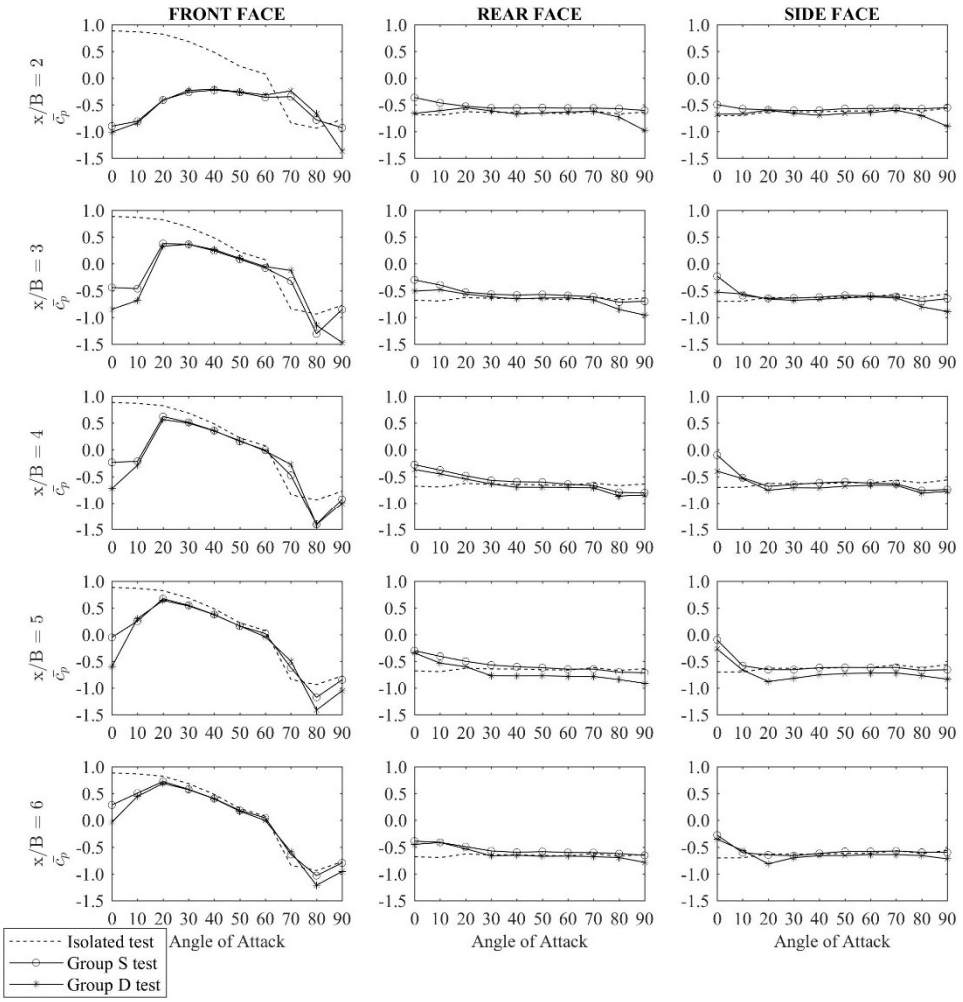

Figure 4-11: Mean pressure coefficients in tandem arrangements in different attack angles

4.4.2 Interference factors

The major contribution can be observed in the graph of y/B = 0, 1 and 2. The WOT flow increases the pressure on the front face of the principal model. This flow is generated from the upstream interference model. After leaving the leading edge, the shear layer of the WOT flow is formed and moved downward to the principal model. The different IF between group S and group is 0.11 to 0.55 in tandem arrangement y/B = 0; 0.09 to 0.27 in stagger arrangement y/B = 1, and 0 to 0.11 in stagger arrangement y/B = 2 case. A light difference in the far distance x/B = 6 case in graph y/B =2 still can be found. There is a similar phenomenon in the previous finding when the WOT flow could have effects on the principal model within 20 ° angle of attack.

The highest difference of IF (0.55) could be observed at the position of x/B = 5 in tandem arrangement. Thus, the most contribution of the WOT flow can be found when the interference model located at x/B = 5; y/B = 0. These significant numbers would be an important addition in the cladding design of high-rise buildings to avoid the damages by wind in the urban area.

At the farthest distance in tandem arrangement x/B = 6, the difference of IF between two group can still be observed. Therefore, the longer domain in along-wind direction would need to be conducted in our future research.

4.4.3 Effects of interference model's position to the WOT flow

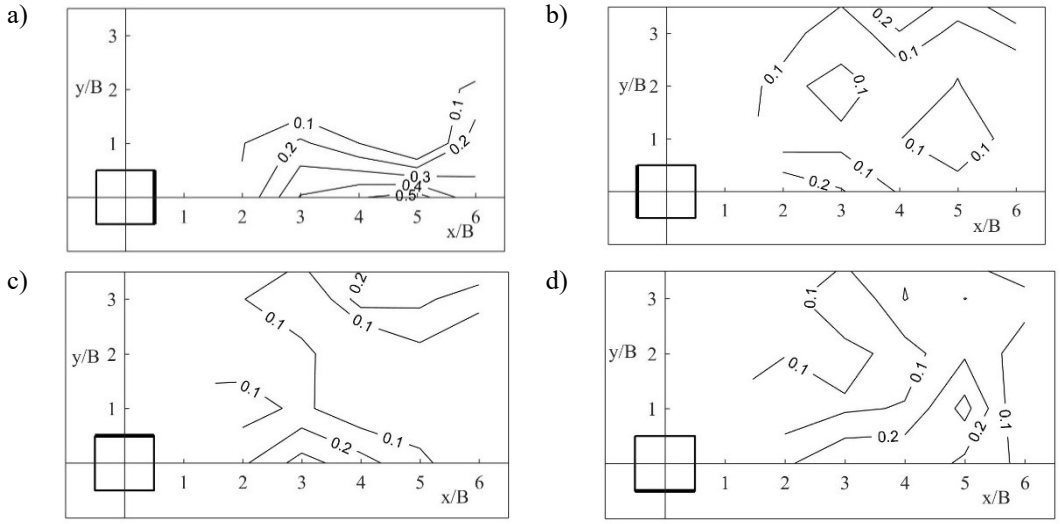

Figure 4-12: The different pressure coefficient of group S to group D: a) Front face; b) Rear face; c) Left-side face; d) Right-side face

As mentioned, the WOT flow is researched through the same height interference model. However, the same height interference model generates both side effects and top effects. To research the WOT flow separately, the double height interference model which only generates side effects to the principal model is also put into the concern to compare. In each position of interference models, the mean of pressure coefficients on each face is calculated. Then, the subtraction of the mean pressure coefficient in group S and mean pressure coefficient in group D is a possible value to evaluate the effect of WOT flow on each face. To have a general view of all faces, these subtraction values are represented in the form of contour lines by the linear interpolation method. Figure 4-12 shows the contour lines on each face. Meanwhile, these contour lines indicate the possible areas where the WOT flow could have the distribution on the principal model. The values of contour lines show how much the WOT flow contribute to the mean pressure coefficient on faces. The following findings are obtained from the comprehensive analysis.

1) The front face is the face which receives the most influence from the top flow. The strength of WOT flow could contribute 46% (at position x/B = 5, y/B =0; 0.5/1.086×100) of mean pressure coefficient on the front face.
2) The WOT flow contributes not only to the font face but also to other faces. Unlike the front face, the effects from positions of interference model could not be predicted clearly. However, the contribution level of WOT flow is more than 20% to the mean of face pressure coefficient. Also, the effects from positions of the interference models do not indicate the clear trend at the rear and side faces.
3) The combination of WOT flow and Karman vortex poses a considerable difficulty for cladding design in high-rise buildings. The influence of WOT flow to the principal building clearly cannot be neglected in all sides near the top of the model. Strengthening claddings of the principal model is needed if any building is built within the affected

area which is shown in Figure 4-12. Moreover, the design of the roof needs to consider the aerodynamic shape to avoid or reduce the pressure from the shear layer of WOT flow.

4.4.4 Dynamic tests

VIV is investigated in the across-wind direction in various reduce velocities. The top displacement of the principal model is recorded in the isolated case and interference cases. Figure 4-13 represents the RMS displacement in the form of a dimensionless unit by dividing the RMS displacement by the height of the principal model. In most cases, the interference tests reduce the amplitude of vibration on the principal model compared to the isolated test. These reductions are explained by the shielding effect. Two important results could be obtained as follows.

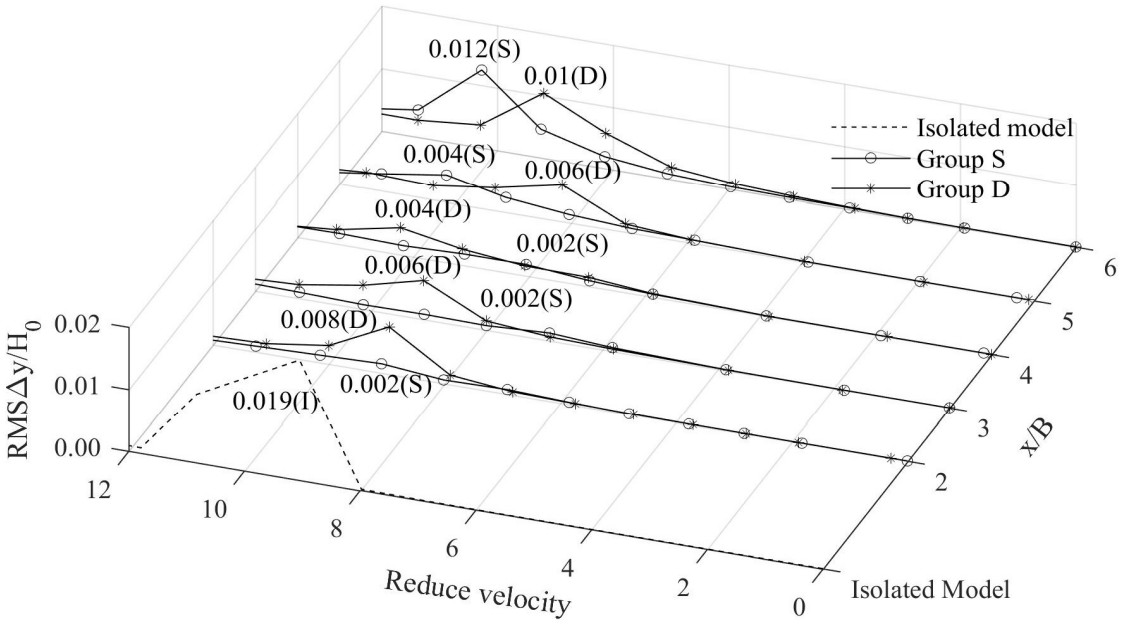

Figure 4-13: RMS displacement in various reduce velocities in tandem arrangements: (I): Isolated model; (S): Group S; (D): Group D

1) When two models in group S are in distance x/B ≤ 4 in the tandem arrangement, the VIV still occurs but with very small amplitude of vibration. The amplitude of VIV in these cases is not much different with the amplitude in adjacent velocity. On the other hand, group D shows the clear peak of the amplitude in VIV. The reason could be explained that the interference model in group D produces the Karman vortex which causes the vibration of the downstream model. While the Karman vortex in group S is mixed with the WOT flow so that the effect of Karman vortex on the downstream model is reduced.
2) In farther distance, x/B>4, the VIV in group S occurs in higher velocity than group D. Moreover, the amplitude at VIV of group S increases significantly. The oscillation is more pronounced when interference models are at the distance x/B = 6. At x/B = 5 and x/B =6, the appearance of the WOT flow properly makes the principal model vibrate at higher reduced velocity. Meanwhile, the building can resist larger velocity before turning to instability vibration on the site.

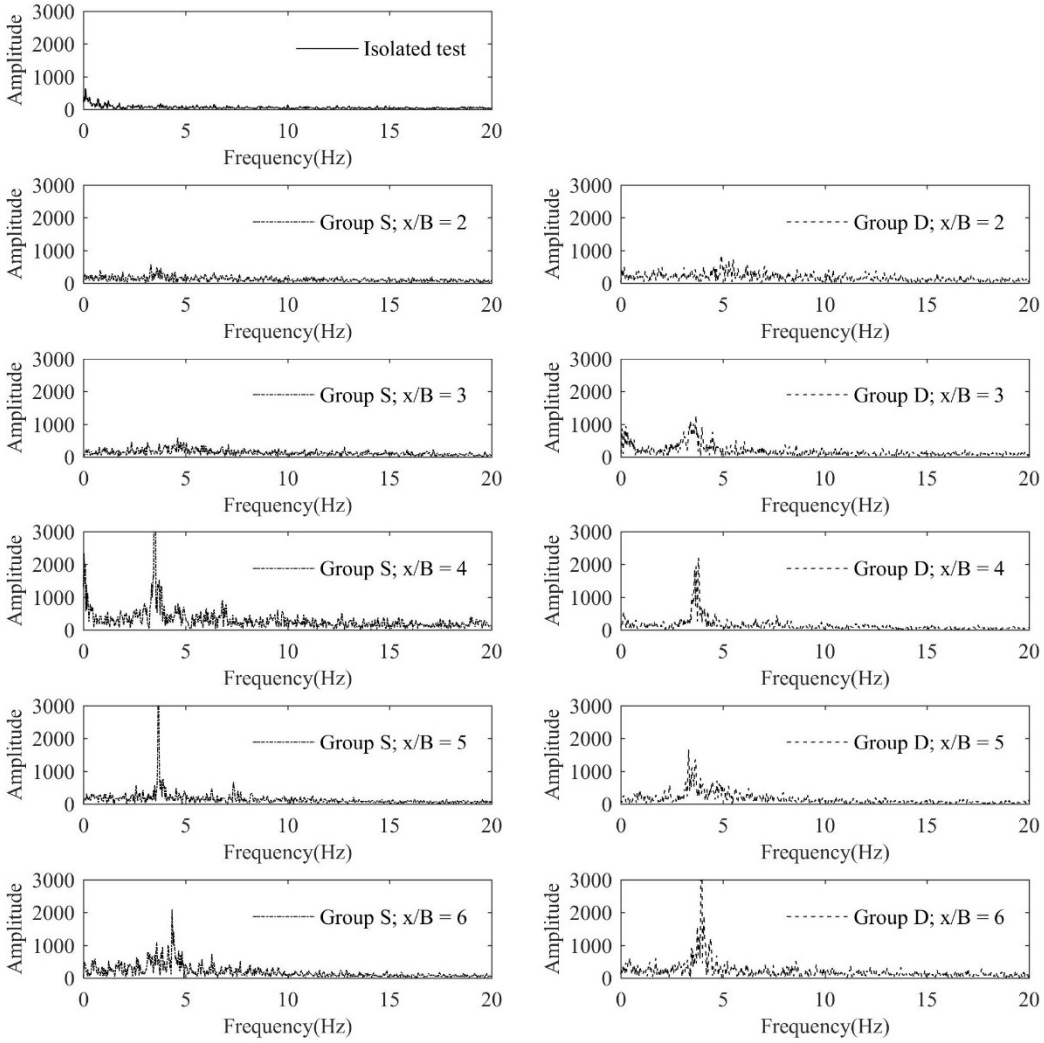

Figure 4-14: Fast Fourier Transform (FFT) of wake fluctuation on the side face of the principal model in tandem arrangements

The analysis of power spectrum on the side of the principal model (Figure 4-14) explains more clearly for VIV and Strouhal number $St = fB/U_0$ where f is the frequency of vortex shedding. In close distances, the peak amplitude is not clear enough to distinguish from other adjacent points according to the slight vibration in VIV for all cases. Whereas, from x/B = 3 in group S and group D, the peak is extremely sharped. The frequency at the peak in each case increases with the increase of the distance between two models in interference tests. The amplitude of group S in x/B = 4 and 5 is lower than group D, while the opposite phenomenon is observed in distance x/B = 6. The critical position for interference model may be located in between x/B = 5 and x/B = 6. Moreover, Strouhal numbers are calculated from these peaks of power spectrum graphs. This number is directly proportional to the frequency of the vortex shedding. The distance between the two models in interference tests is farther, the higher Strouhal number is obtained. These results are in agreement with those from Sakamoto, Hainu et al. (1987).

4.4.5 PIV images

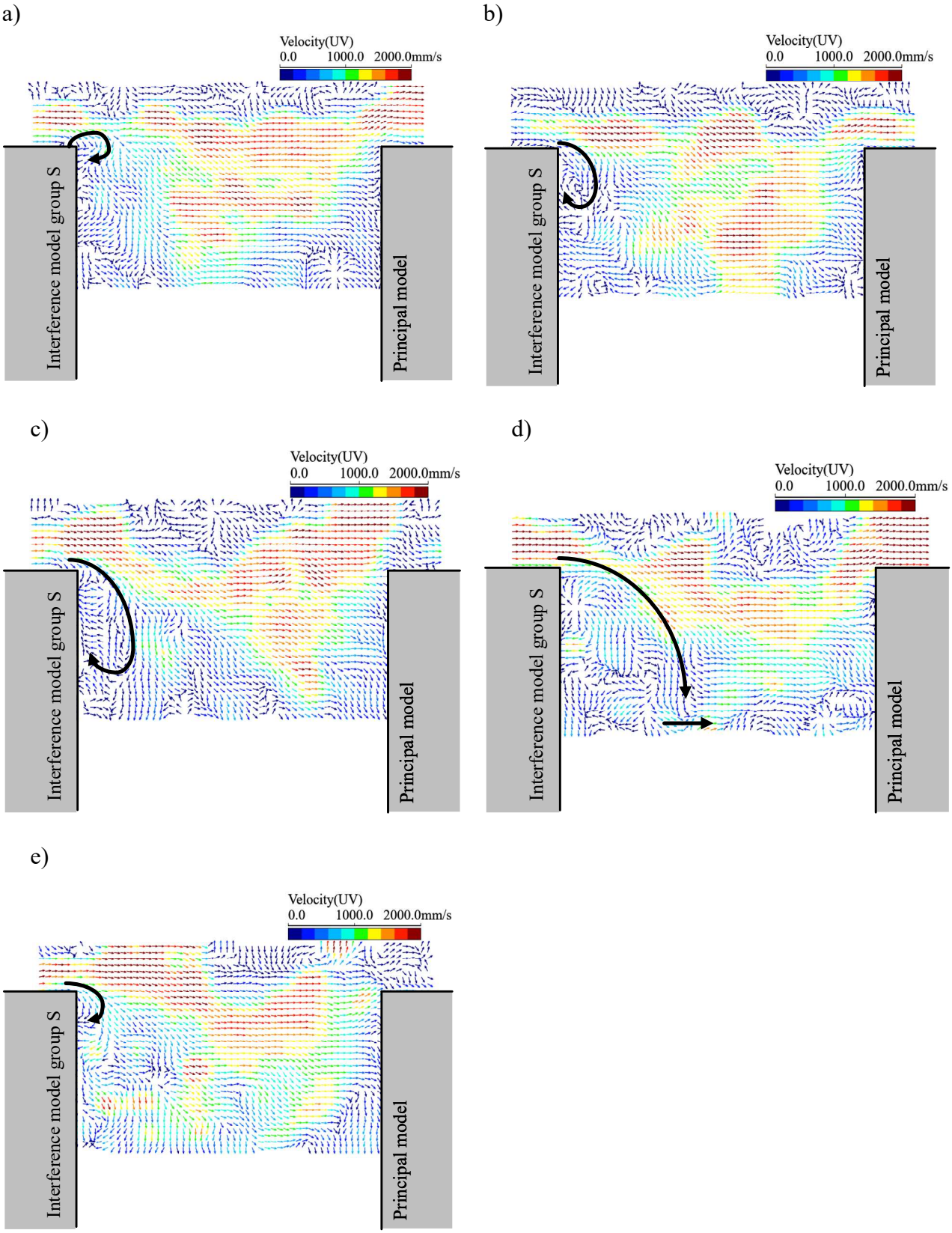

Figure 4-15: Instantaneous images of velocity field in group S, x/B = 5, y/B = 0: a) t = 0T; b) t = T/4; c) t = T/2; d) t = 3T/4; e) t = T;

An example of flow visualization in tandem arrangement group S at x/B = 5 is shown in Figure 4-15. Five instantaneous images are selected to represent the flow in one period of vortex shedding (T) which can be calculated from the frequency of vortex shedding in Figure 4-14 (Group S; x/B =5: f = 3.687 Hz). The vortex is always present under the shear layer of the WOT flow which is generated from the top of the upstream model and developed to downstream. Due to this vortex, the area on the leeward side of the interference model is in negative pressures. Figure 4-15a shows the vortex which is initially generated on the leading edge at top of the interference model. Then, the size of the vortex keeps increasing between the streamwise and downward direction (Figure 4-15b, c). These vortices are in different sizes in different times but always start from the edge of the flat roof. However, this kind of vortex is easy to lose its energy when moving down and mixes up with the side flow which is generated from the lower wall on the vertical edges of the upstream model (Figure 4-15d). In these figures, the shear layer of the WOT flow tend to move downward after leaving the roof of the interference model.

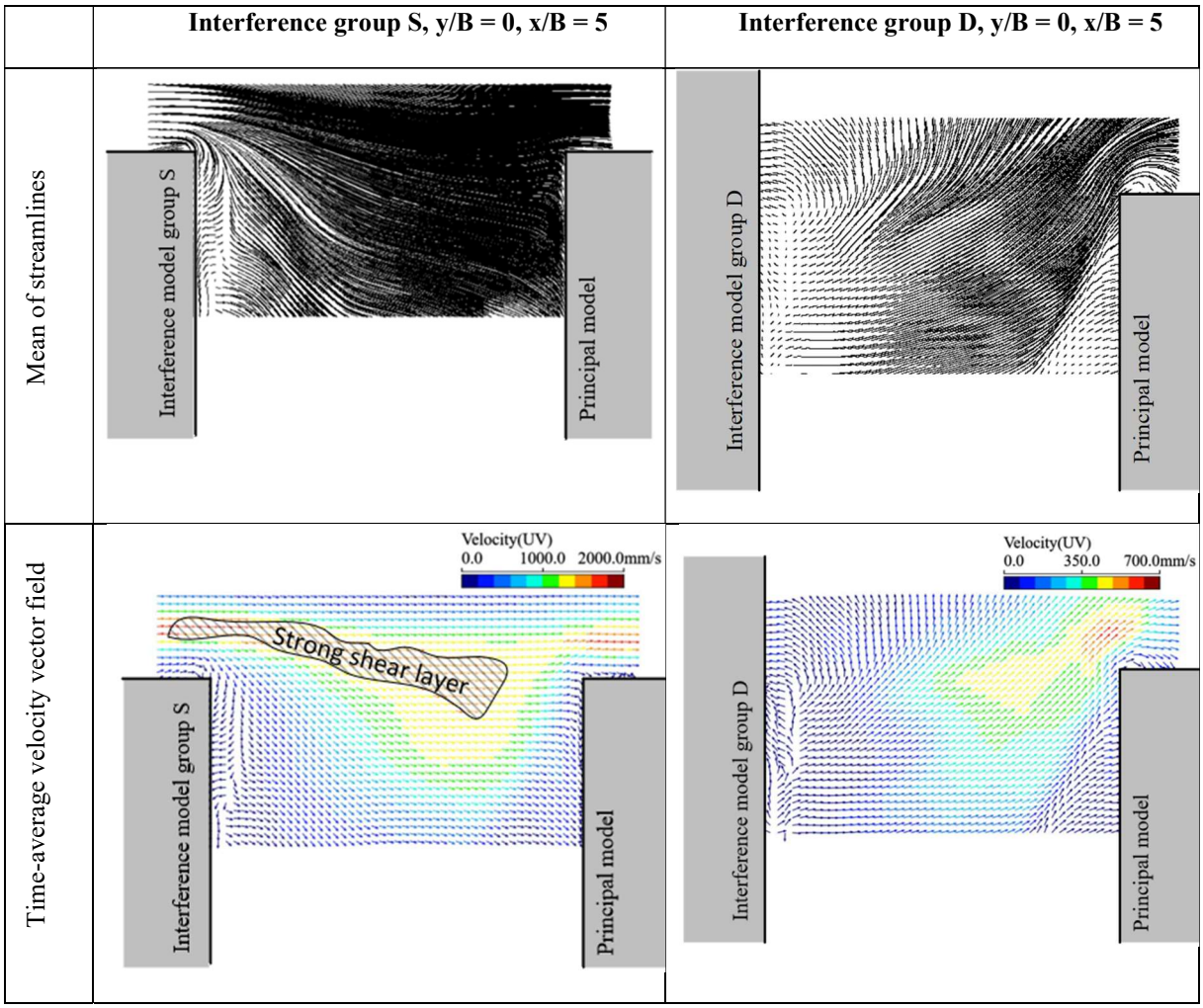

Figure 4-16: Mean streamlines and time-average velocity vector field at x/B = 5; y/B = 0

Figure 4-16 shows the mean of streamlines and time-average velocity vector fields of tandem arrangements at distance of x/B = 5. A part of models is also represented in this figure. These images are obtained by averaging all instantaneous images. The analysis of mean of streamlines and time-average velocity vector fields gives an overall image of WOT flow regardless of time.

In streamline results, the shear layer of WOT flow passes the roof, tends to go down and heads to the front side of the principal model. With this shear layer, the areas near the top of the principal model turn into positive pressure area and even receive more pressure than the isolated test. The same results are shown in Figure 4-10 when showing the high-pressure value on the pressure near the top of the principal model. On the other hand, group D without WOT flow does not form the shear layer behind the leeward wall of the interference model. The low pressures between two models and the presence of Karman vortex make all sides of the principal model turn to negative pressures at all positions.

In time-average velocity vector fields results, the shear layer of WOT flow generated on the flat roof of the interference model group S moves downward and downs to lower level of the principal model. The magnitude vector inside of shear layer of WOT flow slightly decreases along the wind flow direction. This means that the pressure could also reduce if the distance between two models increases. Thus, the most affected areas are the one near the top of the principal model, while the lower areas along the height of model suffer less effect.

4.4.6 Comparation to the current design code

ASCE 07-10 provides the method to calculate the wind load on the high-rise buildings as well as other structural components. For cladding design, there is no reported about the issue related to the overall structural of buildings. However, the damage from cladding, mostly by the damage of the glass, could harm to the pedestrian people. For some typical structure, the design of cladding would be referred from the design code.

For square cylinder with flat roof, ASCE section 6.5 gives the velocity pressure coefficients to design of cladding and structure. To compare with this study, the safety factor is considering by the ratio of the important factor ($I_w = 1.15$) and gust factor ($G = 0.85$). The external pressure coefficient of positive pressure is 0.6. And, external pressure coefficient of negative pressure is -0.7.

The interference test with the existence of the WOT flow is compared with the design limitation in ASCE in term of the pressure coefficient. Figure 4-17 indicates that all the results from the effect of the WOT flow is still located within the range of ASCE design. There are some cases that the pressure coefficients are overestimated with the ASCE design. However, it is underestimated of the safety factor design. At the distance $x/B = 6$, the area near the top of the principal model is in the danger area comparing to the design code. The requirement of strengthening the cladding design near the roof is needed.

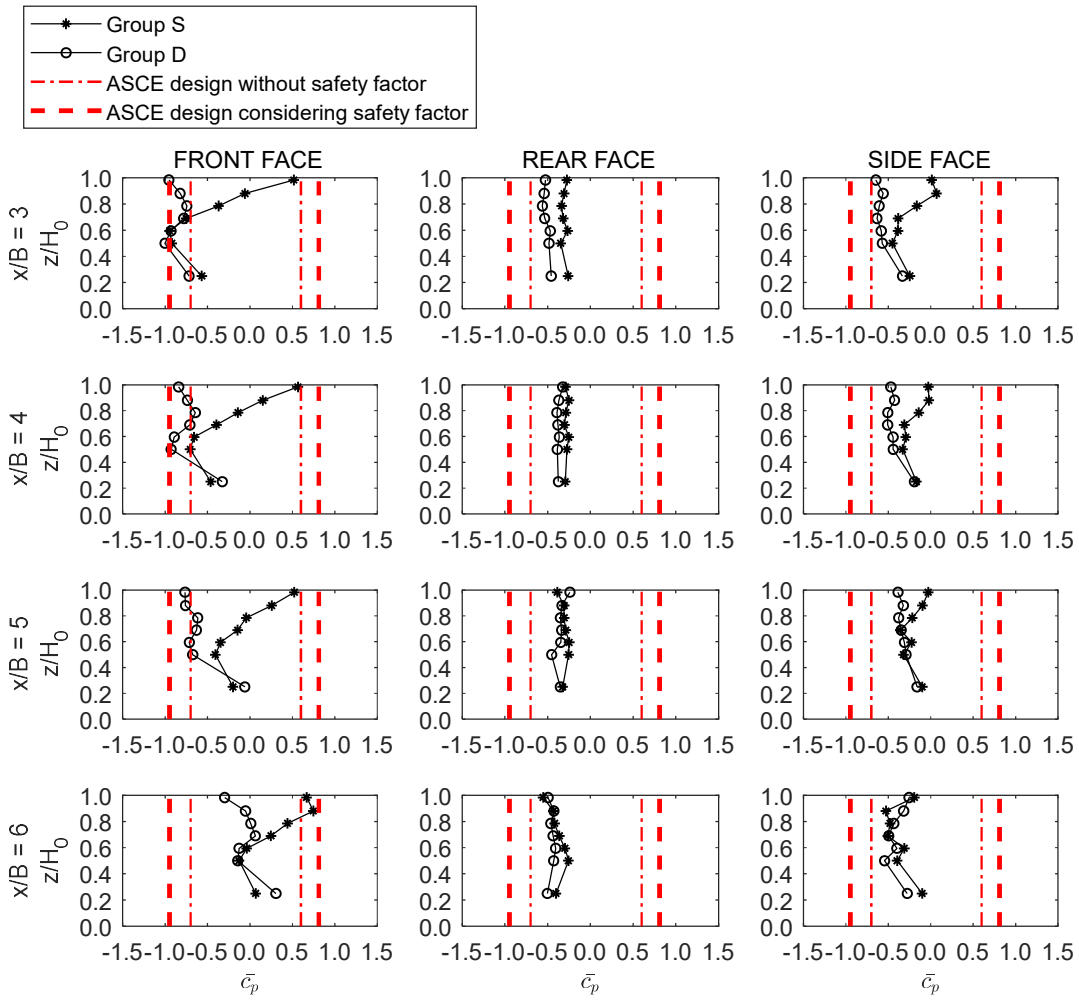

Figure 4-17: The comparison of this study to the limit design of ASCE

4.5 Summary

In this study, the WOT flow in square cylinder high-rise buildings are investigated and systematically studied through a series of static and dynamic wind tunnel tests. The contribution of WOT flow in different locations is analysed, and following conclusion can be inferred:

1) The WOT flow has strong effects in the same height models. At position x/B = 5, y/B =0 of the same height upstream model, the WOT flow could contribute 62.31% of pressure coefficient to the front face of the principal model. Even though there is a model in the upstream direction and it presents as the shielding model, a part of the front face of the principal model shows higher positive pressures compared to the isolated test. When the distance between the upstream model and the downstream model is lengthened, the affected area on the front face increases because of shear layer generated from WOT flow.

2) In dynamic vibration, the presence of the WOT flow in interference tests makes the principal model vibrate in small amplitude within the distance x/B = 2 to 4 in tandem arrangement. In farther distance (x/B = 5, 6), the contribution of the WOT flow in group S make VIV occur in a higher reduced velocity compared to both isolated tests and group D. Meanwhile, in all distances of tandem arrangement, the WOT flow provides the beneficial effects in terms of dynamic structural designs. Therefore, buildings on the

site can resist better by the contribution of the WOT flow.

Chapter 5

Simulation by Unsteady Reynolds-averaged Navier-Stocks Equation (URANS) Method

5.1 Verification cases on AIJ Benchmark test

A verification case was tested on the building model with the ration of 4:4:1 as recommendation of AIJ Benchmark test (Tominaga, Mochida et al. 2016). The domain was generated by the structured mesh using k-ε model in unsteady state. The results of simulation latter on are compare with the wind tunnel test (MENG and HIBI 1998).

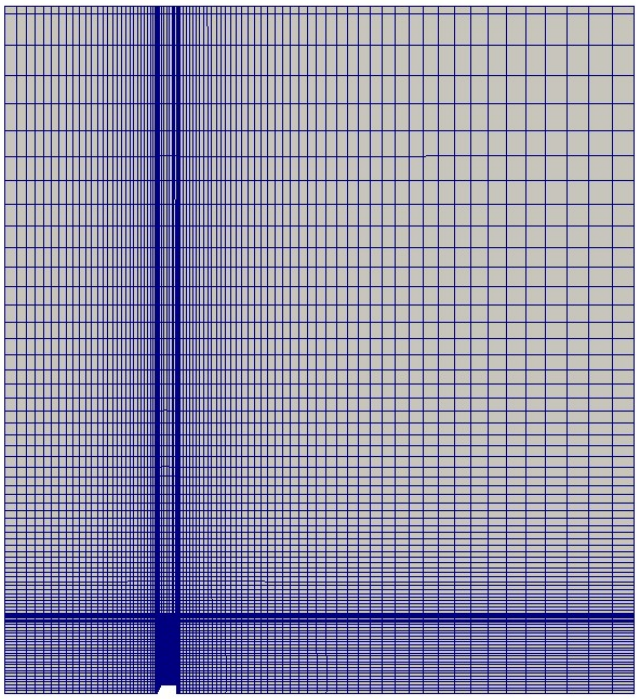

Figure 5-1: Structural mesh of verification case

The simulation is assumed that the flow is incompressible, there is no heat transfer, turbulence viscosity is isotropic (Ratio between Reynolds stress and mean rate of deformation is the same in all directions).

The input velocity is simulated by the power law with the modification from the turbulence intensity at the reference point. All standard k-ε and modified k-ε models simulate well for the inflow boundary condition (Figure 5-2). To compare with the results from wind tunnel tests, many points are selected in horizontal plan (Figure 5-3) and vertical plan (Figure 5-5) to measure the velocity at instantaneous time. The results of velocity field is well reproduced by

all turbulence model (Figure 5-6). However, only Durbin model and Renormalization group k-ε could reproduce well the value of kinetic energy around the model (Figure 5-7).

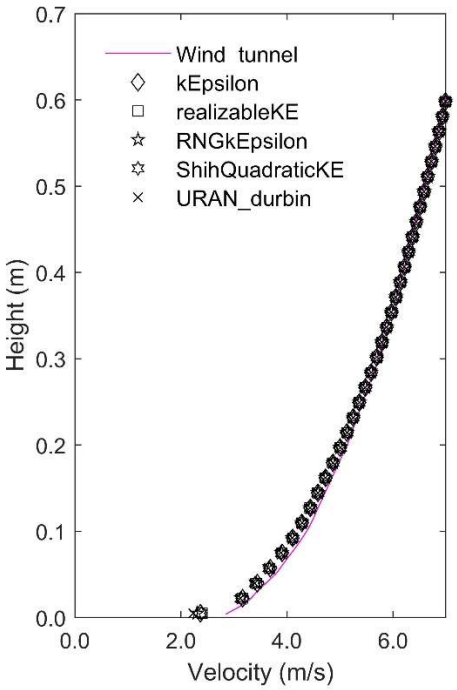

Figure 5-2: Comparison of inlet velocity in all turbulence model case

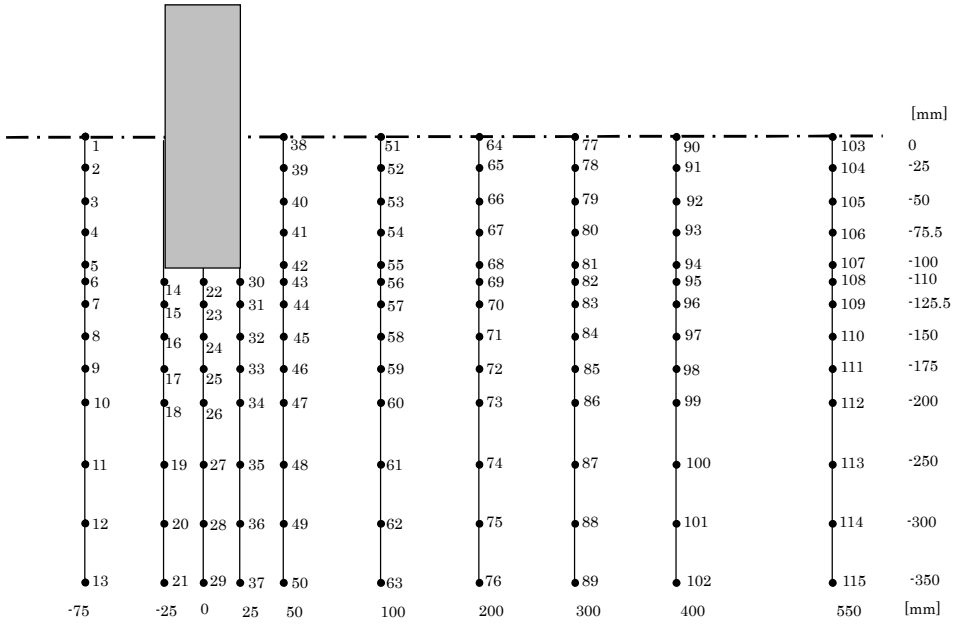

Figure 5-3: Measurement points in horizontal section (z = 0.0125m)

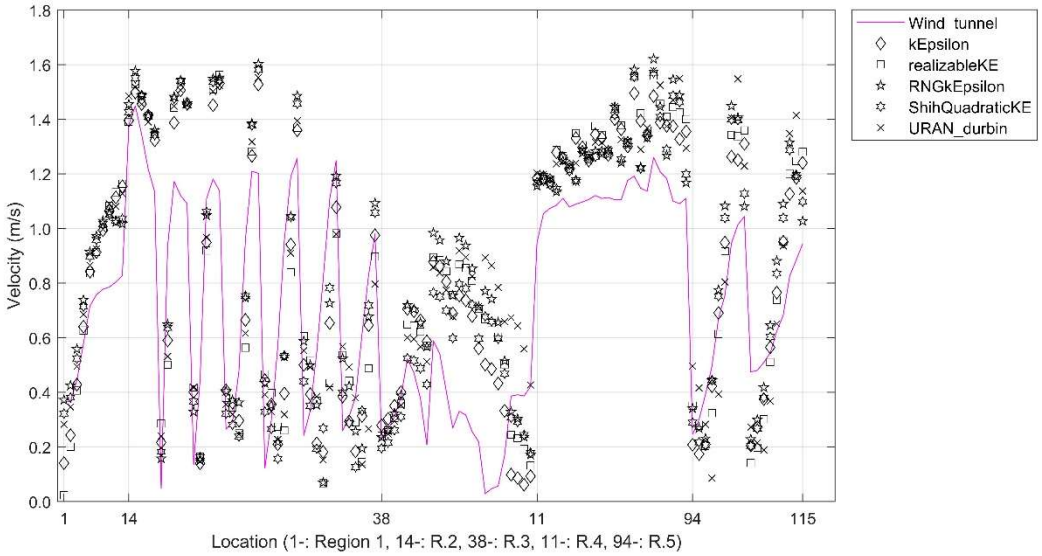

Figure 5-4: Comparison on horizontal velocity around the model

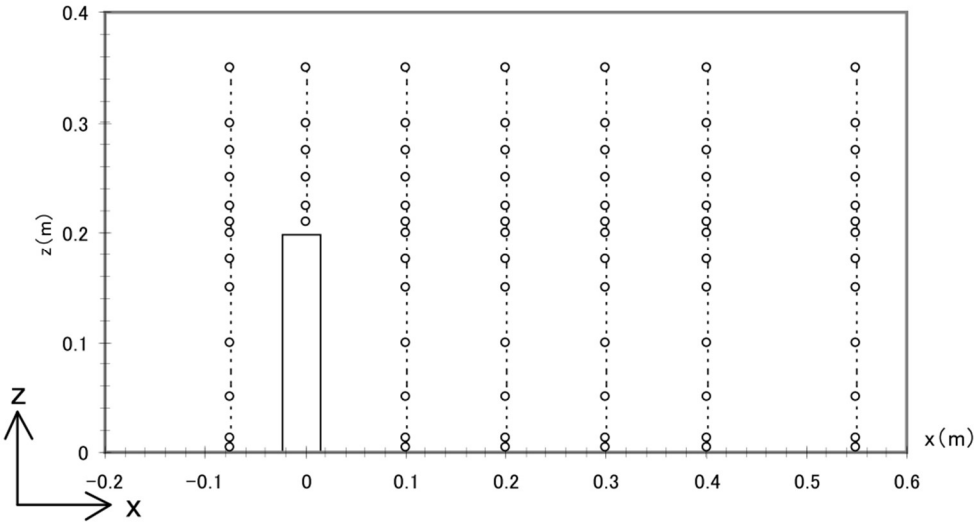

Figure 5-5:Measurement points in vertical section (y=0)

In these tests, all turbulence models in URANS is overestimated on the top of the model due to the reverse flow. The results of simulation are much depended on the way to reconstruct the eddy near the top of each turbulence models. The properties of velocity are well simulated, the mean pressure coefficient on the model could be used in this case. However, the instantaneous results is important to calculate the peak values which is using in the design as the extreme value.

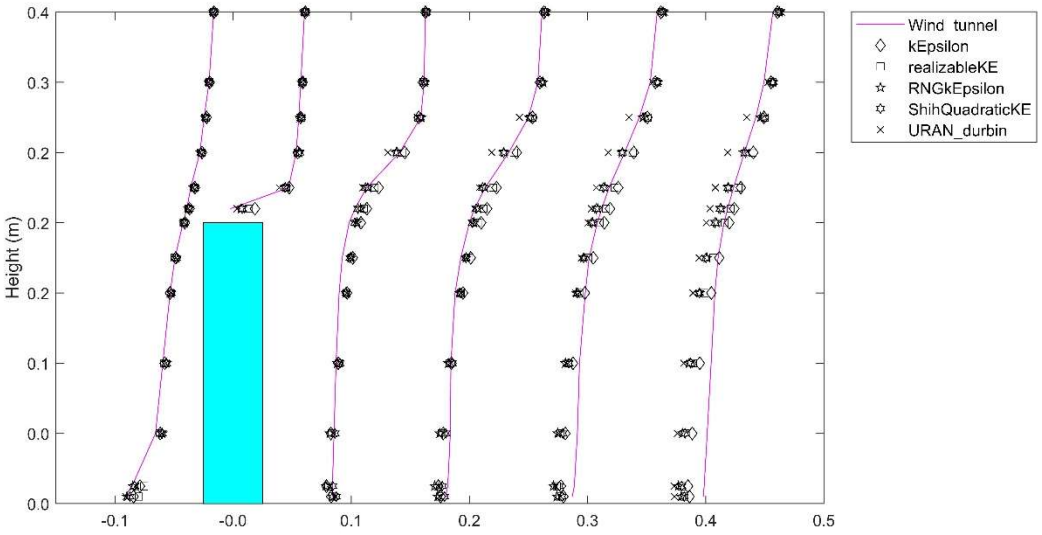

Figure 5-6: Comparison of vertical velocity at measurement points (x-axis = x position + 0.3*velocity)

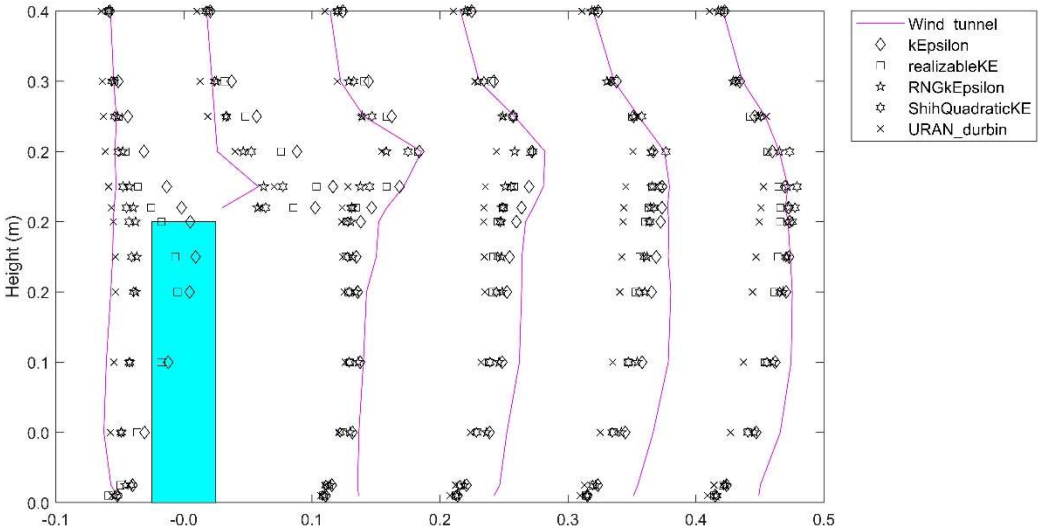

Figure 5-7: Comparison of kinetic energy at measurement points (x-axis = x position + 0.3*kinetic energy)

The results show that, Durbin model and Renormalization group k-ε are the best fixed to the wind tunnel test results among all the modified k-ε models.

5.2 Selection of inflow boundary condition, meshing

The comparison of a single model's test results was performed using structured grid and unstructured grid in the same domain's size. Figure 5-8 represents the domain and boundary conditions of both cases which are set to be the same configuration in a discretization method. The unstructured mesh with polyhedral mesh contains only 274,744 cells compared to a large number of mesh 2,058,244 cells in structural mesh to produce the same value of Y+. The polyhedral mesh could increase the size along three axes while the structured mesh needs to keep the small grid along the whole domain. The polyhedral mesh has proved the advantage in

reducing the number of mesh cells and disadvantage in increasing the number of faces (Spiegel, Redel et al. 2011). However, polyhedral mesh in this study shows the advantages in both the number of cells and faces due to the strategy of increasing sizes in all directions. Also, the accuracy of the polyhedral mesh is proved as same as the structured mesh in the researches of Japanese institutes (Tominaga, Mochida et al. 2016).

The results of mean pressure coefficient in the simulation are compared with the current wind tunnel test (Sy, Yamada et al. 2019) and previous studies on the isolated building in Figure 5-9. List of the wind tunnel test on the Commonwealth Advisory Aeronautical Research Council (CAARC) standard building (Dragoiescu, Garber et al. 2006) including tests from City University, Briton University, Monash University, Tongji University, and Cheng, Fu et al. (2010). The result indicates that the pressure coefficients in simulation on all faces agree well with the experimental tests in literatures. Moreover, the results of polyhedral mesh and structured mesh are giving the same pressure coefficients. A little different pressure can be observed in the figure. However, this difference is small enough to be ignored. Therefore, the polyhedral mesh would be constructed in coming simulation tests to reduce the execution time of each case.

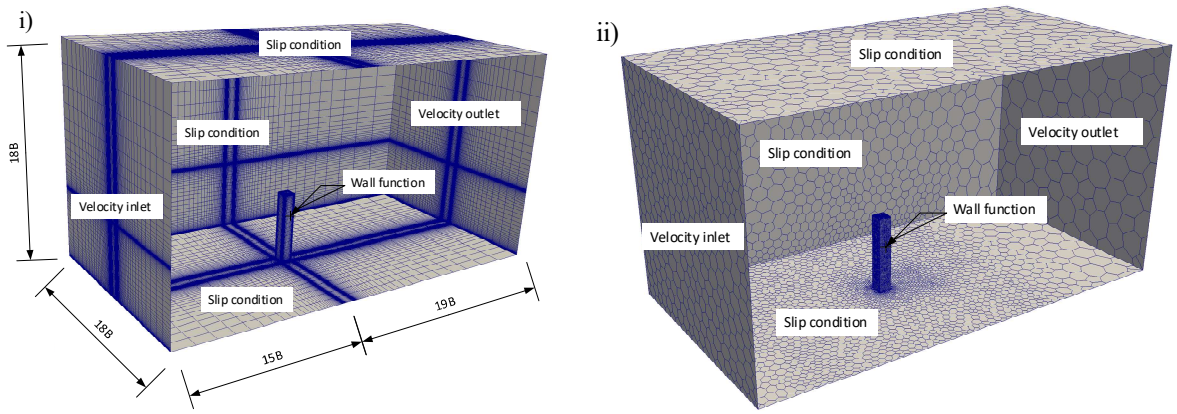

Figure 5-8: Boundary conditions: i) Structural mesh; ii) Polyhedral mesh.

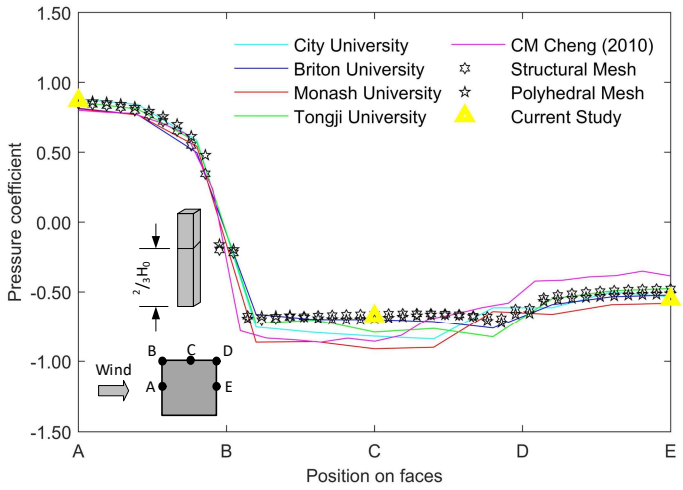

Figure 5-9. Compared results of different mesh types and previous studies of mean pressure coefficients at $^2/_3H_0$ of the principal model. A-B: Front face; B-D: Side face; D-E: Back face

5.3 Selection of turbulence model

To find out the best fixed turbulence model for the current study, all incompressible turbulence models in Table 5-1 are simulated in the isolated cases and compared with the literature and current study on wind tunnel test. The suggestion for URAN test in AIJ Benchmarks test (Tominaga, Mochida et al. 2016) was Renormalization group k-ε. While Wilcox (1998) suggests using k-Ω SST model to reproduce well the stagnation point. However, the current wind tunnel test was performed with different turbulence intensity and boundary condition compared to the Benchmark test and literatures. Thus, the trial tests on different turbulence models of URANS is needed to find out the most accurate model for the current wind flow condition.

Table 5-1: Applied turbulence model **in RANS simulation test**

Turbulence model	Note	Reference
Standard k-ε	kEpsilon	(Launder and Spalding 1983)
Lien cubic non-linear low-Reynolds k-ε	LienCubicKE	(Lien, Chen et al. 1996)
Realizable k-ε turbulence model	realizableKE	(Shih, Liou et al. 1995)
Renormalization group k-ε	RNGkEpsilon	(Yakhot, Orszag et al. 1992)
Shih's quadratic algebraic Reynolds stress k-ε	ShihQuadraticKE	(Shih, Zhu et al. 1993)
Lien and Kalitzin's v2-f	v2f	(Lien and Kalitzin 2001, Davidson 2003)
Standard high Reynolds-number k-Ω	kOmega	(Wilcox 1998)
Implementation of the k-Ω SST	kOmegaSST	(Hellsten 1998, Menter and Esch 2001)

The means of pressure coefficients of all faces in the elevation of $^2/_3H_0$ are represented in Figure 5-10 including simulation tests, wind tunnel test, and literatures. Wind tunnel test shows a strong correlation to literature. In general, all turbulent models can simulate the trend of pressure in the building model. Group of k-ε based models show the various results along the measured line. Standard k-ε, RNGkEpsilon, realizableKE and v2f models could not produce the appropriate results when showing high pressure in the front face and low pressure in the side and back faces. LienCubicKE and ShihQuadraticKE model simulate the turbulence model in the test and with acceptable results on the local pressure. The two equation models on k-ε model is not a good guesser in this low turbulence intensity case, while the nonlinear eddy viscosity models could present the results better. In the other hand, kOmega and kOmegaSST indicate different accuracy level of pressure on faces. The kOmega and v2f model are difficult to avoid the stagnation point abnormally. The turbulence model kOmega could not present the accuracy pressure on the model while the kOmegaSST well presents the results on faces matching with literature and current study by wind tunnel test.

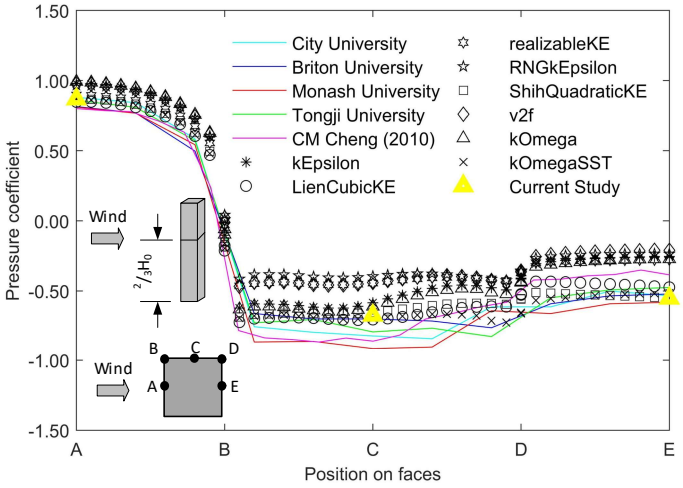

Figure 5-10. Compared results from different turbulence model tests and previous studies of mean pressure coefficients at $^2/_3H_0$ of the principal model.

5.4 Mean pressure on the principal model in interference test.

Figure 5-11i) and Figure 5-12 show the mean pressure coefficient of pressure taps along with the height of the front, side and rear faces of the principal model in tandem arrangements respectively. The data sets in the front face present the trend of WOT flow clearly. In interference tests, most of the pressure coefficients in the front face of the principal models show negative value compared to positive pressures on the front face of the isolated test. These positive pressures on the front face and negative pressures on the rear face makes the drag coefficient of the whole model turn to a positive value. When the interference models located near the principal model at x/B less than 2, no significant difference between two different interference cases is found. The WOT flow has no effect on the principal model in these cases. From x/B = 3 to 6, the pressure coefficients on the front face of the principal model in same height interference tests change gradually in each distance. The areas near the top firstly turn to positive pressures at distance x/B = 3. In this case, the shear layer from the WOT flow could move downward and reach the front face of the downstream model. When the same height interference models move away from the principal model, the area of positive pressure on the principal model increased with the increase of the distance. From x/B = 7, the top pressure of the front face of the principal building change the trend when backing to the negative value. This phenomenon clearly presents the vortex from the roof top of the interference model.

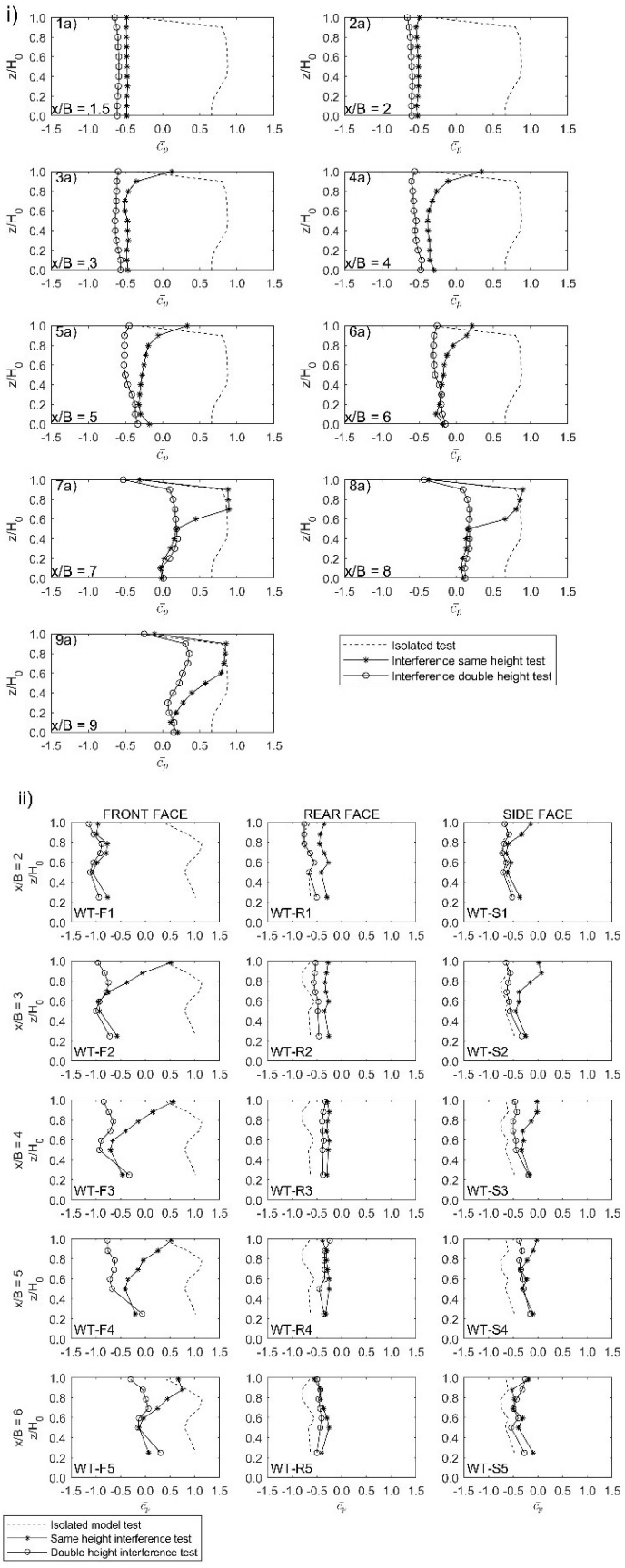

Figure 5-11: i) Pressure coefficients on the front face of the principal model in tandem arrangements of two types of interference model (1a – 9a). ii) Wind tunnel results of pressure coefficients on all faces of the principal model in different tandem arrangements of two types of interference model (WT series).

For comparison, results of wind tunnel tests are also represented in Figure 5-11ii). In general, the simulation results show the correct trend along with the wind tunnel results. Instead of discrete results due to the limitation of the number of pressures taps on the principal model in wind tunnel tests, results of simulation can show the continuous value along the principal model's face. The area of positive pressure coefficients increases as the increase of the distance between the two models. The pressure along the height of the model proved that the WOT flow shows the existence of 3D arch type vortex in the vertical direction. Moreover, there is different pressure at the top of the principal model in isolated test between the results of simulation and wind tunnel test. While the wind tunnel test indicates the low positive value of pressure coefficient near the top, the simulation test shows the low amplitude of negative pressure on the top of the model. This different result is explained by the installation of a pressure tap when we could not place pressure tap at the real top of the principal model.

At the side face, the pressures along the building height in both cases of interference tests do not show the variation in the closed distance x/B<6 (Figure 5-12i). In this range, the wind from the rooftop could not fully develop to contribute effects to the side face. However, in further distance, x/B>6, the WOT in interference same height presents clearly when showing the difference with the double high interference test. The rooftop wind combined with the Karman vortex generated from the side face of the interference model becomes the 3D arch type vortex. This arch type vortex needs a long distance enough to contribute to local pressure on the side face of the principal model. In the other hand, there is not much different pressure coefficients at the back side of the principal model but the pressure near the top area. The slight difference can be observed in far distance x/B>6 between two models. The phenomenon can be easily proved by the wind tunnel test in a closed gap of models. However, there is a significant change from top to middle of model in the range of x/B = 7-9. Especially, the high negative pressure is observed in the middle of the principal model, showing the dangerous area for façade design.

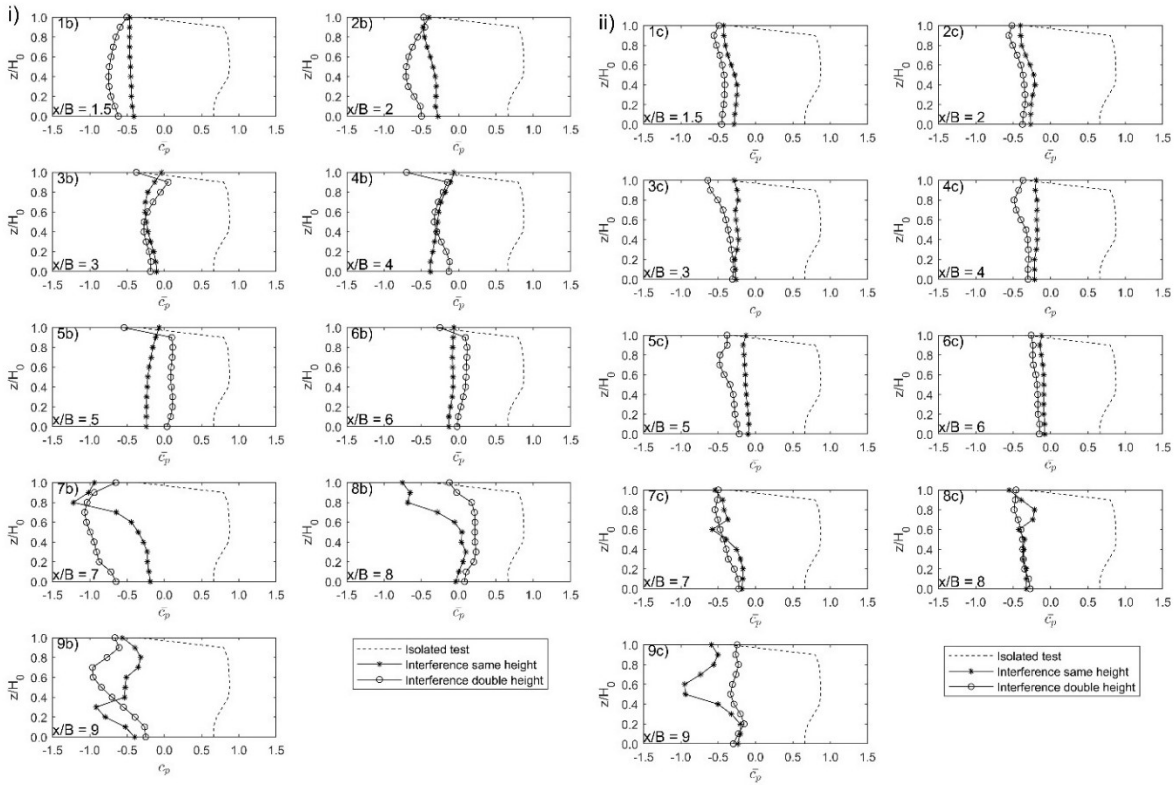

Figure 5-12: Pressure coefficients on the principal model i) The side face (graph 1b-9b); ii) The rear face (graph 1c-9c) of the principal model in tandem arrangements of two types of interference model.

5.5 Response spectra of downstream model

The analysis of response spectra on the side of the principal model is represented in Figure 5-13i). In general, the peak of double height interference height tests is clearly and sharply than the same height interference tests. The response spectra's amplitude in most of the cases of same height interference tests is lower than double height interference tests. The continuous contribution of pure Karman vortex probably produces the peak of power spectrum density sharper in tests with double height interference model. In the distance of x/B = 3, the frequency at the peak increases with the increase of the distance between two models in interference tests. The critical position for interference model may be located in between x/B = 5 and x/B = 6 where the peaks of the response spectra show clearly in both cases of test.

Moreover, Strouhal numbers are calculated from these peaks of response spectra graphs and represented in Figure 5-13ii). This number is directly proportional to the frequency of the vortex shedding. The Strouhal number is constant at 0.2 for both cases of interference tests. In close distance of the arrangement of two model, x/B = 3-4, the WOT flow significantly decreases the Strouhal number resulting in the low frequency of the oscillation. These results are in complete agreement with Sakamoto, Hainu et al. (1987).

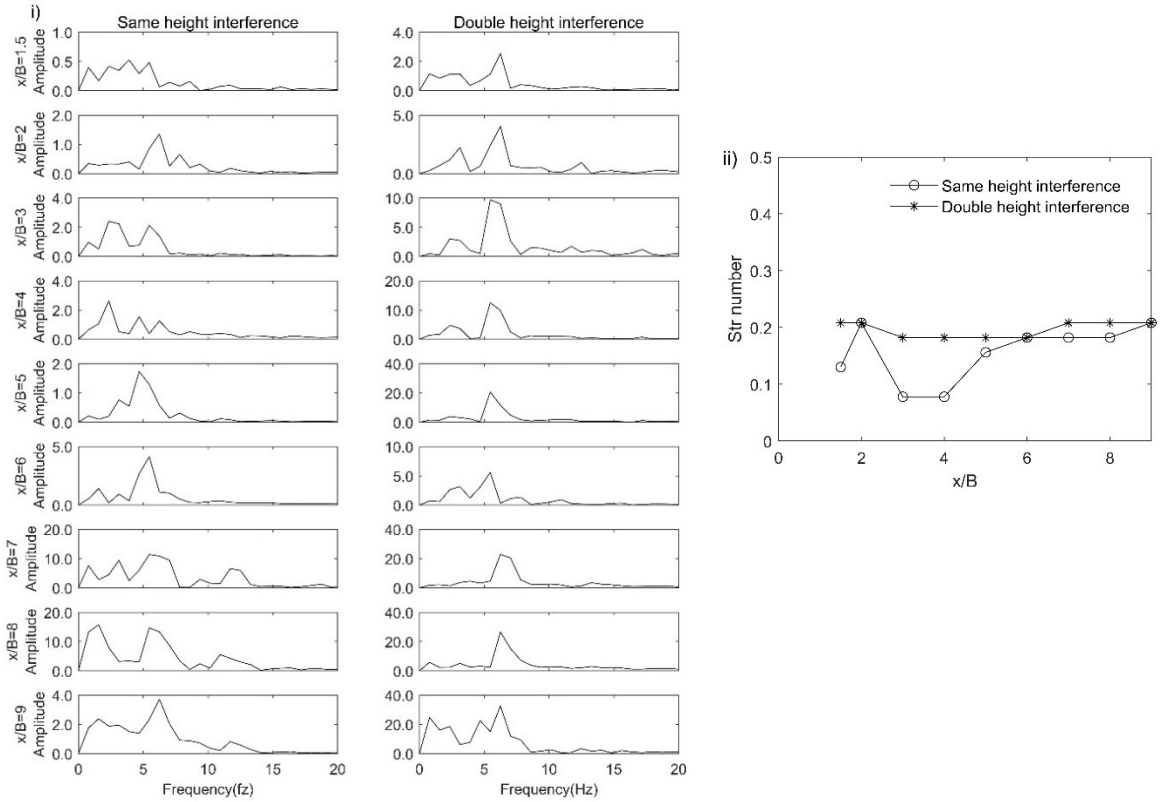

Figure 5-13: i) Power spectrum density of the principal model when measuring the pressure on the point on the side face. ii) Comparison of Strouhal number of two interference tests according to the distance between two model x/B.

5.6 Velocity vector field by the simulation

Figure 5-14 shows the average vector filed of interference tests at distance x/B = 5 in both same height and double height interference tests. The WOT flow generates the vortex on the top of interference model. This vortex keeps increasing the size and effect significantly on the principal model of the front face. The URANS models perform equally well in predicting the time-averaged flow but could not give the information of an instantaneous flow. In the other hand, the tall interference model did not show the increasing of the vortex. And, the front face of the principal model is always in negative pressure along with the height of the building.

i)

ii)

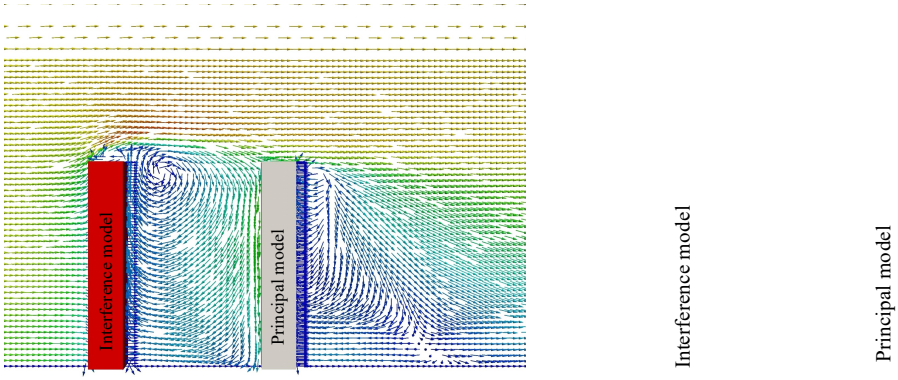

Figure 5-14: An example of vector fields in interference tests with x/B = 5. i) Same height interference test; ii) Double height interference test

5.7 Condition to form the WOT flow

Flow over the top of isolated building was initially form as the vortex which tip at the edge top (Figure 5-15i). Then, this vortex is modified by Karman vortex which is generated from the side face of building. At convergence stage, the Karman vortex in form of leg vortex (Figure 5-15ii) is observed in research of Williamson and Govardhan (2004)

i)

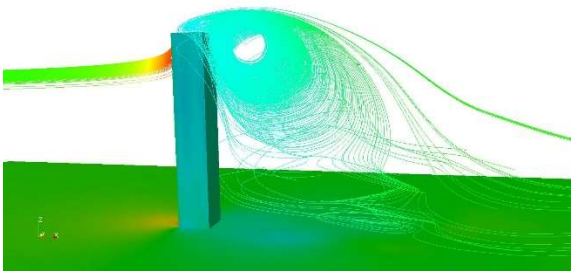

ii)

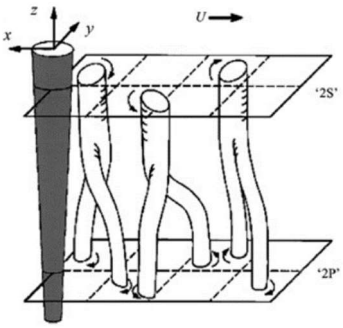

Figure 5-15: Different stage of rooftop wind over a single building: i) Initial stage; ii) Convergence stage (Williamson and Govardhan 2004)

In tandem arrangement with distance x/B≤6, the downstream model play a block role (Figure 5-16). The initial vortex could not develop to the convergence stage with the Karman vortex. This vortex keeps growing up the size, release energy and return to the smallest size. The tip of vortex is always stay at the edge top of upstream building. When the distance of two square cylinders increase x/B>6, the large area in between two models allow the vortex to transform to the Karman vortex in shape of leg form (Figure 5-17).

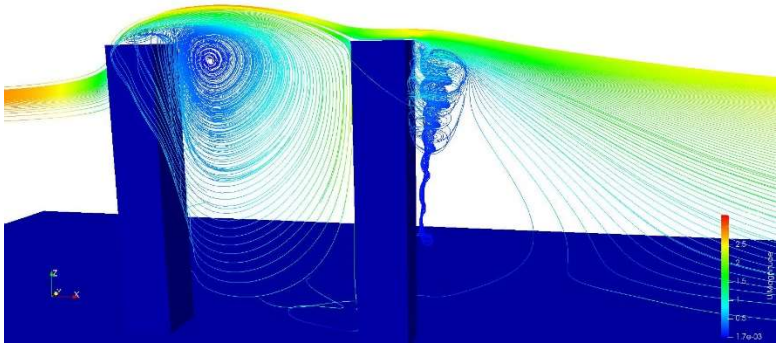

Figure 5-16: The flow field in same height interference x/B = 5

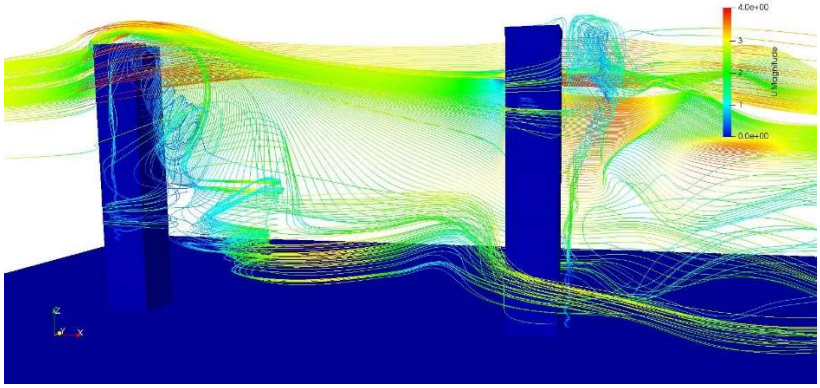

Figure 5-17: The flow field in same height interference test x/B = 9

5.8 Flow patterns

In interference test, the flow patterns are important to understand the properties of flow around a body. As we already realized that the WOT flow only exist with the distance of two building 3≤x/B≤6. For this reason, the flow pattern of two cases, x/B = 5 and x/B = 9 are plotted in same height interference and double height interference from level z = 0.3 to 0.6m (Figure 5-18, Figure 5-19, Figure 5-20, Figure 5-21).

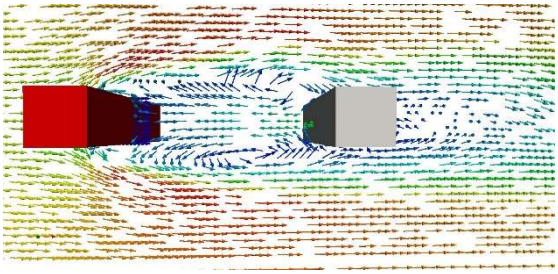

Same height interference test x/B = 5

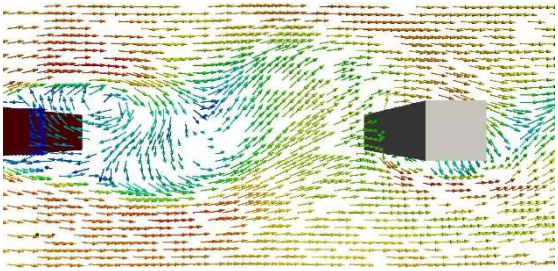

Same height interference test x/B = 9

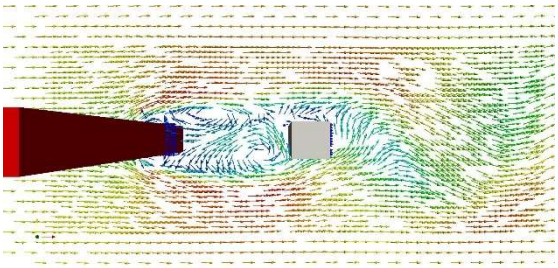

Double height interference test x/B = 5

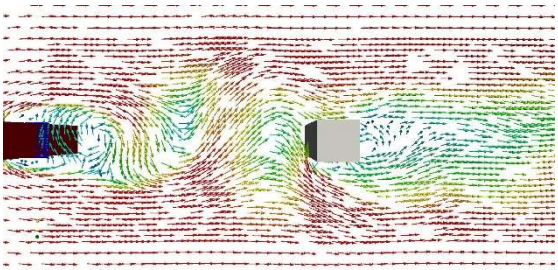

Double height interference test x/B = 9

Figure 5-18: Flow patterns between two models at level z = 0.3m

The same height interference test at the position x/B = 5 including the effects of the WOT flow has the different flow patterns compared to other cases. Without the existence of the WOT flow, an important point to mention is the cross flow generated from a side of upstream building to another side of downstream building. This is interesting point when the phenomenon is not happened in the case with the existence of the WOT flow. Only the reverse flow located on the axis along two buildings is appeared. The ellipse vortex is generated outside this reverse flow.

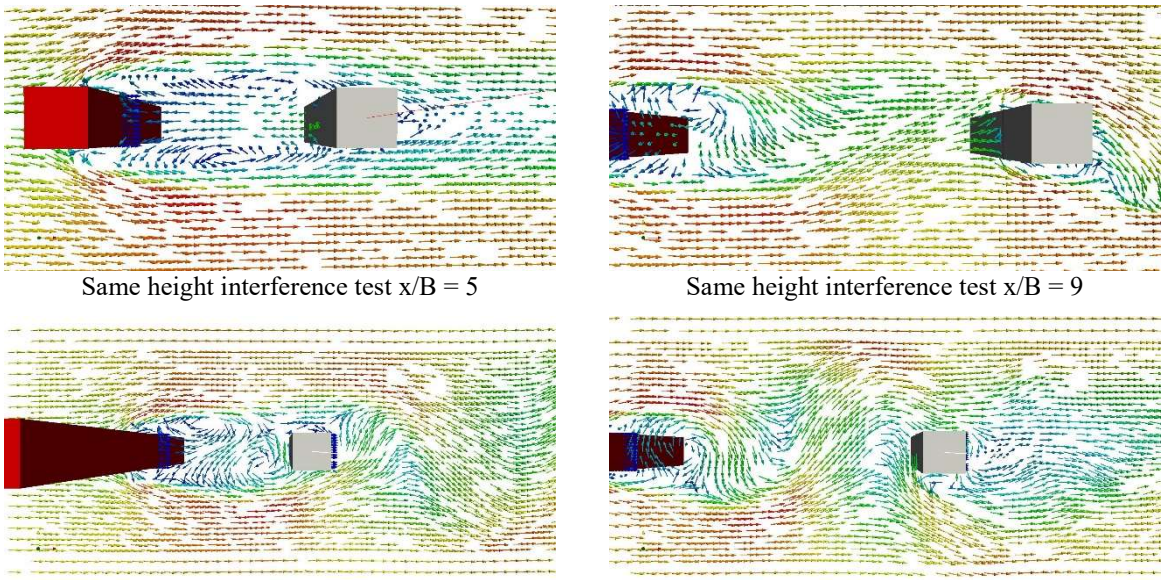

Same height interference test x/B = 5 | Same height interference test x/B = 9

Double height interference test x/B = 5 | Double height interference test x/B = 9

Figure 5-19: Flow patterns between two models at level z = 0.4m

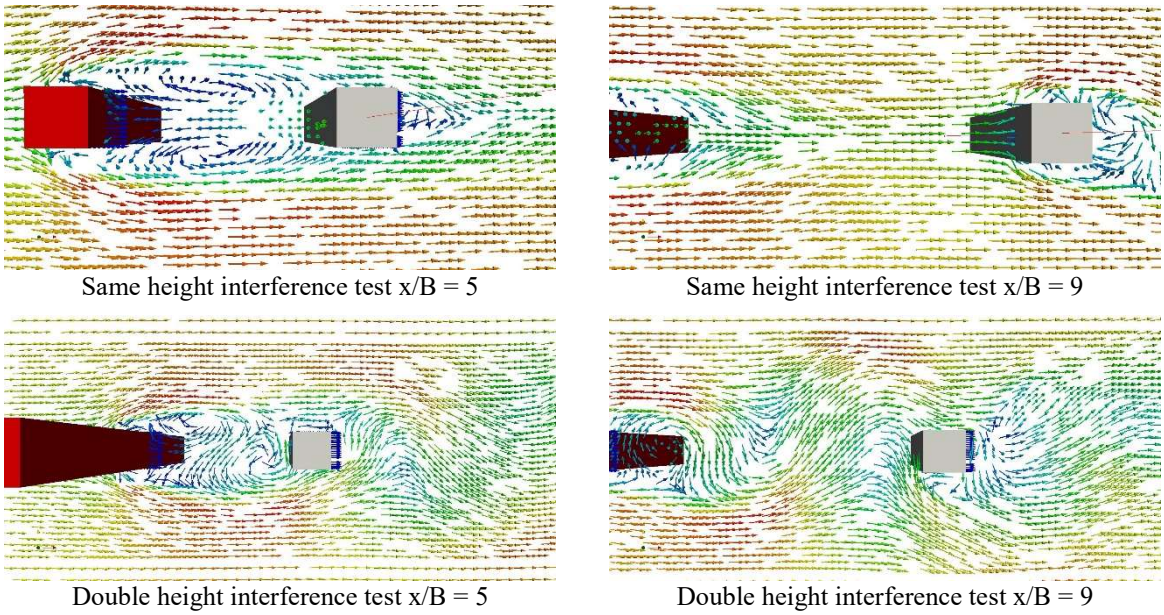

Same height interference test x/B = 5 | Same height interference test x/B = 9

Double height interference test x/B = 5 | Double height interference test x/B = 9

Figure 5-20: Flow patterns between two models at level z = 0.5m

In closed distance, the flow between two models is backward, rear face of upstream model and front face of downstream model is resisted with positive pressure and negative pressure respectively. On the other hand, the forward flow pattern is observed in far distance in the

example at x/B = 9. In this case, the front face of downstream building is with positive pressure just like as the isolated case.

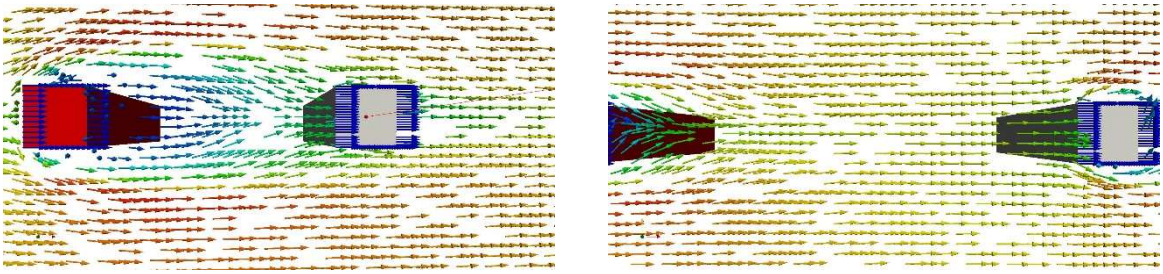

Same height interference test x/B = 5 Same height interference test x/B = 9

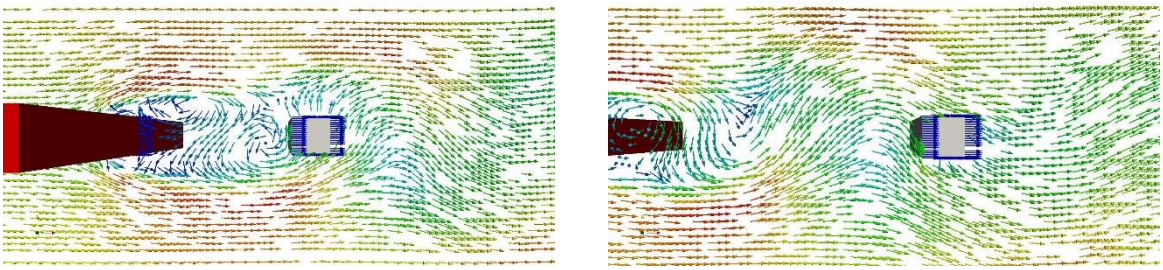

Double height interference test x/B = 5 Double height interference test x/B = 9

Figure 5-21: Flow patterns between two models at level z = 0.6m

5.9 Summary

In this chapter, the WOT flow generated from square cylinder high-rise buildings is investigated and systematically study through wind tunnel tests and CFD simulation. WOT flow exits in the form of 3D arch type vortex. This vortex effects on the downstream buildings by increasing the pressure of front face and side faces near the top area. The affected area from WOT flow increase when the distance between two buildings increases.

In the simulation, the polyhedral mesh reduces the computational effort by reducing the number of mesh while ensuring accuracy. The URANS model with kOmegaSST turbulence model could provide the correct trend of pressures and the power spectrum density on the downstream building. However, the URANS model could not provide the information of the instantaneous flow.

The condition to form the WOT flow is controlled by the distance of two building $3 \leq x/B \leq 6$. In these distances, the flow over the roof top will be blocked by the downstream building to fully develop to the leg Karman vortex.

The flow pattern of the WOT flow is also different from other cases. This pattern shows the reverse flow in the area between two models. Other cases present the cross flow from a side of upstream model to another side of downstream model.

Chapter 6

Simulation by Large Eddy Simulation (LES) Method

6.1 Turbulence generator

The inflow turbulence is the most important to simulate among computational wind engineering. Along with time, there are many methods which have been developed. Satisfying a target of spectrum such as the von Karman model is a significant job for the evaluation of wind effects. Consistent discrete random inflow generator was developed by Aboshosha, Elshaer et al. (2015). This method to correct the coherency in the inflow condition from the method discrete random inflow generator (Huang, Li et al. 2010).

Python code is constructed to generator the velocity in each time step in OpenFOAM by CDRFG method. The simulation results are compared with the wind tunnel test results. Figure 6-1 and Figure 6-2 show the good agreement of these generating data. Turbulence intensity is matched with the wind tunnel test. There is a little different turbulence intensity of two method near the ground where showing the near boundary condition. Power spectra density in simulation completely fixed with the wind tunnel test. Those data in low frequency is not following the Von Karman function and more concentrated in high frequency area.

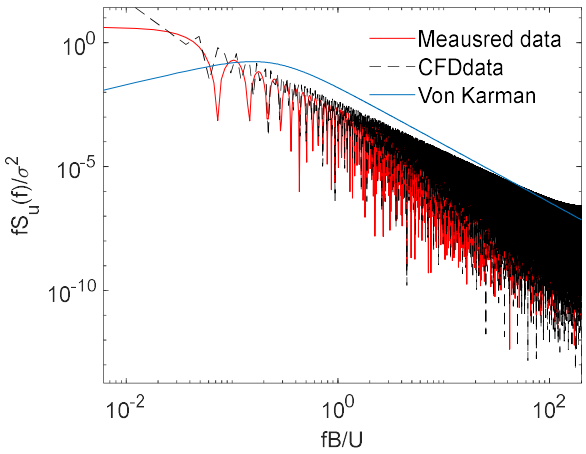

Figure 6-1: Power spectra density of measurement data and CFD data

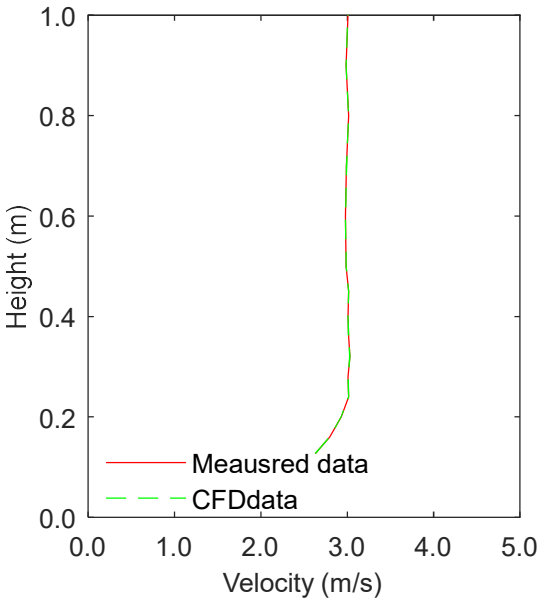

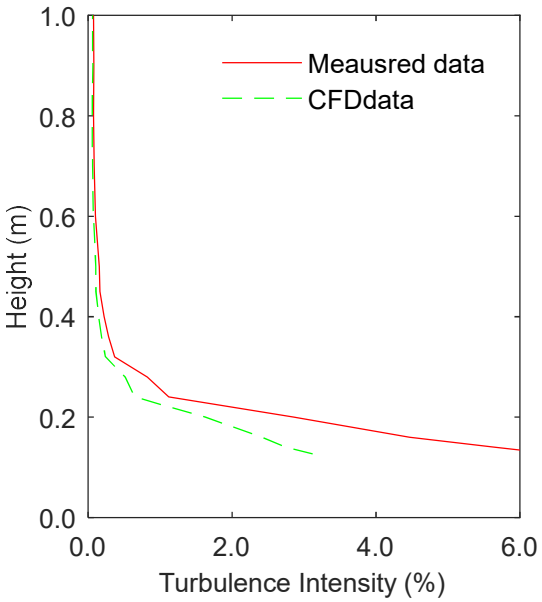

Figure 6-2: Comparison of measurement data and CFD data using CDRFG

CDRFG was applied in the isolated test. In this test, the pressure on all faces at 2/3 height of model were used to validate the results. The wind tunnel test conducted by Cheng, Fu et al. (2010) on the single building with aspect ratio 3 and side ratio 1.230 was plotted in Figure 6-3 for validation. Also, the results which was conducted on the standard CAARC building (Melbourne 1980) are also plotted for comparison. Noted that these tests were conducted with single building in turbulence flow and different aspect ratio and side ratio. However, with the mean value for comparison, these data are valuable for validation.

Figure 6-3 represents the mean pressure coefficient on all faces in the isolated test with cases using CDRFG method. With turbulence inflow generator, pressures by CDRFG show better accuracy. Without CDRFG, the inflow boundary condition in LES could not represent any

value of turbulence intensity. In the front face, the same results from two cases is observed. This may be explained by taking the average value in post process of LES simulation.

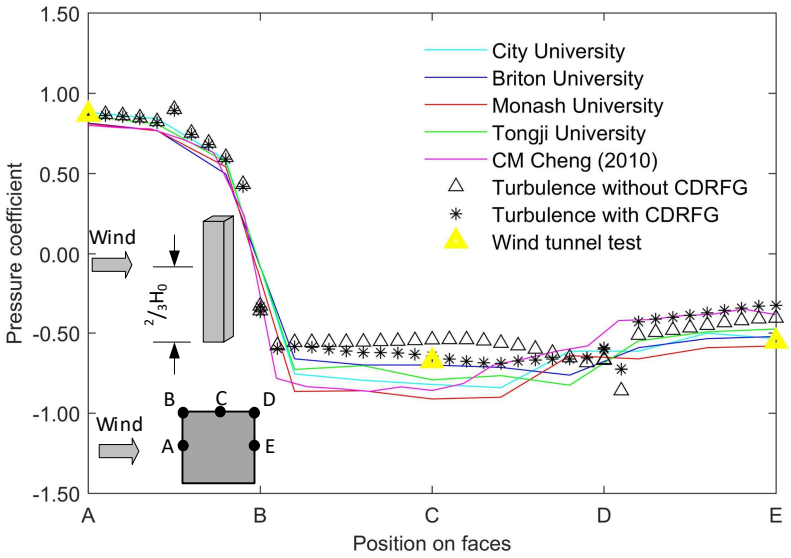

Figure 6-3: Comparison of mean pressure coefficient in the isolated test: Simulation with turbulence generator CDRFG, simulation with CDRFG

6.2 Optimization of computational efforts

Simulation in LES is time-costly due to the huge number of mesh cells. The y+ near wall at building is set with 0.6 with is small enough for sub-grid scale eddy. Even though the polyhedral mesh is used to reduce the number of cells, the number of cells is 2,157,202 cells considering for expensive simulation. In order to reduce the number of mesh, symmetry plane was used at y-axis (y=0) (Figure 6-4).

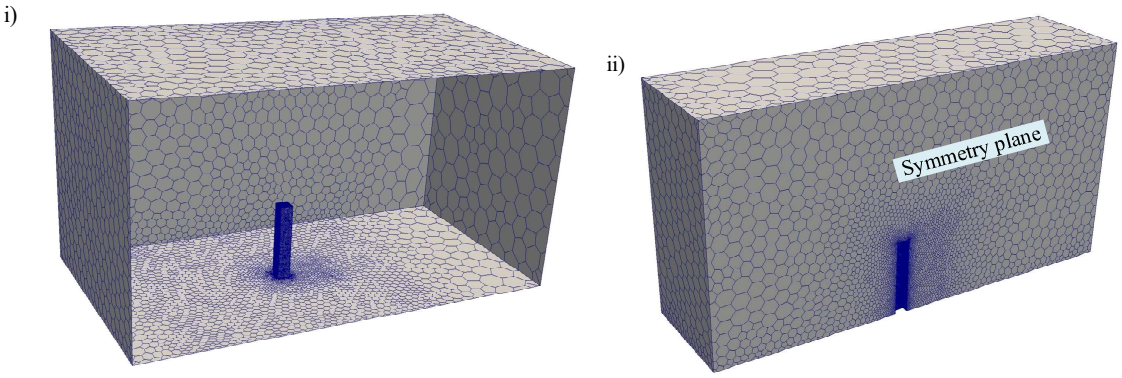

Figure 6-4: The domain constructed by polyhedral mesh: i) Full domain; ii) Half domain using symmetry plane.

The results of pressure coefficient in Figure 6-5 prove that half domain could not reproduced well the mean pressure on the front face as well as the edge between side and rear face. The geometry is symmetry while the flow is isotropic which means that the flow freely develops in three dimensions.

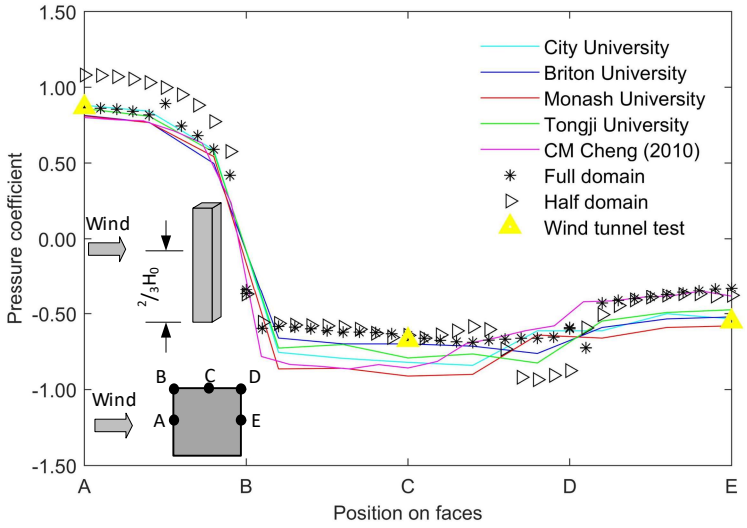

Figure 6-5: Comparison of mean pressure coefficient in the isolated test: Full domain and half domain

6.3 Time schemes

The part of convection-diffusion-source equation is the time schemes $\frac{\partial}{\partial t}(\rho\Phi)$. As the diffusion term will contain the unsteady vortex under the shear layer of the WOT flow. However, we are concerning on the mean of pressure coefficient in one cycle of flow. The steady method could be considered to simulate in this case. The results from Figure 6-6 show that there is good correlation in mean of pressure coefficient on the front face. However, the side face in unsteady state case reproduce over estimated pressure.

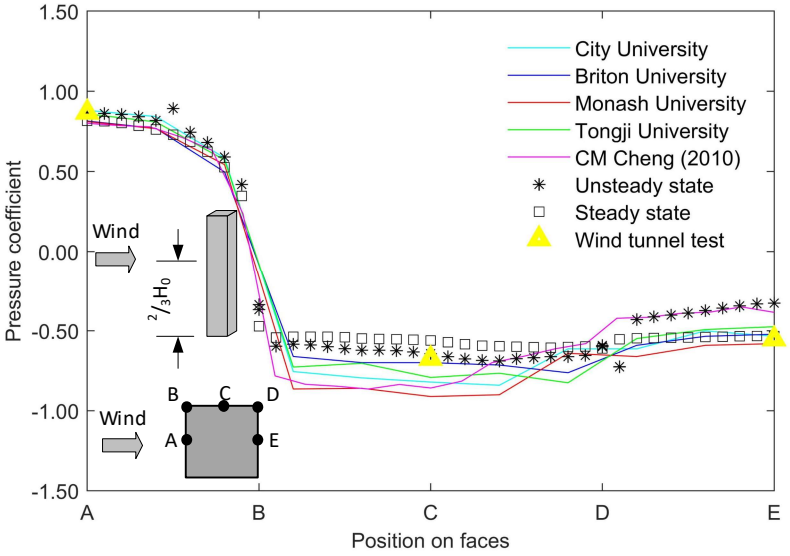

Figure 6-6: Comparison of mean pressure coefficient in the isolated test: Steady state and unsteady state

6.4 Turbulence model for LES

LES simulates the flow in wide range of time and length scales and ignores the smallest length scales by low-pass filtering of the Navier-Stokes equations. Smagorinsky is the classical model in simulation with different Smagorinsky constant Cs. AIJ recommends that Cs should be in value of 0.14 at the diffusion area. In this trial test, we would like to test the default number of Smagorinsky constant in OpenFOAM as Cs = 0.167 and the AIJ recommendation Cs = 0.14. Also, K-equation model which is governed by kinetic energy is also tested for validation.

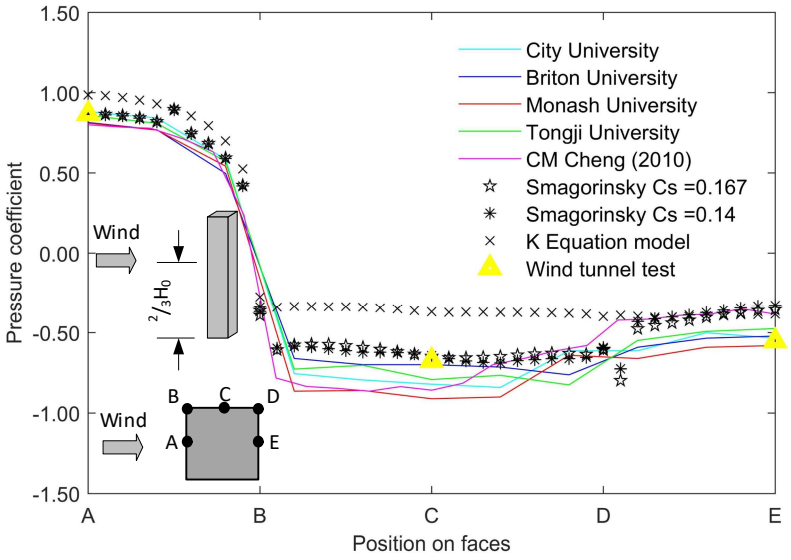

Figure 6-7: Comparison of mean pressure coefficient in the isolated test: Smagorinsky model and k equation model

Figure 6-7 shows the results of mean pressure coefficient on all faces. K-equation could not reproduce well the pressure on the side of model. While two cases of Smagorinky model show good agreement on pressure. There is not much different on two cases excepting at the edge between side and rear face. Thus, the Smagorinsky with Cs = 0.14 would be used in the simulation of interference tests in our study.

6.5 Pressure data

Figure 6-8, Figure 6-10, Figure 6-11 respectively represents the mean pressure coefficient of pressure taps along with the height of the front faces, side face and rear face of the principal model in tandem arrangements for simulation and wind tunnel tests. In general, simulation tests including LES and RANS represented well the trend of pressure on the front face. The isolated test has been validated by both methods of simulation when showing the closed results to the wind tunnel test. More turbulence was generated in the area between two buildings in interference tests leading to the fluctuation. LES model could represent more fluctuation in term of pressure the same as the wind tunnel test. RANS model shows the intense concentration of pressure on the front face. In addition, the slightly overestimated pressure data in LES simulation is also mentioned in (Tominaga, Mochida et al. 2016)

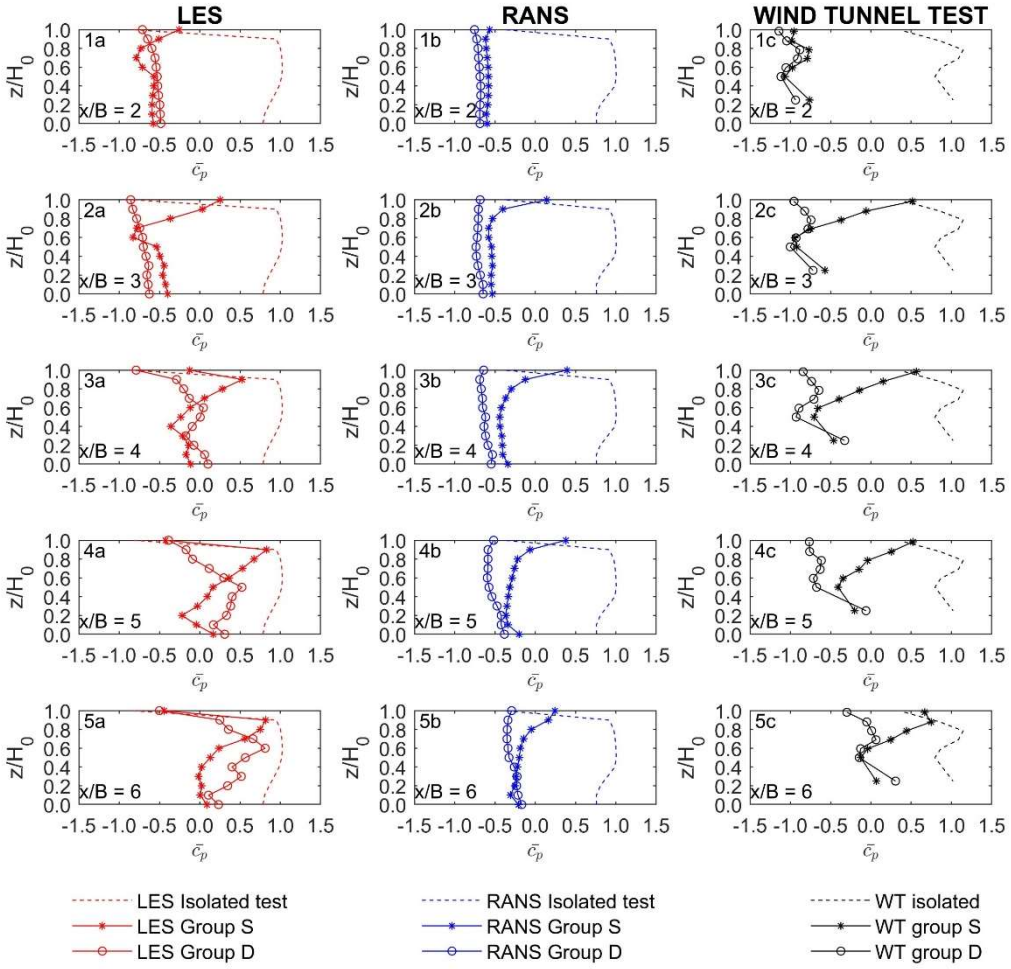

Figure 6-8: Comparison of RANS and LES to wind tunnel test results on the front face of the principal model (Graph 1a -5a: LES simulation; Graph 1b-5b: RANS simulation; Graph 1c-5c: Wind tunnel test)

At the side face (Figure 6-10), RANS model could indicate the trend better than LES simulation in term of the mean pressure. In all distance, the pressure coefficients on the side face of group D do not vary. An assumption has been made like the generation of Karman vortex on the side of the double height interference model (Figure 6-9b). This vortex affects clearly on the side face of the downstream building resulting in the negative pressure on the whole face. This phenomenon is not observed in group S at different distances of two models. The WOT has formed with the Karman vortex in case of group D to the arch-type vortex which is mentioned in Kawai, Okuda et al. (2012). Moreover, LES shows a wide fluctuation compared to RAN simulation. Regard to representation the average value on pressure. RANS has shown the advantage to predict the flow when showing the time-cost saving and the results.

All faces of the principal model get impacts from the arch-type vortex which is only generated from group S test. At the rear side (Figure 6-11), both RANS and LES provide precise information about the WOT flow. However, LES simulation gives overestimated different pressure between group S and group D. At rear face, the WOT flow helps to reduce pressure force in short distances which are x/B< 4B. In long distance, the arch-type vortex loses its

energy to contribute continuously to the pressure on the rear face. Pressure coefficients show no significant difference at the rear face between group S and group D. It is noted that the pressure along the rear face of the principal model in group S did not change as the distance x/B varies. Moreover, the pressure along the rear face did not varied corresponding to the tandem distance. An assumption of the steady vortex keeps staying at the rear face of the downstream building has been proposed as Figure 6-9a

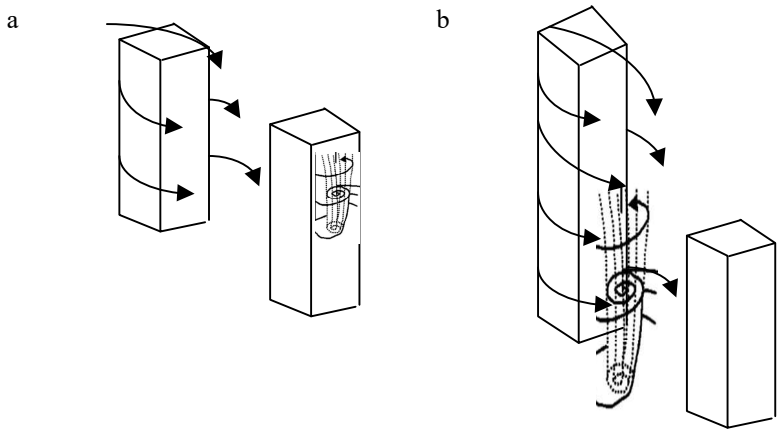

Figure 6-9: Vortex travelling assumption: a. Steady vortex behind downstream model; b. Karman vortex generated on the side of upstream model and move downward.

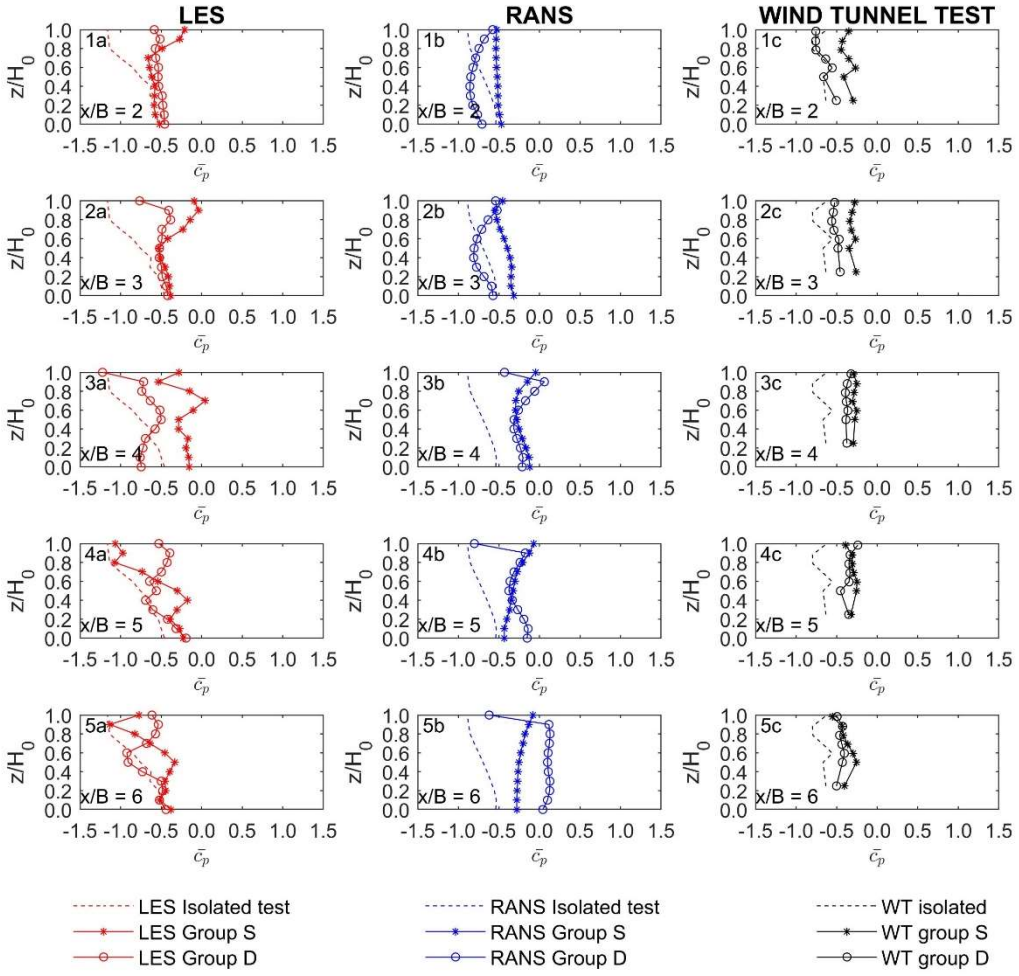

Figure 6-10: Comparison of RANS and LES to wind tunnel test results on the side face of the principal model (Graph 1a -5a: LES simulation; Graph 1b-5b: RANS simulation; Graph 1c-5c: Wind tunnel test)

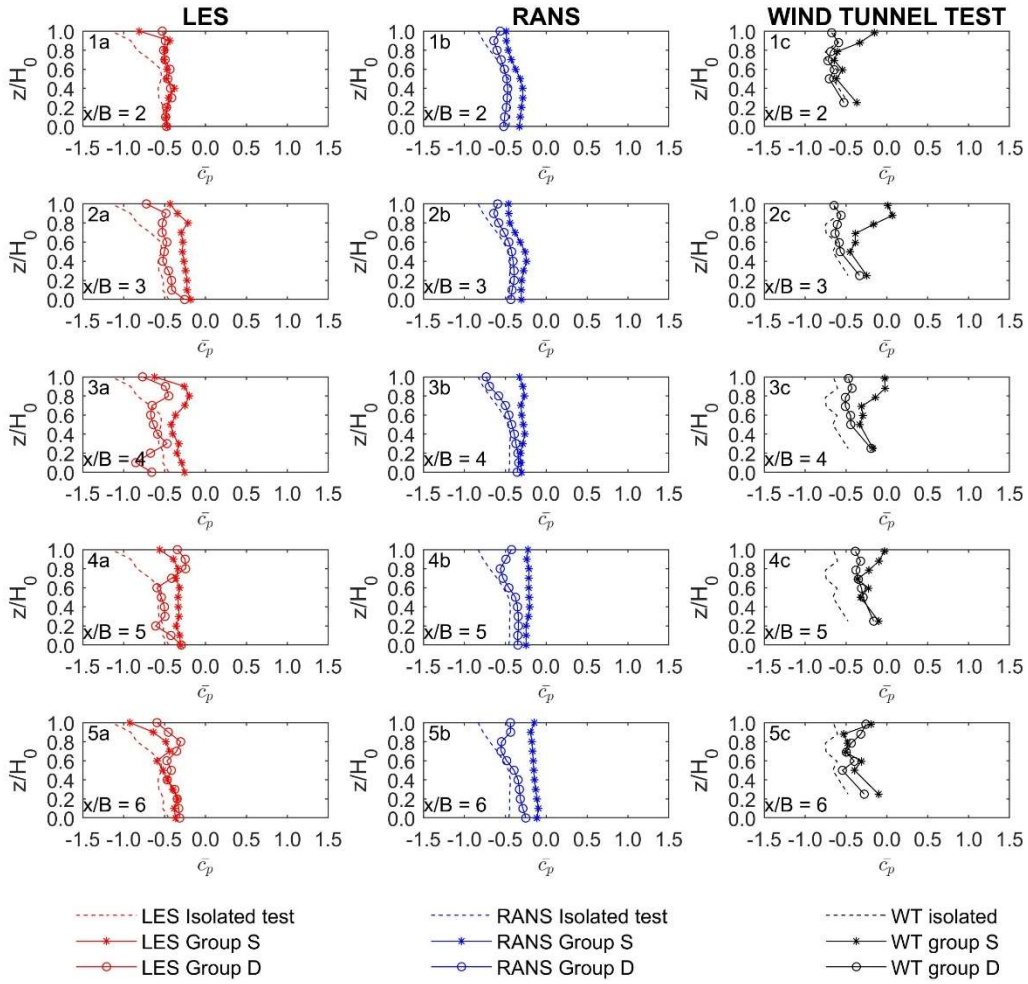

Figure 6-11: Comparison of RANS and LES to wind tunnel test results on the rear face of the principal model (Graph 1a -5a: LES simulation; Graph 1b-5b: RANS simulation; Graph 1c-5c: Wind tunnel test)

6.6 Velocity field in LES

Instantaneous images of flow in same height tandem arrangement x/B =5 one cycle are shown in Figure 6-12. A period is calculated from the frequency on the recorded pressure on the side face of the downstream building. Here the frequency is calculated as f = 3.687Hz (T = 0.271s). LES simulation could reproduce the WOT flow by including both shear layer and stationary vortex under the shear layer. This vortex always tips from the roof edge of upstream building and keep increasing the size till release energy and back to the initial size.

a)

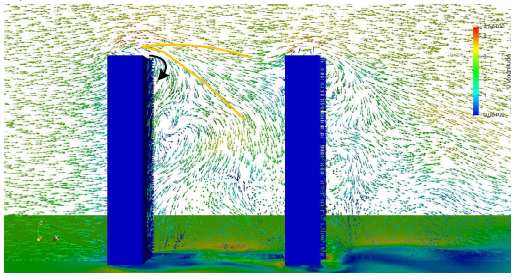

b)

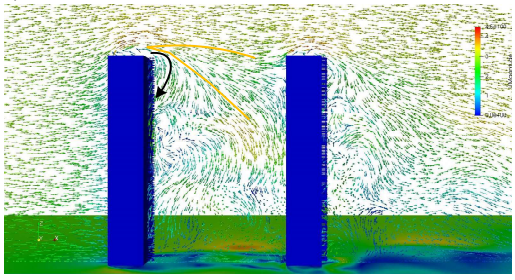

c)

d)

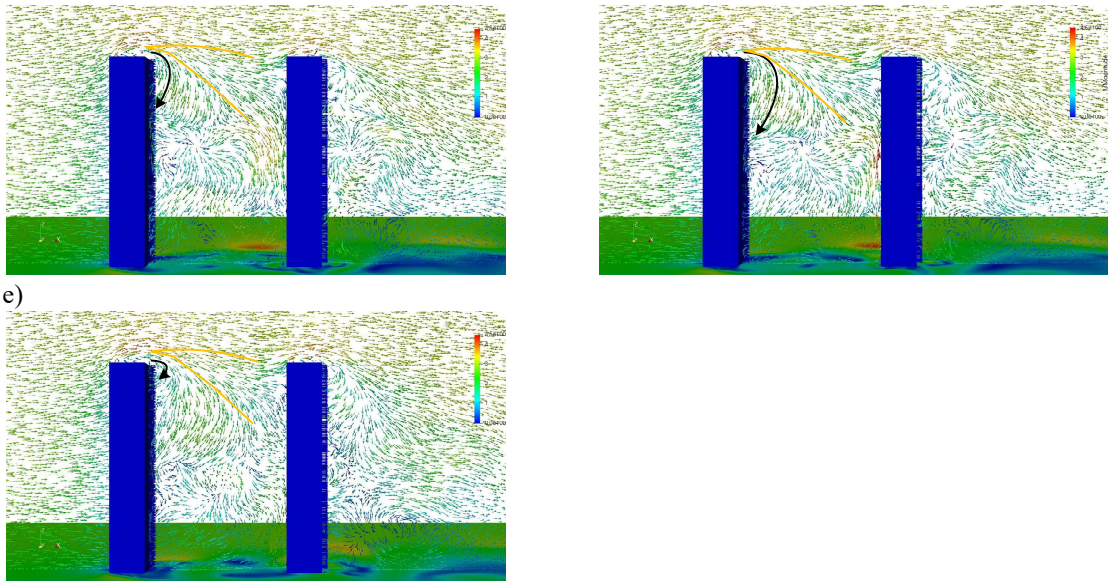

e)

Figure 6-12: Instantaneous images of velocity field in LES simulation , x/B = 5, y/B = 0: a) t = 0T; b) t = T/4; c) t = T/2; d) t = 3T/4; e) t = T;

Supplement: Suggestion on GPU simulation

With the development of Graphic Processing Unit recently, GPU is not only for display high quality of image but also is applied in the big data of simulation. RapidCFD was designed by simFlow and based on OpenFOAM 2.3.0 code. With different of concept in Central Processing Unit (CPU) and GPU, some of solver and algorithm is not correlation. GPU is still at the beginning of development process to build the code and environment to work with. The most difficult is a problem of code productivity. We know GPU is ideal for CFD tools, but it takes much time and human resources to implement all solvers to GPU, follow model updates, and make optimizations for GPU. Now we have learned a lot of tips for GPU optimization, and we can use easily and highly productive tools like OpenACC, however, GPU implementation of CFD tools like OpenFOAM is still a hard problem. GPU works with low frequency (around 1Ghz). To compensate on that, GPU is integrated with thousand of CUDA core. This point makes GPU work well with huge data parallelism.

During RapidCFD simulation, there is no overhead for GPU-CPU memory copy. all required data (initial data, boundary data, parameters, etc.) are transferred from CPU to GPU in an initial stage of RapidCFD. No redundant data transfers are required while main time loop is executed.

We test the speed of CPU and GPU on Deep learning box (24CPU Core i9-7920 & 4GPU Geforce GTX 1080 Ti 12Gb). More details can be found in Table S- 1. Noted that CPU is integrated with the latest development of CPU core working at high frequency.

Table S- 1: Simulation computer performance

Computer	Name	DeepLearningBOX
Hardware	CPU	Intel® Core™ i9-7920X [2.9 GHz, **12core 2socket**]
	GPU	GeForce GTX 1080 Ti 12Gb **x 4**
	SSD hard disk	SSD 960Gb
	HDD hard disk	HHD SATAIII 2Tb
	Memory	2666Mhz, **128Gb**
Software	OS	Ubuntu 16.04 LTS 64bit
	OpenFoam	Dev; 2.3; 4.1 ; 5 ; 6
	RapidCFD	RapidCFD-dev
	CUDA	8.0

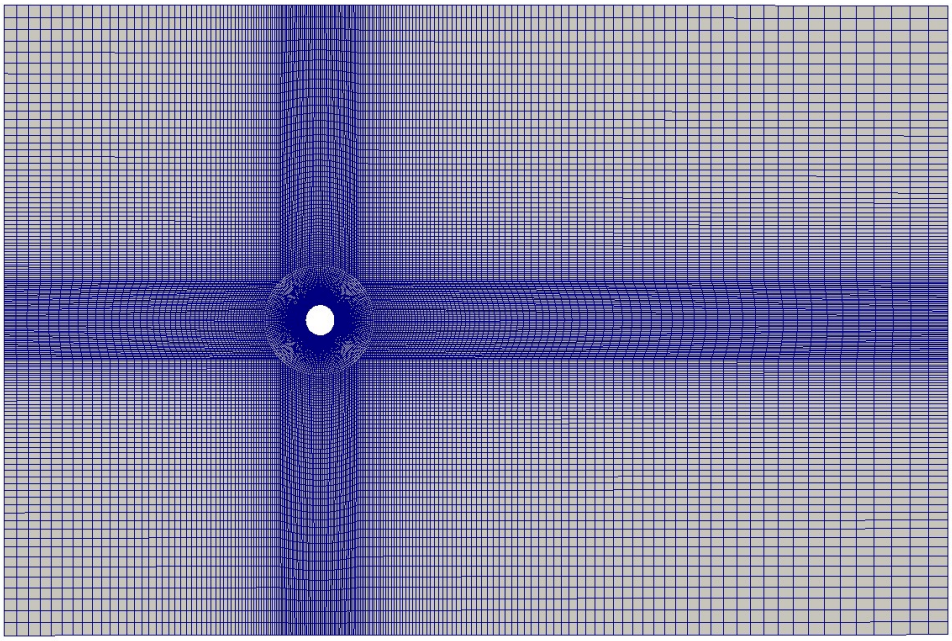

Figure S- 1: Mesh type of example test

The validation test with cylinder in laminar flow with structured mesh is tested with different mesh size. The mesh size is modified by changing the number of layers in thickness direction. The simulation keep the same schemes for every parts of Navier-Stock equation and using pisoFoam.

The results are shown in Figure S- 2. At low number of mesh sizes, the CPU work better compare to the GPU simulation. The explanation is that GPU accelerate the speed when the flow get convergence on simulation. When the mesh size increases to 700,000 cells. GPU and CPU work at the same speed. However, 1 GPU simulate faster compared to the simulation of 4GPU. The parallel running of GPU could not provide the best performance in this case. System need some time to divide work to each GPU in parallel simulation. The acceleration of 1GPU in case of 700,000 mesh cells is 1.2 times faster to 4CPU simulation.

At high computation effort with 3,000,000 cells, the GPU simulation show its advantages in parallel simulation. The simulation of 4GPU is faster 2.7 times compared to the simulation by 4CPU. However, the computer is integrated with 24 CPU. Then, higher computational mesh size was proposed at 15 million cells. At this moment, parallel GPU simulation still active with the acceleration about 2.5 faster.

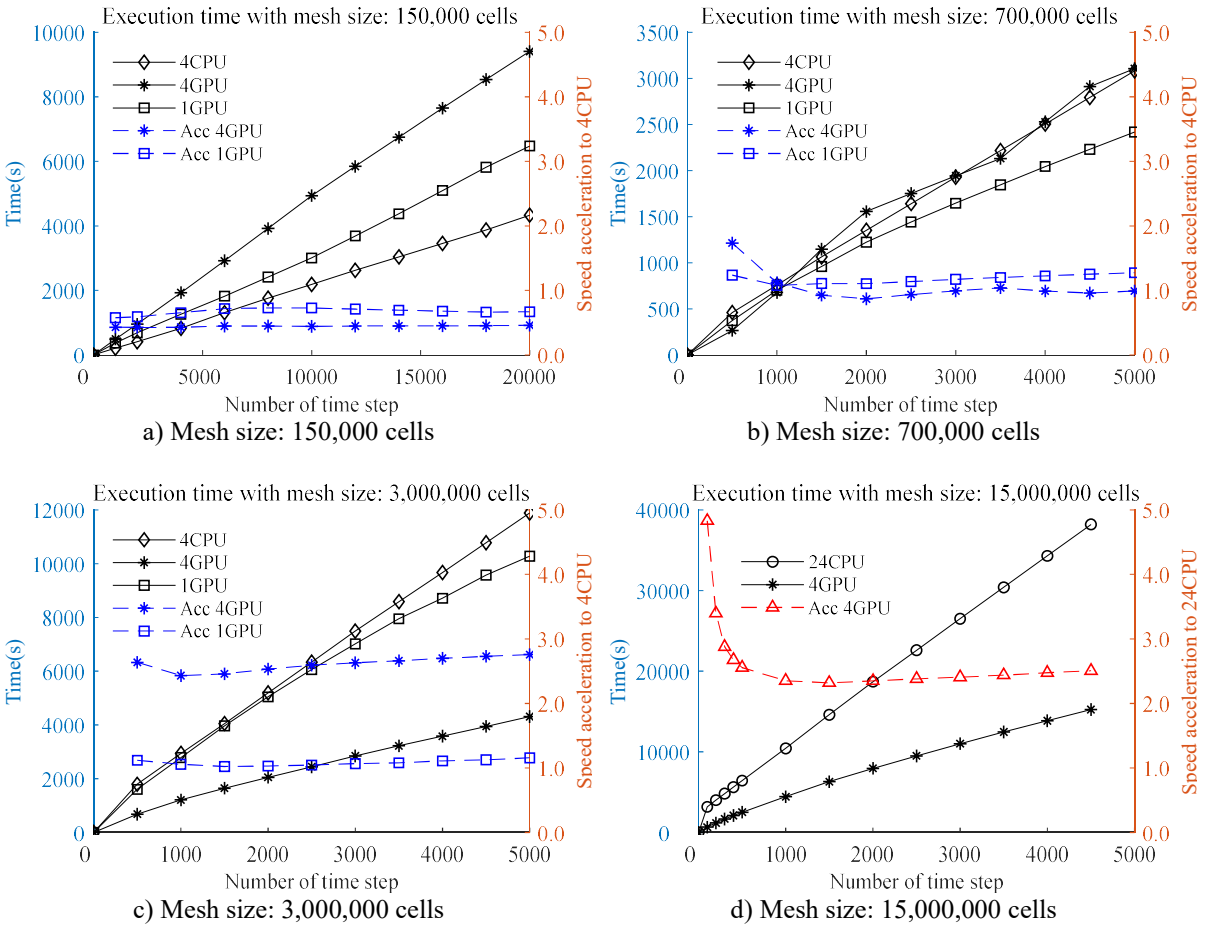

Figure S- 2: Comparison of execution time and GPU acceleration in different mesh sizes

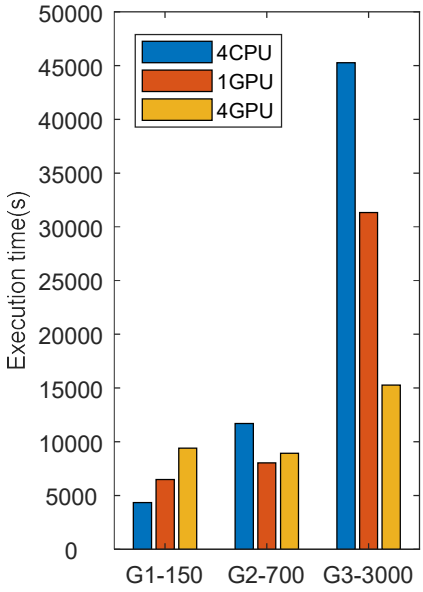

Figure S- 3: Comparison of execution time at same time step (20,000): G1-150: 150,000 cells; G2-700:700,00 cells; G3-3000:3,000,000 cells

Suggestion for using GPU

- With mesh size less than 700,000: Using CPU for simulation and have more options for solvers.

- 1 GPU work efficiently in range of 700,000 – 3 million cells.

- Multiple GPU is not suggested for small mess size (<3 million cells).

- At 15 million cells, speed ratio of 4GPU and 24 CPU is more than 2.5 times. Meanwhile, 1GPU=15CPU in term of simulation speed.

Chapter 7

Final remarks

7.1 Conclusion on the WOT flow

The WOT flow has strong effects in the same height models. At position x/B = 5, y/B =0 of the same height upstream model, the WOT flow could contribute 62.31% of pressure coefficient to the front face of the principal model.

The WOT flow produces significant effects on cladding pressure of the principal model for angles of attack from 0-20°.

In dynamic vibration, all distances of tandem arrangement show that the WOT flow provides the beneficial effects in terms of dynamic structural designs. Therefore, buildings on the site can resist better by the contribution of the WOT flow.

The WOT flow contain two parts: shear layer generated from the upstream model and the vortex under the shear layer. In a cycle, this vortex generates from the top with small size keep growing up to release the momentum.

URANS model could produce well for the mean of pressure on model but could not present correctly for the flow around the model. LES could reproduced well the results of instantaneous time in the other hand.

7.2 Research limitation

The research has been involved with the constant efforts. However, there are still few of limitational points that need to improve. Firstly, the simulation part could not simulate the vibration of building. With one dead end at the bottom of building, the simulation requires the displacement is vary from the bottom to the top. The current development of OpenFOAM does not allow us to simulate the displacement in three dimensions. Secondly, more pressured tap should be installed in all the faces of building model to research more detail in local pressures and peak pressures. More data on pressure, the research more perfectly present to the engineer group about the solution for cladding design of building in urban area.

7.3 Suggestion

7.3.1 Further research

The WOT flow could present in series of buildings like a row of 3 buildings. The research would figure out the behaviour of secondary WOT flow. In the range $3 \leq x/B \leq 6$, there is new type of vortex located behinds the downstream building. This kind of vortex is likely stationary. The exitance of this vortex may not affect to the design of building. However, it is not mentioned elsewhere in research area.

7.3.2 Building design in urban area

Strengthen the cladding near the top of building

Twin tower should be designed with the distance 3B to 6B to get the beneficial effect of the WOT flow

Design for a wide range of VIV for building

7.3.3 Simulation

Using polyhedral mesh to reduce the number of cell and execution time

Symmetry plane is not capable to use in symmetry domain

Using URANS to see the trend and the average of pressure

Using LES for the instantaneous flow velocity

Simulation by GPU is time-saving and cost-saving for large number of cell simulation

7.4 Publication

7.4.1 International Journal

- Long Doan Sy, Hitoshi Yamada and Hiroshi Katsuchi, "Interference effects of wind-over-top flow on high-rise buildings." Journal of Wind Engineering and Industrial Aerodynamics, 187, 85-96, April 2019.

7.4.2 International Conference

- Long Doan Sy, Hitoshi Yamada and Hiroshi Katsuchi (2019), Interference effects of two high-rise buildings on wind-over-top flow in tandem arrangement: Wind tunnel and CFD analysis. The 15th International Conference on Wind Engineering (ICWE15), Beijing, China.

- Long Doan Sy, Hitoshi Yamada and Hiroshi Katsuchi (2019), GPU acceleration in OpenFOAM simulation of Wind-over-top flow. The 3rd International Conference on Transportation Infrastructure and Sustainable development, Danang, Vietnam.

- Long Doan Sy, Hitoshi Yamada and Hiroshi Katsuchi (2019), Numerical simulation Wind-over-top flow over a square cylinder Cross comparison of unsteady RANS and LES. The 12th Pacific Structural Steel Conference, Tokyo, Japan.

Appendix: Calculation for elastic system

Building model details

Mass of model	M	2	kg	To	1	kg
centre of mass to pivot piont	Lm	0.3	m		0.3	m

Mass of stick under wind tunnel

Material: Steel	Density	7850	kg/m3		7850	kg/m3
Upper plate	Diameter	100	mm		100	mm
	Thickness	9	mm		9	mm
	Weight	0.55	kg		0.55	kg
	Center	0.00	m		0.00	m
Stick	Diameter	9	mm		9	mm
	Length	450	mm		450	mm
	Weight	0.22	kg		0.22	kg
	Center	0.10	m	To	0.23	m
Point for spring x 2	Diameter	10	mm		10	mm
	Inner dia.	9	mm		9	mm
	Length	20	mm		20	mm
	Weight	0.00	kg		0.00	kg
	Center	0.10	m		0.23	m
Damping card	Width	30	mm	To	60	mm
	Length	40	mm	To	80	mm
	Thickness	6	mm	To	6	mm
	Weight	0.06	kg	To	0.23	kg
	Center	0.47	m	To	0.49	m
Stiffener	Width	40	mm		40	mm
2 triangular	Length	40	mm		40	mm
	Thickness	6	mm		6	mm
	Weight	0.00	kg		0.00	kg
	Center	0.02	m		0.02	m
Total weight	m =	**0.84**	kg	To	**1.01**	kg
Distance to centre	Le =	**0.06**	m	To	**0.16**	m
					0.49	
Distance to damping	Ld =	**0.4745**	m	To	**45**	m

Spring stiffness

1 spring stiffness	k =	1	kg/cm		10	kg/cm
		981	N/m		**9810**	N/m
					0.23	
Distance from pivot	d =	**0.100**	m		**0**	m

Viscosity calculation

Liquid temperature		25	Celsius			
		298.15	Kelvin			
Reference	http://www.clearcoproducts.com/pdf/high-viscosity/NP-PSF-5,000cSt.pdf					
					0.12	
Distance from centre of bottom pendulum to bottom of oil tank					6	m

The area of plate in contact			From	0.0012	to	0.0048	m2
PSF 5000cSt	Kinetic viscosity υ	5000	Centistocks			0.005	m2/s
	Density	0.97	g/cm3			970	kg/m3
	Dynamic viscosity μ					4.85	Ns/m2
	Damping coefficient c		**0.046**	To		**0.19**	Ns/m
PSF 10000cSt	Kinetic viscosity υ	10000	Centistocks			0.01	m2/s
	Density	0.97	g/cm3			970	kg/m3
	Dynamic viscosity μ					9.70	Ns/m2
	Damping coefficient c		**0.093**	To		**0.37**	Ns/m
PSF 12500cSt	Kinetic viscosity υ	12500	Centistocks			0.01 25	m2/s
	Density	0.97	g/cm3			970	kg/m3
	Dynamic viscosity μ					12.13	Ns/m2
	Damping coefficient c		**0.116**			**0.46**	Ns/m
PSF 30000cSt	Kinetic viscosity υ	30000	Centistocks			0.03	m2/s
	Density	0.97	g/cm3			970	kg/m3
	Dynamic viscosity μ					29.10	Ns/m2
	Damping coefficient c		**0.278**	To		**1.11**	Ns/m
PSF 60000cSt	Kinetic viscosity υ	60000	Centistocks			0.06	m2/s
	Density	0.97	g/cm3			970	kg/m3
	Dynamic viscosity μ					58.20	Ns/m2
	Damping coefficient c		**0.556**	To		**2.23**	Ns/m
PSF 100000cSt	Kinetic viscosity υ	100000	Centistocks			0.1	m2/s
	Density	0.97	g/cm3			970	kg/m3
	Dynamic viscosity μ					97.00	Ns/m2
	Damping coefficient c		**0.927**	To		**3.71**	Ns/m

References

Aboshosha, H., A. Elshaer, G. T. Bitsuamlak and A. El Damatty (2015). "Consistent inflow turbulence generator for LES evaluation of wind-induced responses for tall buildings." Journal of Wind Engineering and Industrial Aerodynamics **142**: 198-216.

Amandolèse, X. and P. Hémon (2010). "Vortex-induced vibration of a square cylinder in wind tunnel." Comptes Rendus Mécanique **338**(1): 12-17.

Bailey, P. A. and K. C. S. Kwok (1985). "Interference excitation of twin tall buildings." Journal of Wind Engineering and Industrial Aerodynamics **21**(3): 323-338.

Balendra, T. and G. Nathan (1987). "Longitudinal, lateral and torsional oscillations of a square section tower model in an atmospheric boundary layer." Engineering Structures **9**(4): 218-224.

Banks, D. and R. N. Meroney (2001). "The applicability of quasi-steady theory to pressure statistics beneath roof-top vortices." Journal of Wind Engineering and Industrial Aerodynamics **89**(6): 569-598.

Banks, D. and R. N. Meroney (2001). "A model of roof-top surface pressures produced by conical vortices: Model development." Wind and Structures **4**(3): 227-246.

Banks, D., R. N. Meroney, P. P. Sarkar, Z. Zhao and F. Wu (2000). "Flow visualization of conical vortices on flat roofs with simultaneous surface pressure measurement." Journal of Wind Engineering and Industrial Aerodynamics **84**(1): 65-85.

Bearman, P. W. (1984). "Vortex shedding from oscillating bluff bodies." Annual review of fluid mechanics **16**(1): 195-222.

Bearman, P. W. and T. Morel (1983). "Effect of free stream turbulence on the flow around bluff bodies." Progress in Aerospace Sciences **20**(2): 97-123.

Bearman, P. W. and E. D. Obasaju (1982). "An experimental study of pressure fluctuations on fixed and oscillating square-section cylinders." Journal of Fluid Mechanics **119**: 297-321.

Blessmann, J. (1985). "Buffeting effects on neighbouring tall buildings." Journal of Wind Engineering and Industrial Aerodynamics **18**(1): 105-110.

Brika, D. and A. Laneville (1993). "Vortex-induced vibrations of a long flexible circular cylinder." Journal of Fluid Mechanics **250**: 481-508.

Cheng, C.-M., C.-L. Fu and Y. Chen (2010). Numerical simulation and validation of wind load and structural responses of an isolated tall building in turbulent boundary layer flow. The Fifth International Symposium on Computational Wind Engineering, USA May 23-27, 2010.

Cheng, C. and Y. Lin (2005). Interference effects on the design wind loads of tall buildings. Proceedings of the Sixth Asia-Pacific Conference on Wind Engineering, Seoul, Korea.

Corless, R. M. and G. Parkinson (1988). "A model of the combined effects of vortex-induced oscillation and galloping." Journal of Fluids and Structures **2**(3): 203-220.

Davidson, L. (2003). "Modification of the V2F model for computing the flow in a 3D wall jet." Turbulence Heat Mass Trans. **4**: 577-584.

Dragoiescu, C., J. Garber and S. Kumar (2006). A comparison of force balance and pressure integration techniques for predicting wind-induced response of tall buildings. Structural engineering and public safety proceedings of the structures congress.

English, E. (1993). Shielding factors for paired rectangular prisms: an analysis of along-wind mean response data from several sources. Proc, 7th US National Conf.

Gowda, B. H. L. and R. Kumar (2006). "Flow-induced oscillations of a square cylinder due to interference effects." Journal of Sound and Vibration **297**(3): 842-864.

Han, N., M. Gu and P. Huang (2012). Interference effect on wind pressure of two buildings. The Seventh International Colloquium on Bluff Body Aerodynamics and Applications (BBAA7). Shanghai, China.

Hellsten, A. (1998). Some improvements in Menter's k-omega SST turbulence model. 29th AIAA, Fluid Dynamics Conference.

Heschl, C., W. Sanz, I. Lindmeier and G. Clauss (2010). Validation of scale-adaptive and elliptic relaxation turbulence models applied to flow around buildings.
Huang, S. H., Q. S. Li and J. R. Wu (2010). "A general inflow turbulence generator for large eddy simulation." Journal of Wind Engineering and Industrial Aerodynamics **98**(10): 600-617.
Hui, Y., Y. Tamura and A. Yoshida (2012). "Mutual interference effects between two high-rise building models with different shapes on local peak pressure coefficients." Journal of Wind Engineering and Industrial Aerodynamics **104–106**: 98-108.
Isaev, S. and D. Lysenko (2009). "Calculation of unsteady flow past a cube on the wall of a narrow channel using URANS and the Spalart–Allmaras turbulence model." Journal of Engineering Physics and Thermophysics **82**(3): 488-495.
Kareem, A. (1987). "The effect of aerodynamic interference on the dynamic response of prismatic structures." Journal of Wind Engineering and Industrial Aerodynamics **25**(3): 365-372.
Kawai, H. (2002). "Local peak pressure and conical vortex on building." Journal of Wind Engineering and Industrial Aerodynamics **90**(4–5): 251-263.
Kawai, H. and G. Nishimura (1996). "Characteristics of fluctuating suction and conical vortices on a flat roof in oblique flow." Journal of Wind Engineering and Industrial Aerodynamics **60**: 211-225.
Kawai, H., Y. Okuda and M. Ohashi (2009). Three dimensional structures of flow behind a square prism. The Seventh Asia-Pacific Conference on Wind Engineering.
Kawai, H., Y. Okuda and M. Ohashi (2012). "Near wake structure behind a 3D square prism with the aspect ratio of 2.7 in a shallow boundary layer flow." Journal of Wind Engineering and Industrial Aerodynamics **104**: 196-202.
Kim, W., Y. Tamura and A. Yoshida (2009). Interference effects of two buildings on peak wind pressures. The Seventh Asia-Pacific Conference on Wind Engineering.
Kim, W., Y. Tamura and A. Yoshida (2013). "Simultaneous Measurement of Wind Pressures and Flow Patterns for Buildings with Interference Effect." Advances in Structural Engineering **16**(2): 287-305.
Kim, W., Y. Tamura and A. Yoshida (2015). "Interference effects on aerodynamic wind forces between two buildings." Journal of Wind Engineering and Industrial Aerodynamics **147**: 186-201.
Kim, Y. C. and S. W. Yoon (2014). Aeroelastic Vibration of Super-Tall Buildings. Advanced Materials Research, Trans Tech Publ.
Kumar, R. A. and B. H. L. Gowda (2006). "Flow-induced vibration of a square cylinder without and with interference." Journal of Fluids and Structures **22**(3): 345-369.
Kwok, K. and W. H. Melbourne (1981). "Wind-induced lock-in excitation of tall structures." Journal of the Structural Division **107**(1): 57-72.
Lam, K., S. Wong, J. Zhao, A. To and K. Tse (2013). Numerical simulation of interference effect on dynamic wind loading of tall buildings in close proximity by large-eddy simulation. Asia-Pacific Conference on Wind Engineering (APCWE), Research Publishing.
Lam, K. M., M. Y. H. Leung and J. G. Zhao (2008). "Interference effects on wind loading of a row of closely spaced tall buildings." Journal of Wind Engineering and Industrial Aerodynamics **96**(5): 562-583.
Lam, K. M., J. G. Zhao and M. Y. H. Leung (2011). "Wind-induced loading and dynamic responses of a row of tall buildings under strong interference." Journal of Wind Engineering and Industrial Aerodynamics **99**(5): 573-583.
Launder, B. E. and D. B. Spalding (1983). The numerical computation of turbulent flows. Numerical prediction of flow, heat transfer, turbulence and combustion, Elsevier**:** 96-116.
LI, X. and Q. S. LI (2015). Wind interference effects on super tall twin towers. The 14th International Conference on Wind Engineering ICWE14. Porto Alegre - Brazil.

Lien, F.-S. and G. Kalitzin (2001). "Computations of transonic flow with the v2–f turbulence model." International Journal of Heat and Fluid Flow **22**(1): 53-61.
Lien, F., W. Chen and M. Leschziner (1996). "Low-Reynolds-number eddy-viscosity modelling based on non-linear stress-strain/vorticity relations, Engineering Turbulence Modelling and Measurements-3 (W. Rodi and G Bergeles, Eds.)." Rodi, W., Bergeles, G.(eds.): 91-100.
Mannini, C., A. M. Marra, T. Massai and G. Bartoli (2017). Low-speed galloping for rectangular cylinders with side ratios larger than unity. title JAXA Special Publication: Proceedings of the First International Symposium on Flutter and its Application 宇宙航空研究開発機構特別資料.
Marwood, R. and C. J. Wood (1997). "Conical vortex movement and its effect on roof pressures." Journal of Wind Engineering and Industrial Aerodynamics **69-71**: 589-595.
Matsumoto, M., T. Yagi, H. Tamaki and T. Tsubota (2008). "Vortex-induced vibration and its effect on torsional flutter instability in the case of B/D= 4 rectangular cylinder." Journal of Wind Engineering and Industrial Aerodynamics **96**(6): 971-983.
Melbourne, W. (1975). Cross-wind response of structures to wind action. Proc. of the 4^< th> International Conference on Wind Effects on Buildings and Sructures.
Melbourne, W. H. (1980). "Comparison of measurements on the CAARC standard tall building model in simulated model wind flows." Journal of Wind Engineering and Industrial Aerodynamics **6**(1–2): 73-88.
MENG, Y. and K. HIBI (1998). "Turbulent measurments of the flow field around a high-rise building." Wind Engineers, JAWE **1998**(76): 55-64.
Menter, F. and T. Esch (2001). Elements of industrial heat transfer predictions. 16th Brazilian Congress of Mechanical Engineering (COBEM), sn.
Mochida, A., Y. Tominaga, S. Murakami, R. Yoshie, T. Ishihara and R. Ооκаш (2002). "Comparison of various ke models and DSM applied to flow around a high-rise building-report on AU cooperative project for CFD prediction of wind environment." Wind and Structures **5**(2-4): 227-244.
Nishimura, H. and Y. Taniike (2000). "Fluctuating pressures on a two-dimensional square prism." Journal of Structural and Construction Engineering(533): 37-43.
Norberg, C. (1993). "Flow around rectangular cylinders: pressure forces and wake frequencies." Journal of wind engineering and industrial aerodynamics **49**(1-3): 187-196.
Olivari, D. (1983). "An investigation of vortex shedding and galloping induced oscillation on prismatic bodies." Journal of Wind Engineering and Industrial Aerodynamics **11**(1-3): 307-319.
Ongoren, A. and D. Rockwell (1988). "Flow structure from an oscillating cylinder Part 1. Mechanisms of phase shift and recovery in the near wake." Journal of fluid Mechanics **191**: 197-223.
Parkinson, G. and P. Sullivan (1979). "Galloping response of towers." Journal of Wind Engineering and Industrial Aerodynamics **4**(3-4): 253-260.
Parkinson, G. and M. Wawzonek (1981). "Some considerations of combined effects of galloping and vortex resonance." Journal of Wind Engineering and Industrial Aerodynamics **8**(1-2): 135-143.
Peng, X.-q., C.-h. Zhang and C.-g. Qiao (2012). Numerical simulation of static interference effects for single building group. The Seventh International Colloquium on Bluff Body Aerodynamics and Applications (BBAA7). Shanghai, China.
Pindado, S., J. Meseguer and S. Franchini (2011). "Influence of an upstream building on the wind-induced mean suction on the flat roof of a low-rise building." Journal of Wind Engineering and Industrial Aerodynamics **99**(8): 889-893.
Ramponi, R. and B. Blocken (2012). "CFD simulation of cross-ventilation for a generic isolated building: Impact of computational parameters." Building and Environment **53**: 34-48.

Ramsey, S. R. (1990). "Wake resonance mechanisms in bluff body interactions." Journal of Wind Engineering and Industrial Aerodynamics **36**(Part 2): 1125-1133.
Sakamoto, H., H. Hainu and Y. Obata (1987). "Fluctuating forces acting on two square prisms in a tandem arrangement." Journal of Wind Engineering and Industrial Aerodynamics **26**(1): 85-103.
Shih, T.-H., W. W. Liou, A. Shabbir, Z. Yang and J. Zhu (1995). "A new k-ϵ eddy viscosity model for high reynolds number turbulent flows." Computers & Fluids **24**(3): 227-238.
Shih, T.-H., J. Zhu and J. L. Lumley (1993). "A realizable Reynolds stress algebraic equation model."
Simiu, E. and T. Miyata (2006). Design of Buildings and Bridges for Wind: A Practical Guide for ASCE-7 Standard Users and Designers of Special Structures, Wiley.
Spiegel, M., T. Redel, Y. J. Zhang, T. Struffert, J. Hornegger, R. G. Grossman, A. Doerfler and C. Karmonik (2011). "Tetrahedral vs. polyhedral mesh size evaluation on flow velocity and wall shear stress for cerebral hemodynamic simulation." Computer methods in biomechanics and biomedical engineering **14**(01): 9-22.
Stathopoulos, T. and C. C. Baniotopoulos (2007). Wind effects on buildings and design of wind-sensitive structures, Springer Science & Business Media.
Sy, L. D., H. Yamada and H. Katsuchi (2019). "Interference effects of wind-over-top flow on high-rise buildings." Journal of Wind Engineering and Industrial Aerodynamics **187**: 85-96.
Tamura, Y. and A. Kareem (2013). Advanced structural wind engineering, Springer Science & Business Media.
Taniike, Y. (1991). "Turbulence effect on mutual interference of tall buildings." Journal of engineering mechanics **117**(3): 443-456.
Taniike, Y. (1992). "Interference mechanism for enhanced wind forces on neighboring tall buildings." Journal of Wind Engineering and Industrial Aerodynamics **42**(1-3): 1073-1083.
Templin, J. T. and K. R. Cooper (1981). "Design and performance of a multi-degree-of-freedom aeroelastic building model." Journal of Wind Engineering and Industrial Aerodynamics **8**(1): 157-175.
Thanh, T. N., H. Yamada and H. Katsuchi (2005). Motion-dependent forces in high-rise building. 2005 Structures Congress and the 2005 Forensic Engineering Symposium-Metropolis and Beyond.
Tominaga, Y. (2015). "Flow around a high-rise building using steady and unsteady RANS CFD: Effect of large-scale fluctuations on the velocity statistics." Journal of Wind Engineering and Industrial Aerodynamics **142**: 93-103.
Tominaga, Y., A. Mochida, R. Yoshie, H. Kataoka, T. Nozu, M. Yoshikawa and T. Shirasawa (2016). AIJ Benchmarks for validation of CFD simulation.
Wilcox, D. C. (1998). Turbulence modeling for CFD, DCW industries La Canada, CA.
Williamson, C. and R. Govardhan (2004). "Vortex-induced vibrations." Annu. Rev. Fluid Mech. **36**: 413-455.
Williamson, C. H. K. and R. Govardhan (2008). "A brief review of recent results in vortex-induced vibrations." Journal of Wind Engineering and Industrial Aerodynamics **96**(6): 713-735.
Wu, F., P. P. Sarkar, K. C. Mehta and Z. Zhao (2001). "Influence of incident wind turbulence on pressure fluctuations near flat-roof corners." Journal of Wind Engineering and Industrial Aerodynamics **89**(5): 403-420.
Xie, Z. N. and M. Gu (2004). "Mean interference effects among tall buildings." Engineering Structures **26**(9): 1173-1183.
Yahyai, M., K. Kumar, P. Krishna and P. Pande (1992). "Aerodynamic interference in tall rectangular buildings." Journal of Wind Engineering and Industrial Aerodynamics **41**(1-3): 859-866.

Yakhot, V., S. Orszag, S. Thangam, T. Gatski and C. Speziale (1992). "Development of turbulence models for shear flows by a double expansion technique." Physics of Fluids A: Fluid Dynamics **4**(7): 1510-1520.
Yan, B. W. and Q. S. Li (2016). "Wind tunnel study of interference effects between twin super-tall buildings with aerodynamic modifications." Journal of Wind Engineering and Industrial Aerodynamics **156**: 129-145.
Yoshie, R., H. Kawai, M. Shimura and R. Wei (1997). "A study on wind-induced vibration of super high rise building by multi-degree-of freedom model." Journal of Wind Engineering and Industrial Aerodynamics **69**: 745-755.
Yu, X. F. and Z. N. Xie (2015). Interference effects on wind pressure distribution for high-rise buildings. The 14th International Conference on Wind Engineering ICWE14. Porto Alegre - Brazil.
Zdravkovich, M. (1985). "Flow induced oscillations of two interfering circular cylinders." Journal of Sound and Vibration **101**(4): 511-521.
Zhao, M. (2015). "Flow-induced vibrations of square and rectangular cylinders at low Reynolds number." Fluid Dynamics Research **47**(2): 025502.
Zhou, Y. and A. Kareem (2003). "Aeroelastic balance." Journal of engineering mechanics **129**(3): 283-292.